Design of Photocage Ligands for Light-Activated Changes in Coordination of d-block Transition Metals

by

Katie L. Ciesienski

Department of Chemistry
Duke University

Date:_____

Approved:

_____
Katherine J. Franz Ph.D, Supervisor

_____
Alvin L. Crumbliss, Ph.D.

_____
Michael C. Fitzgerald, Ph.D.

_____
Jiyong Hong, Ph.D.

Dissertation submitted in partial fulfillment of
the requirements for the degree of Doctor
of Philosophy in the Department of
Chemistry in the Graduate School
of Duke University

2010

ABSTRACT

Design of Photocage Ligands for Light-Activated Changes in Coordination of d-block Transition Metals

by

Katie L. Ciesienski

Department of Chemistry
Duke University

Date:_____

Approved:

_____
Katherine J. Franz, Ph.D., Supervisor

_____
Alvin L. Crumbliss, Ph.D.

_____
Michael C. Fitzgerald, Ph.D.

_____
Jiyong Hong, Ph.D.

An abstract of a dissertation submitted in partial fulfillment of the requirements for the degree of Doctor of Philosophy in the Department of Chemistry in the Graduate School of Duke University

2010

Abstract

The concept of light-activated "caged" metal ions was first introduced for Ca^{2+}. These high affinity coordination complexes are activated by UV light to release calcium ions intracellularly and have found widespread use in understanding the many roles of calcium in biological processes. There is an unmet need for photocaging ligands for biologically relevant transition metal ions. Described here are the first examples of uncaging biologically important d-block metal ions using photoactive ligands.

New nitrogen-donor ligands that contain a photoactive nitrophenyl group within the backbone have been prepared and evaluated for their metal binding affinity. Exposure of buffered aqueous solutions of apo-cage or metal-bound cage to UV light induces cleavage of the ligand backbone reducing the denticity of the ligands. Characterization of several caging compounds reveals that quantum efficiency and metal binding affinity can be tuned by modifications to the parent structure. The change in reactivity of caged vs. uncaged metal for promoting hydroxyl radical formation was demonstrated using the *in vitro* deoxyribose assay. The function of several of these compounds *in vivo* pre- and post-photolysis has been validated using MCF-7 cells. This strategy of caging transition metals ions is promising for applications where light can trigger the release of metal ions intracellularly to study metal trafficking and distribution, as well as, selectively impose oxidative stress and/or metal toxicity on malignant cells causing their demise.

Dedication

I dedicate my dissertation to my mom and dad for all their love and support.

Contents

List of Tables

List of Figures

List of Schemes

Acknowledgements

First and foremost, I would like to thank Dr. Katherine Franz, my Ph.D. advisor, I could not have asked for a better boss. Your support and encouragement has been invaluable to me.

I would like to thank my committee, Dr. Alvin Crumbliss, Dr. Michael Fitzgerald, and Dr. Jiyong Hong for your time and commitment. I am also thankful to Dr. Katherine Franz, Dr. Alvin Crumbliss, Dr. Michael Fitzgerald, and Dr. George Dubay for supporting me throughout my pursuit of a postdoctoral position.

To the past and present members of the Franz lab, I thank you for your friendship and making the laboratory such a great place to learn and work. A special thanks to Lynne Hyman, Kathryn Haas, and Marina Dickens for your scientific collaborations and for being such great friends. I could not have done it without you. To all of my friends in the department, I want to thank you for so many great memories.

Most importantly, I would like to thank my family for always believing in me. To my mom and dad, your confidence in me has allowed me to pursue my dreams. I thank you both and truly appreciate all you have done for me. Finally, I would like to thank my fiance, John Stanko, for all your love and support. This experience definitely would not have been the same without you.

1. Keys for Unlocking Photolabile Metal Cages[1]

The ability to control the spatial distribution and temporal release of specific bio-reactive molecules allows researchers to understand how various chemical events mediate biological processes. Caged or light-modulated molecules enable the use of light as a non-invasive trigger to turn on such events. The term "caged" was coined by Kaplan, Forbush, and Hoffman in 1978 to describe their light-activated ATP molecule.[1] Caged, in this sense, means that the biological activity of a molecule is blocked by the covalent attachment of a photolabile protecting group onto a key functional group of the molecule. The molecule is thereby rendered inactive (i.e. caged) until irradiation with UV light alters the photolabile component to reveal the functionality of the molecule and restore its biological activity. This strategy has been used to cage various biomolecules, including peptides, proteins, nucleic acids, effectors that regulate gene expression, secondary messengers, and nucleotide cofactors, just to name a few.[2-4]

Metal ions can also ellicit profound biological responses, and it would be desirable to control these responses by either releasing metal ions or altering their reactivity on-demand in a similar fashion to the light-induced uncaging of organic molecules. Caging metal ions, however, requires a different strategy from the covalent protecting group method used for organic molecules. In this chapter, we explore various methods to cage metal ions, including transition metal ions. We define two types of cages

---

[1] Reproduced in part with permission from Ciesienski, K. L. and Franz, K. J. *Angewandte Chemie-International Edition* **2010**, *Manuscript Submitted*. Copyright 2010 Wiley-VCH Verlag GmbH & Co. KGaA, Weinheim.

for metal ions: “locked” and “unlockable”. In this context, a locked metal cage refers to a conventional definition of a cage compound wherein a metal ion is completely encapsulated in a three-dimensional cavity provided by a macropolycyclic ligand.[5] In contrast, unlockable cages here refer specifically to photocages in which the coordination environment around the metal center changes upon light exposure.

Scheme 1: First "caged" molecule

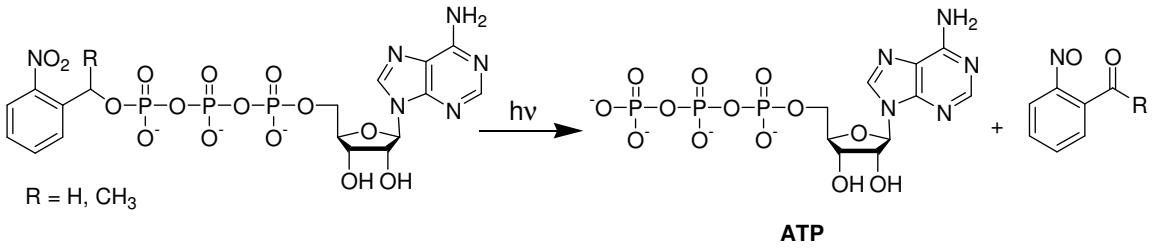

1.1 Locked Metal Cages

The utility of locked metal cages in biology and medicine relies on the metal ion remaining isolated from and unreactive with other species in its environment. Some examples are shown in Figure 1. In these cases, the three-dimensional scaffold of the ligand provides all of the donor atoms to coordinatively saturate the metal, and in doing so imposes further steric and electronic restraints beyond those of their two-dimensional counterparts. This cryptate effect provides impressive thermodynamic and kinetic

stability to caged metal complexes.[6-8] The synthesis of preassembled apo-ligands such as the cryptand shown in Figure 1a is often tedious and low yielding.[9] However, template synthesis of molecules like diamsar in Figure 1b and other clathrochelates provides efficient access to encapsulating ligands.[10]

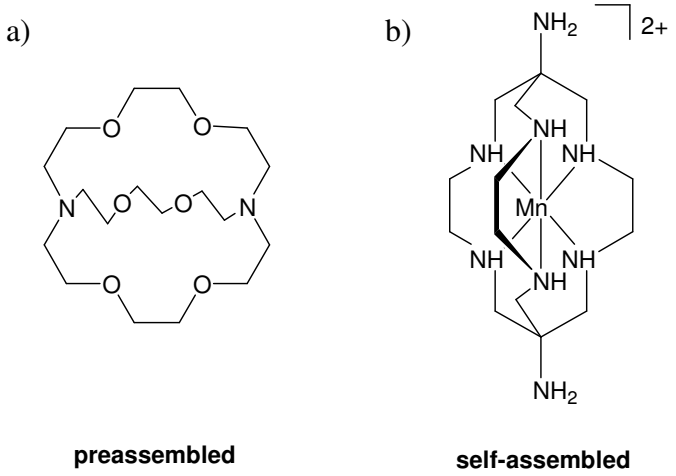

Figure 1: Examples of Locked Cages

For details on these compounds see references 9 and 10.

Due to the ease of synthesis and ability to vary the molecular scaffold of clathrochelates paired with their kinetic and thermodynamic stability, these complexes have both biochemical and medicinal applications. Some uses of these molecules include complexation of radioactive metal ions for radiotherapy and diagnostics, encapsulation of paramagnetic ions for magnetic resonance tomography, coordination of metals for HIV therapy, and membrane transporters for metal ions.[11] A comprehensive review of all of the applications of locked metal cages is beyond the scope of this dissertation, but further

information on this subject can be found in references 5 and 10.

1.2 Unlockable Metal Cages

The distinction between a locked metal cage and an unlockable metal cage is that the unlockable cage can be opened. Because we are specifically discussing photocages, light is the key that opens the cage, and the process of opening the cage entails a change in coordination environment of the metal ion. Whereas the utility of locked metal cages relies on the metal being unreactive with its environment, the utility of unlockable metal cages is that the reactivity of the complex with its surroundings changes selectively upon light exposure. The following sections describe two types of photocages that rely on light to alter the coordination chemistry of a metal complex. In the Type 1 case, light reacts with a photoactive component of the ligand to cause a change in reactivity of the metal center itself, whereas in the Type 2 case light causes a change in reactivity of a ligand that was once coordinated to the metal. This distinction is demonstrated by the cartoon in Figure 2, where light is used as the key to unlock the reactivity of either the metal ion or a component of the cage.

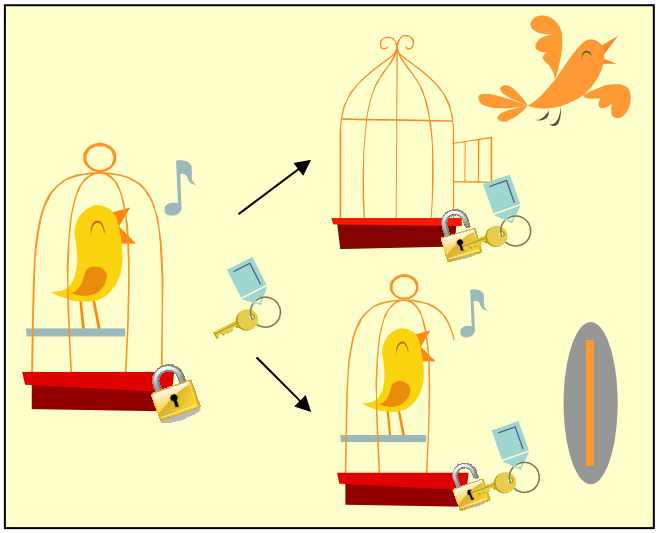

Figure 2: Cartoon of Unlockable Metal Cages

The bird in this cartoon represents a metal ion and the key represents light. Light can either unlock the metal ion or a component of the cage allowing it to interact with its environment.

1.2.1 Unlockable Metal Cages Type 1: Photoactive Ligand

A potential application for caged metal complexes is to use them as reagents to alter metal ion bioavailability. Incorporating a photoactivatable agent into a chelating ligand introduces a switch that can control the release of the coordinated metal in a spatial and temporal fashion. Such reagents could be valuable tools for studying cellular processes related to metal ion uptake, distribution, storage, usage, and trafficking.

1.2.1.1 Calcium Cages

Calcium cages are the most prominent example of the first definition of an unlockable metal cage. In this design, a photolabile and high affinity ligand chelates Ca^{2+} to render it biologically unavailable. Bioavailability is restored when UV irradiation leads to a photochemical change in the ligand backbone, liberating products with a diminished affinity for Ca^{2+}. In the late 1980s, the first calcium cages were developed independently by two groups.[12-14] These cages, shown in Scheme 2, became commercially available due to their applicability to biological systems. Both compounds utilize the same nitrobenzyl photochemistry, though the resulting photoproducts are quite different. When nitr-2 is photolyzed, methanol is released and a nitroso photoproduct forms. The presence of a benzylic carbonyl *para* to the conjugated nitrogen decreases the affinity for calcium from a K_d of 160 nM to ~8 μM.[14] On the other hand, when DM-nitrophen is exposed to UV light, the ligand backbone is cleaved, changing the binding affinity from a K_d of 5 nM to 3 mM after photolysis.[15] Due to this dramatic post-photolysis change in binding affinity, light can be used to control the time, location, and amplitude of calcium release.

Scheme 2: Photochemistry of nitr-2 and DM-nitrophen.

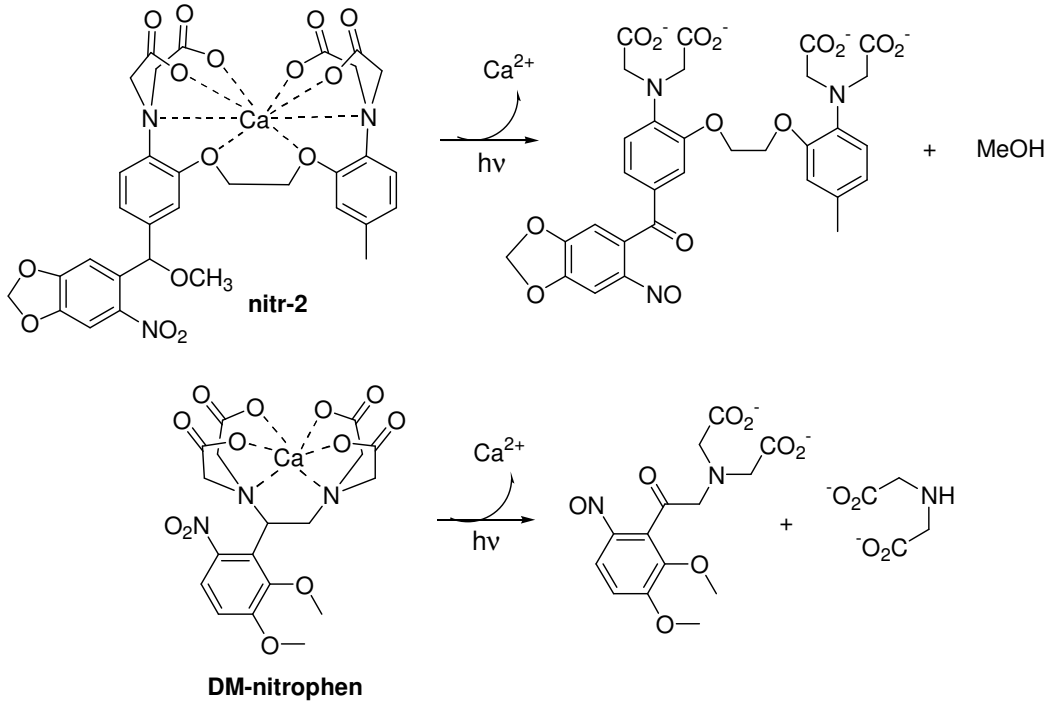

Most calcium cages utilize a 2-nitrophenyl group as the photolabile component of the molecule. These photoactive moieties were first used as protecting groups in organic synthesis and today remain most prevalent in photolabile cages. Their popularity stems in part from their compatibility with a wide variety of functional groups, including amides, amines, carboxylates, hydroxyls, and phosphates.[16,17] In addition, there are a number of derivatives that are commercially available or relatively easy to synthesize.

The nitrophenyl compounds photolyze with near-UV light centered at 350 nm, which lies in the UVA range (315–400 nm). Unlike UVB (280–315 nm) and UVC (100–280 nm), UVA is not absorbed by DNA and therefore does not directly cause DNA damage. Depending on the intensity of the light source, duration of exposure and cell type, however, UVA light can damage DNA and other cellular components indirectly via the formation of reactive oxygen species.[18,19] Light toxicity can therefore be a serious limitation of these compounds, and therefore it is essential that their photolysis be as efficient as possible. Figure 3 shows some of the later generation calcium cages designed to improve efficiency of photolysis.

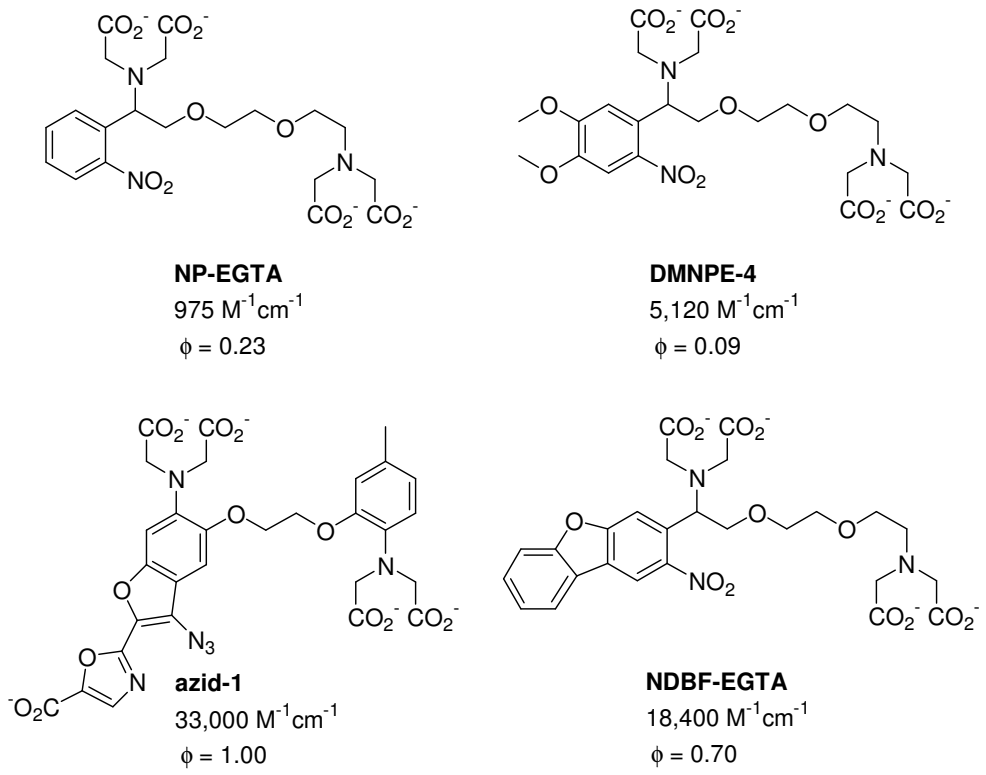

Figure 3: Photolabile Calcium Cages with Various Photolabile Groups

For details on these compounds see references 20-22.

Two defining qualities of a photolabile group are its quantum efficiency and extinction coefficient. If a photolabile compound can absorb light efficiently, then lower exposure times are needed and in turn cellular damage is reduced. One strategy used to improve quantum efficiency is to increase the extinction coefficient at 350 nm. This was accomplished in calcium cages by incorporating methoxy substituents at the four and five position of the ortho-nitrophenyl group. As shown in Figure 3, the addition of methoxy groups to NP-EGTA to form DMNPE-4, increases the extinction coefficient from 975 $M^{-1}cm^{-1}$ to 5,120 $M^{-1}cm^{-1}$.[20] Unfortunately, this increase in the extinction coefficient is not accompanied by an increase in quantum efficiency, as the value decreases from 0.23 for NP-EGTA to 0.09 for DMNPE-4.[20] Interestingly, DMNPE-4 was only the second calcium cage reported that is capable of undergoing efficient two-photon uncaging. The first such cage was azid-1 (Figure 3), a member of the nitr family and derivative of fura-2, a fluorescent calcium sensor. Due to its fluorescent properties, azid-1 has an extinction coefficient of 33,000 $M^{-1}cm^{-1}$ and photolyzes with an impressive quantum yield of unity to produce an amidoxime photoproduct.[21] Similarly, the incorporation of a nitrodibenzofurane chromophore into the ligand backbone of EGTA increases the extinction coefficient to 18,400 $M^{-1}cm^{-1}$, as seen in NDBF-EGTA, which is significantly higher than the extinction coefficient of NP-EGTA.[22] NDBF-EGTA also has a very high quantum yield of photolysis, 0.70, and is capable of two-photon uncaging.[22]

Calcium cages have been used successfully in many types of physiological experiments and have been useful for studying the roles of calcium in biological

processes.[15] This strategy has also been implemented to cage Sr^{2+}, Ba^{2+}, Mg^{2+}, Cd^{2+}, Mn^{2+} and Co^{2+}.[23-25] However, there are few examples of these compounds in the literature for biologically relevant d-block metals. The following sections will give an overview of the existing caged d-block metal compounds and their applications.

1.2.1.2 d-Block Metal Cages

When developing a caging ligand for transition metal ions, it is important to consider preferences of donor atoms, size of the chelate rings, and complex geometry. Binding affinity can be tuned by selecting donor atoms in accordance with the hard soft acid base (HSAB) principle and by optimizing the number and size of the chelate rings in relationship to the size of the cation. In addition, the binding geometry can aid in metal ion selectivity as transition metal ions vary in their number of valence d-electrons, and in turn, their preference for a certain binding geometry. Finally, careful consideration of the implications of the parameters discussed above on photolysis efficiency and on the desired reactivity pre- and post-photolysis is required.

1.2.1.3 Copper Cages

In an effort to expand the concept of caged metal complexes beyond calcium to biologically relevant transition metals, our group recently introduced a photosensitive caged copper complex, [$Cu(OH_2)$(cage)].[26] Our caging ligand, H_2cage, has a nitrophenyl group incorporated into a tetradentate ligand composed of two amide and two pyridyl

nitrogens. H_2cage binds Cu^{2+} with an apparent K_d of 16 pM at pH 7.4.[26] Irradiation with 350 nm UV light cleaves the ligand backbone within 4 min to release bidentate photoproducts with a diminished affinity for Cu^{2+} (Scheme 3). The high efficiency of photolysis of H_2cage, 0.73, is decreased to 0.32 upon Cu^{2+} coordination, indicating that copper impairs photolysis but does not prevent it.[26] In the absence of light, [Cu(OH_2)(cage)] was shown to inhibit hydroxyl radical formation in an *in vitro* assay. However, following light-induced uncaging, copper-catalyzed hydroxyl radical formation increased by 160%.[26] This photoactive caged copper complex is the first example of using light to alter the availability and reactivity of a biologically relevant transition metal. One drawback of H_2cage is that its 16 pM dissociation constant for Cu^{2+} is not strong enough to prevent competition with copper-binding proteins. To address this problem, we developed a series of 2nd generation chelators to better understand the effects of changes to the ligand backbone of H_2cage on Cu^{2+} binding affinity and photolysis efficiency. Using the results of this study, we developed a 3rd generation copper cage, called 3Gcage, that has an apparent K_d at pH 7.4 of 0.18 fM for Cu^{2+}, a remarkable improvement that should be strong enough to keep copper sequestered in the presence of endogenous copper binding proteins.[27] Like H_2cage, 3Gcage coordinates copper in a tetradentate binding site until activation with UV light cleaves the ligand backbone to release bidentate photoproducts with diminished affinity for Cu^{2+}, as shown in Scheme 3. In the dark, 3Gcage inhibits hydroxyl radical formation, while exposure to UV light increases hydroxyl radical formation by more than 300%. $[Cu(3Gcage)]^+$ may be a

useful tool for the delivery of metal ions to study metal trafficking pathways or to induce oxidative stress as a chemotherapy strategy, though $[Cu(3Gcage)]^+$ has not yet been validated in a cellular system.

Fluorescent sensors for Ca^{2+},[28] Zn^{2+},[29,30] and Cu^+ [31,32] have been widely used to investigate metal ion distribution. A common strategy is to design a probe such that coordination to a particular metal ion increases fluorescence intensity, known as a "turn-on" sensor. Developing this type of probe for Cu^{2+} is challenging, since it is paramagnetic and has a quenching effect on fluorescence. Therefore, many Cu^{2+} probes have a "turn-off" mechanism, which offers less accuracy and sensitivity. We developed a new type of turn-on sensor, coucage, in which a photoactive nitrophenyl group is incorporated into the backbone of a coumarin-tagged tetradentate ligand.[33] Coordination of Cu^{2+} dims the fluorescence output until irradiation with UV light cleaves the ligand backbone, which relieves the copper-induced quenching to provide a turn-on response, Scheme 3. Coucage displays a selective fluorescence response for Cu^{2+} over other biologically relevant metal ions. Experiments in live MCF-7 cells show that it can be used for detecting changes in intracellular Cu^{2+} upon the addition of a high concentration of exogenous copper, indicating that coucage could be a useful tool for visualizing the cellular distribution of labile copper to gain insight into the mechanisms of copper trafficking. However, since the probe is destroyed upon UV exposure, this strategy does not provide real-time monitoring of cellular Cu^{2+} fluctuations. It instead reports on the memory of where Cu^{2+} had been available for chelation. This method could be useful for

monitoring endogenous pockets of Cu^{2+} provided that adjustments can be made to the ligand to increase its copper binding affinity and to improve its quenching efficiency prior to light activation.

Scheme 3: Copper Cages

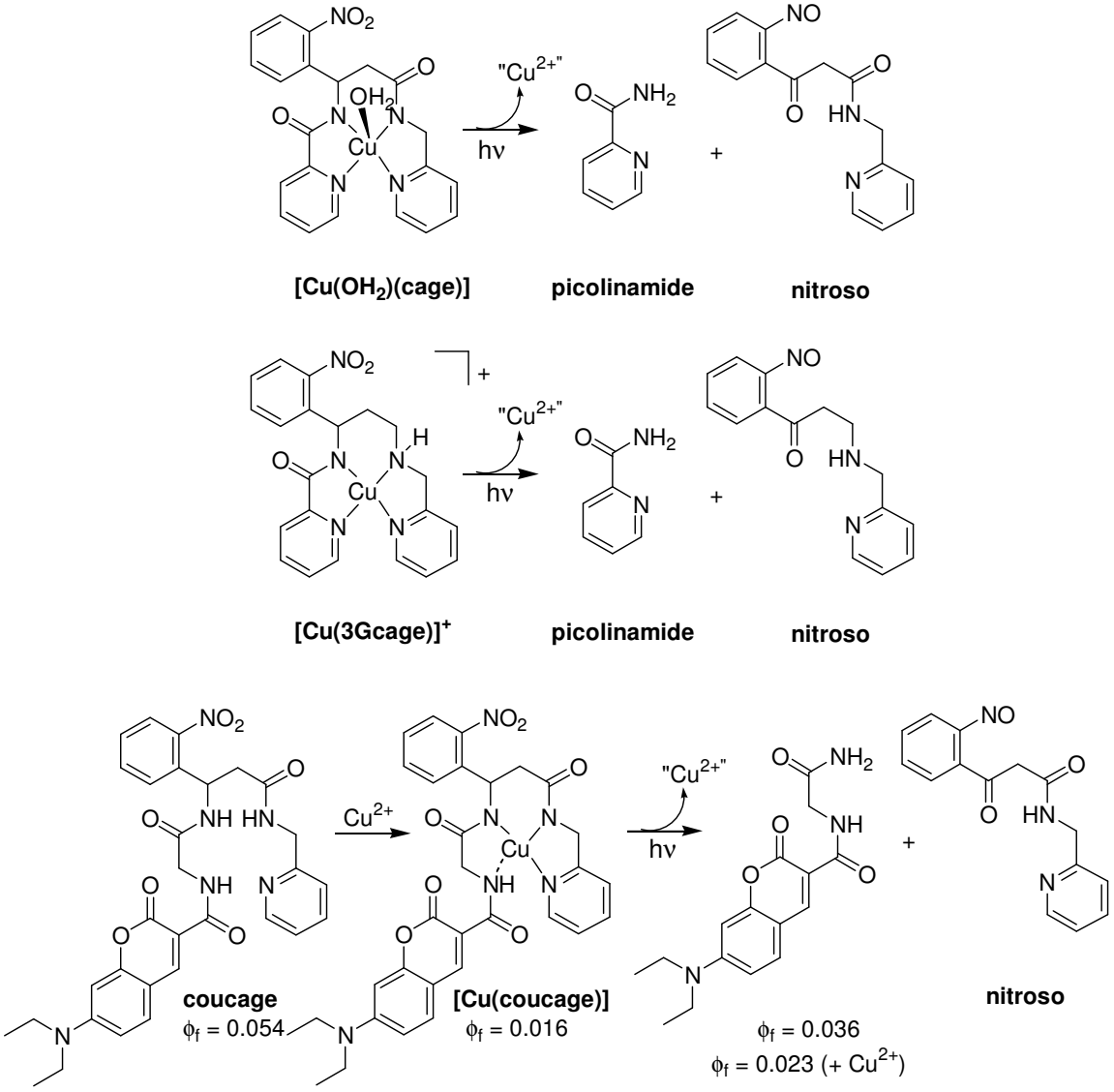

1.2.1.4 Zinc Cages

Burdette and coworkers have set out to develop caged zinc complexes to facilitate Zn^{2+} signaling research. For example, these tools can be used to address discrepancies about the relevance of synaptic zinc in neurotransmission. One current method for releasing Zn^{2+} into a biological system is to apply it exogenously in the form of a Zn^{2+} salt. This method has the potential to overwhelm the system with biologically irrelevant concentrations of zinc, that may induce a response not seen under more appropriate biological concentrations.

One of the first photoactive cages reported to chelate Zn^{2+} was CrownCast,[34] shown in Scheme 4. CrownCast has a crown ether receptor and photochemical properties similar to that of Tsien's nitr-2 calcium cage. Upon photolysis, a nitrosobenzophenone (UNC) is formed, which has decreased metal binding capabilities. This decrease in binding affinity is a result of the lone pair on the aniline nitrogen being donated into the benzophenone carbonyl oxygen. The apo-ligand is capable of binding Cd^{2+}, Ba^{2+}, Sr^{2+}, Ca^{2+}, Mg^{2+}, as well as Zn^{2+}. The highest binding affinity was observed for Ca^{2+} and lowest for Zn^{2+} with dissociation constants of 14 μM and 161 μM, respectively.[34]

The next generation chelator, ZinCast-1 (Scheme 4), binds Zn^{2+} in its tridentate binding pocket with a K_d of 14.3 μM.[35] Upon exposure to UV light, ZinCast-1 operates by the same photochemical mechanism as CrownCast. The formation of a ketone at the benzylic position causes a decrease in electron density on the aniline nitrogen producing a weaker Zn–N bond. After irradiation, the resulting photoproduct has a Zn^{2+} binding

affinity of 5.5 mM.[35] ZinCast-1 has also been shown to bind Cu^{2+} with a binding affinity of 4.5 μM pre-photolysis and 1.6 μM post-photolysis, indicating very little change in binding strength.[35]

ZinCleav-1, shown in Scheme 4, is different than the two previously discussed Zn^{2+} chelators in that its decreased binding affinity after photolysis is a result of cleavage of the ligand backbone. Of the three, ZinCleav-1 has the highest affinity for Zn^{2+} with a K_d of 0.23 pM.[36] After photolysis, it was estimated that the resulting photoproducts have Zn^{2+} binding affinities >150 μM for the 1:1 metal:ligand complexes and in the mM range for the 2:1 metal:ligand complexes.[36] In addition, ZinCleav-1 has the most efficient photolysis, with a quantum yield of 0.024[36] as compared to 0.007[35] for ZinCast-1, and 0.005[34] for CrownCast.

Chen and coworkers developed a different scaffold for their zinc cage, in which a phenolic Schiff base derivative is employed as the caging molecule. When this molecule is dissolved in organic solvent in the presence of stoichiometric amounts of base it was estimated to have a 2.93 x 10^3 M^{-1} (K_d = 0.34 mM) binding affinity for Zn^{2+}.[37] Upon irradiation with 365 nm UV light, a 2-arylbenzoxazole photoproduct is formed with a decreased affinity for Zn^{2+}, Scheme 4. This system is different than those previously discussed since a bidentate chelate cyclizes to abrogate metal binding upon irradiation. It was also demonstrated that this phenolic Schiff-base derivative binds other divalent metal ions, such as Fe^{2+} (1.34 x 10^3 M^{-1}), Ca^{2+} (6.28 x 10^2 M^{-1}), Cu^{2+} (2.73 x 10^3 M^{-1}), and Hg^{2+} (2.23 x 10^3 M^{-1}).[37] However, the reactivity of these metal ions *in vitro* and *in vivo* pre-

and post-photolysis has yet to be determined.

Scheme 4: Zinc Cages

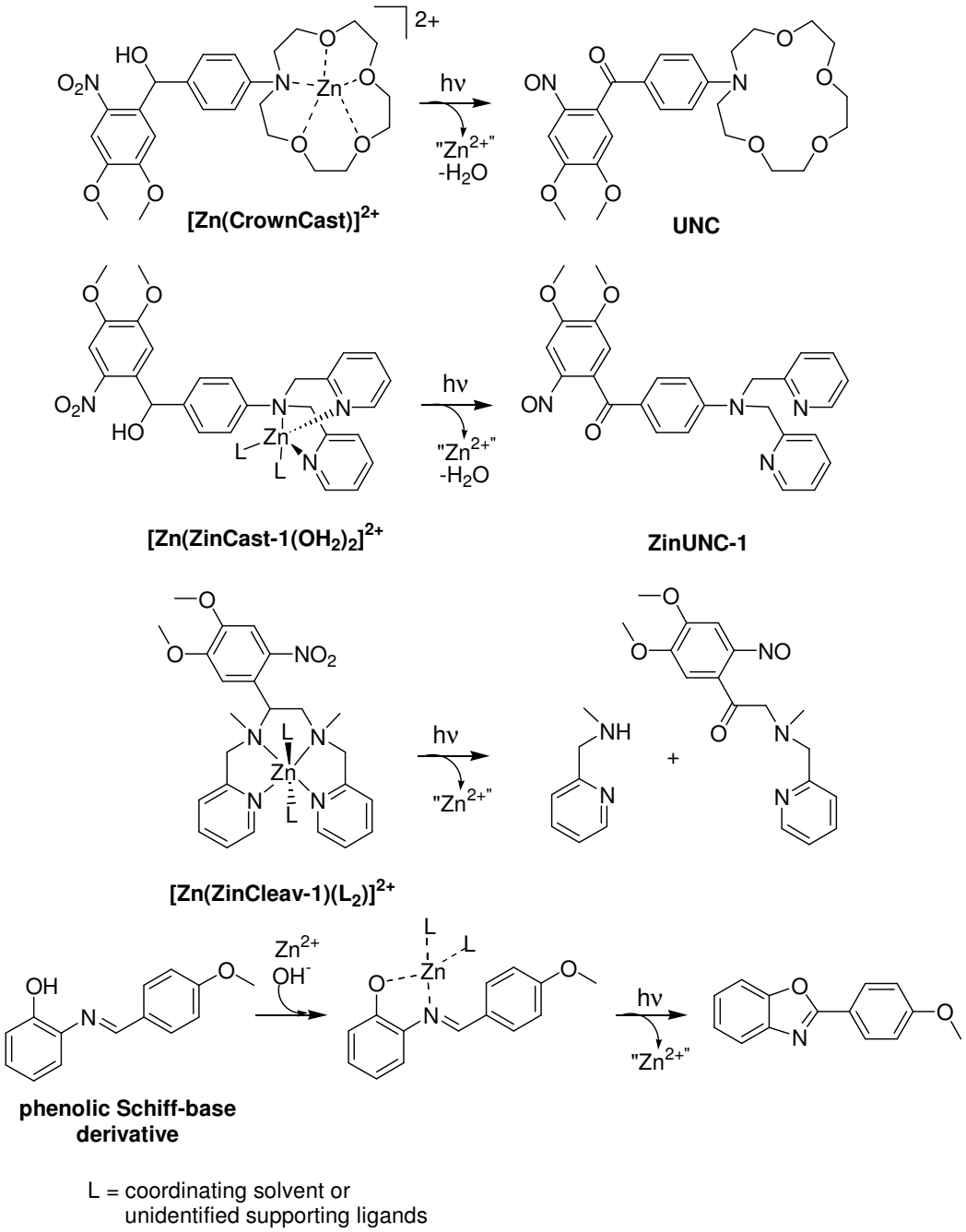

1.2.1.5 Iron Cages

Examples of naturally occurring unlockable cages include some classes of siderophores. Siderophores are high affinity Fe^{3+} chelators produced by bacteria to enable iron acquisition.[38-40] Butler and coworkers have investigated the photochemical properties of marine siderophores called aquachelins to gain insight into the biochemistry of iron in the upper-ocean.[41] Aquachelins contain various fatty acid tails attached to a peptidic headgroup that is responsible for coordination Fe^{3+} via two hydroxamate groups and one β-hydroxyaspartate to form a 1:1 Fe^{3+}:aquachelin complex.[42] In the presence of UVA light, Fe^{3+} is reduced to Fe^{2+} and the siderophore backbone is cleaved at the β-hydroxyaspartate residue, as shown in Scheme 5.[41] As a result, the conditional binding affinity for Fe^{3+} decreases from $10^{12.2}$ M^{-1} (K_d = 0.63 pM) pre-photolysis to $10^{11.5}$ M^{-1} (K_d = 3.16 pM) post-photolysis.[41] These findings show that siderophores not only mediate bacterial iron transport but their photolytic properties may affect the bioavailability of iron.

A second class of photoreactive siderophores structurally similar to aquachelins is aerobactin. A major difference between the two is that aerobactin contains an α-hydroxyacid in the form of citric acid.[43-45] It is proposed that Fe^{3+} is coordinated through two hydroxamate groups and a 3-ketoglutarate.[46,47] Irradiation with UV light into the ligand-to-metal charge transfer band (LMCT) results in the reduction of Fe^{3+} and the release of CO_2, Scheme 5. Unlike aquachelin, photolyzed aerobactin retains a similar affinity for Fe^{3+} as its unphotolyzed counterpart and promotes iron acquisition.[46] Since

photolysis does not result in a change in binding affinity, the repercussions of photolysis on biological function remain to be resolved.

Scheme 5: Photolabile Fe(III)-Siderophore Complexes

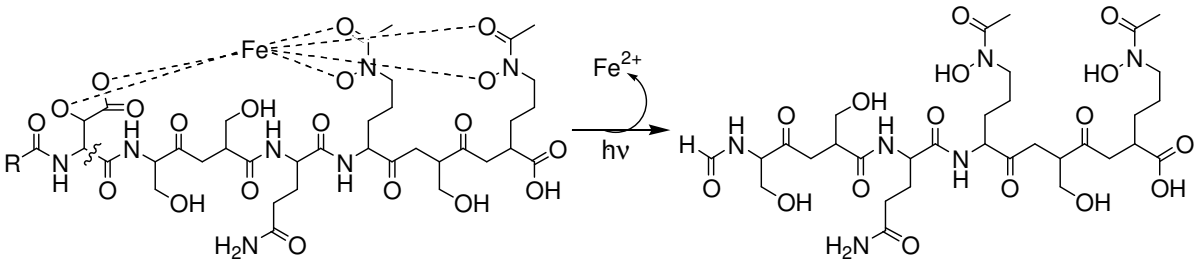

Fe(III)-aquachelin

R = Fatty acid tails

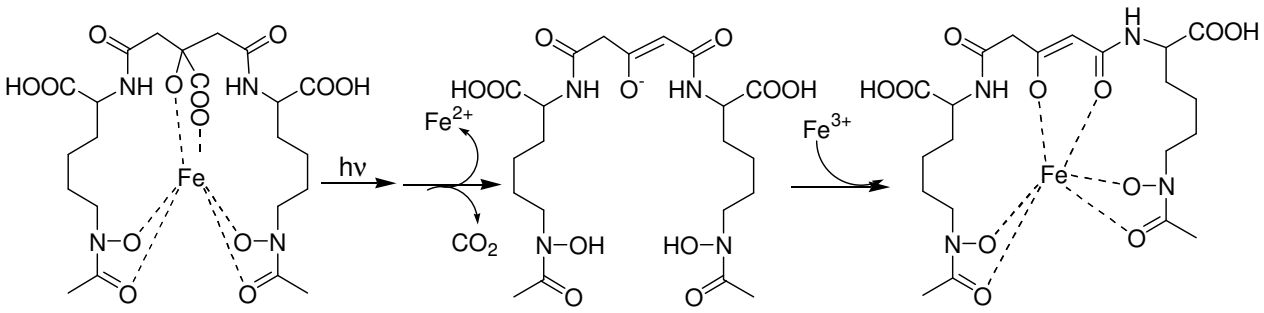

Fe(III)-aerobactin

Caged iron complexes could be useful to gain insight into iron homeostasis and iron's role in disease pathology. Burdette and coworkers developed Ferricast,[48] a photosensitive macrocyclic compound that binds Fe^{3+} in organic solvents. In a manner similar to their first generation zinc cages, Ferricast converts into the weaker binding FerriUNC upon UV irradiation, as shown in Scheme 6. The quantum yield of photolysis for this conversion is 0.01 for the apo-ligand and 0.04 for the metal complex.[48] Both the 1:1 and 2:1 FerriCast:Fe^{3+} complexes are present in organic solution.[48] Unfortunately, metalated FerriCast decomposes in aqueous solution, limiting its utility under biologically relevant conditions.

Scheme 6: Iron cage

FerriCast forms both the 1:1 and 2:1 ligand:metal complex.

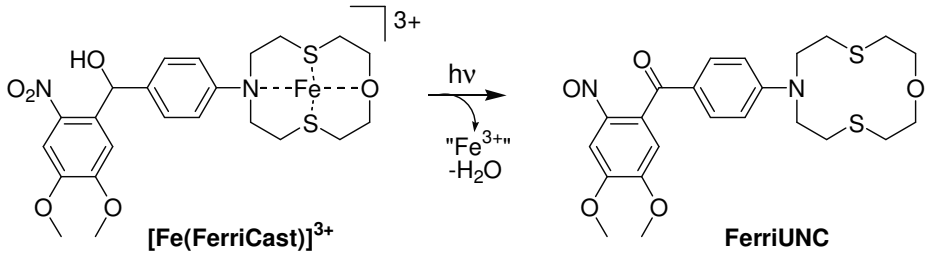

1.2.1.6 Platinum Cages

Cisplatin's anticancer activity has been well established since its fortuitous discovery in the 1960s.[49] Because of the overall success of cisplatin, thousands of analogs have been synthesized. The clinical effectiveness of many of these agents, unfortunately, is restricted since they are toxic to both healthy and cancerous tissue. Drawbacks include dose-limitations caused by severe side effects as well as intrinsic and acquired resistance to the drug. Therefore, a different approach to platinum drug design is needed. This section will outline photoactive drugs that can deliver Pt intracellularly in a site and time specific manner, which could potentially alleviate the limitations of the current drugs.

Photoactive drugs have been employed in photodynamic therapy (PDT), which uses a photosensitizing drug and light of a specific wavelength to generate singlet oxygen. The benefit of this method is that cytotoxic species are localized at the site of a tumor and healthy tissue is unaffected. PDT has been successful in the treatment of numerous cancers. The drawback of this method is that oxygen is required to carry out the cytotoxic mechanism, and yet many tumors are hypoxic.[50] An advantage of the potentially phototherapeutic agents discussed in this section is that they do not require oxygen for cytotoxicity.

The first photoactivatable platinum drug-like molecule was the Pt^{IV} complex $[PtCl_2I_2(en)]$, shown in Figure 4, introduced by Bednarski and coworkers.[51] Pt^{IV} complexes are more inert to ligand substitution than their Pt^{II} counterparts, and therefore

must be reduced to their active Pt^{II} form by extracellular and/or intracellular agents prior to reaction with DNA.[52,53] If the rate of reduction of Pt^{IV} to Pt^{II} can be increased at or around a tumor relative to normal tissue, then the effectiveness of the drug could be maximized. The $[PtCl_2I_2(en)]$ complex photoreduces with visible light. While the photoproducts were not characterized, the resulting complex was shown to bind DNA. However, the unphotolyzed complex was also able to bind DNA and there was no difference in cytotoxicity observed for cells kept in the dark as compared to those exposed to light. The lack of stability of this first-generation complex was attributed to its very positive reduction potential, 75 E/mV.[51]

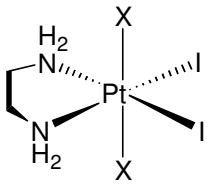

***trans,cis*-$[PtX_2I_2(en)]$**

X = Cl^- or OAc^-

Figure 4: First Photolabile Platinum Based Drugs

Next generation complexes were designed to increase the stability in the dark, one of which, *trans*,*cis*-[$Pt(OAc)_2I_2(en)$] (where X = OAc^-, in Figure 4), has a reduction potential of -65 E/mV.[54] Unfortunately, the cytotoxicity difference between cells kept in the dark and those exposed to light was less significant than expected. It was determined that Pt^{IV}-diiodo complexes are easily reduced *in vivo* by biological thiols to their toxic Pt^{II} counterparts, making them inadequate as a photolabile drug. These compounds may not have operated as desired, but importantly, they revealed the possibility of releasing a toxic platinum complex with light. By irradiating into the ligand-to-metal charge transfer (LMCT) band of the complex, a reductive elimination reaction is initiated.[55,56] The iodide leaving group is oxidized to a radical whereby Pt^{III} is formed. This platinum species will either recombine with the iodide radical or initiate the oxidation of another iodide forming a Pt^{II} complex. This class of compounds is different than the photocages previously discussed since the metal is the photosensitive component of the cage, as opposed to a photolabile component of the ligand. In this respect, they could be classified as Type 2 photocages.

In order to build Pt^{IV} complexes that are more stable in the presence of cellular reductants, Sadler and coworkers replaced the iodide groups with azides, since platinum azide complexes are known to undergo photoreductive elimination.[56] Upon irradiation with UVA light centered at 365 nm, the Pt^{IV} complexes shown in Figure 5 undergo photoreduction to Pt^{II} species. The mechanism of photoreduction is similar to that described above, except the azide radicals rapidly decompose into molecular nitrogen,

preventing the reoxidation of the platinum center.[55]

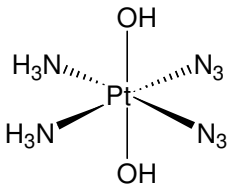

***cis,trans,cis*-[Pt(N$_3$)$_2$(OH)$_2$(NH$_3$)$_2$]**

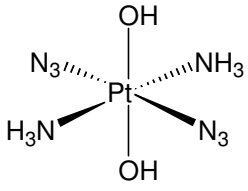

***trans,trans*,trans-[Pt(N$_3$)$_2$(OH)$_2$(NH$_3$)$_2$]**

Figure 5: *Cis* and *Trans* Isomers of Diazide-Pt^{IV} Complexes

Cis,trans,cis-[Pt(N$_3$)$_2$(OH)$_2$(NH$_3$)$_2$][57], shown in Figure 5, is soluble in aqueous solution, stable in the presence of glutathione, and photolyzes into a complex that binds DNA and 5'-GMP. In addition, the photolyzed complex inhibits the growth of human bladder cancer cells as well as cisplatin-resistant cells, while cells treated with the complex and kept in the dark showed very little growth inhibition.[58] Changing the NH_3 ligands does not significantly affect the stability of these complexes; therefore, derivatives with various amines have been synthesized and characterized.[59]

The distinct anticancer mechanism of *trans*-Pt^{II} compared to *cis*-Pt^{II} complexes has been known for some time,[60-62] and the *cis* vs *trans* photoactive Pt^{IV} complexes also appear to show distinct anticancer properties from the *cis* isomers. The all *trans* isomer, *trans,trans,trans*-[Pt(N$_3$)$_2$(OH)$_2$(NH$_3$)$_2$][63] (Figure 5) has enhanced water solubility

compared to the all *cis* version. In addition, its LMCT band is shifted to longer wavelengths with a larger extinction coefficient. In the dark it is stable in the presence of glutathione and is not cytotoxic to human cancer cells. It binds 5'-GMP after exposure to light and is as cytotoxic as cisplatin, albeit via a different mechanism of toxicity. Derivatives of this complex have been studied in depth.[59] Importantly, a derivative where NH_3 is replaced by a pyridine ligand is 90 times more cytotoxic than cisplatin.[64]

As an alternative to photoactive Pt^{IV} compounds, our group recently introduced a Pt^{II} photocaged complex, [Pt(cage)], in which Pt^{II} is coordinated to the photoactive ligand, H_2cage, through two amide and two pyridyl nitrogens.[65] The intact complex is unreactive toward ligand exchange reactions until activation with UV light (350 nm) uncages a Pt complex that more readily exchanges its ligands, as demonstrated in Scheme 7. When MCF-7 human breast carcinoma cells were treated with up to 200 μM [Pt(cage)] in the absence of light, $\leq$ 20% cell death occurred after 96 hours of treatment. However, cytotoxicity increased by 65% with 2 minutes of irradiation and approached the toxicity response of cisplatin.

Scheme 7: Photolysis of [Pt(cage)]

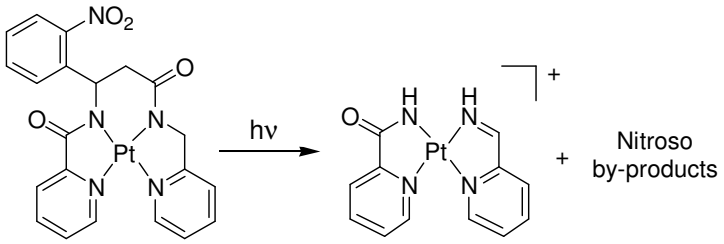

[Pt(cage)]

1.2.1.7 Ruthenium and Rhodium Cages

Ru^{II} complexes such as *cis*-$[Ru(bpy)_2(H_2O)_2]^{2+}$ and *cis*-$[Ru(phen)_2Cl_2]$, are known to be cytotoxic due to DNA binding,[66-69] although, like cisplatin, cytotoxicity is not localized to cancer cells. Therefore, Turro and coworkers developed a photolabile octahedral Ru^{II} complex, *cis*-$[Ru(bpy)_2(NH_3)_2]^{2+}$,[70] shown in Figure 6. Like the Pt^{IV} compounds discussed above, the metal is acting as the photosensitive component of the cage. Irradiation of the complex in water results in the loss of the NH_3 ligands and the formation of *cis*-$[Ru(bpy)_2(OH_2)(OH)]^+$. The photolyzed complex binds to 9-methyl- and 1-ethyl-guanine as well as single-stranded and double-stranded DNA. In contrast, no DNA binding was observed in the absence of light.

Similarly, Morris and coworkers developed octahedral Rh^{III} complexes,[71] such as DDP_2PHEN shown in Figure 6. These complexes are thermodynamically stable in the dark but are susceptible to hydrolysis when exposed to UV light to form species that

readily bind DNA. *In vivo*, DPP_2PHEN was shown to be cytotoxic to cancer cells and to inactivate an intracellular alphavirus Sindbis (SINV) following irradiation.[72]

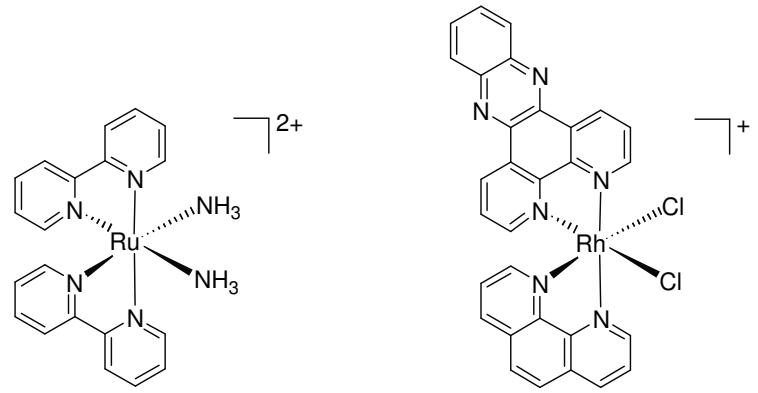

***cis*-$[Ru(bpy)_2(NH_3)_2]^{2+}$** **DDP_2PHEN**

Figure 6: Ruthenium and Rhodium Cages

1.2.2 Unlockable Metal Cages Type 2: Photoactive Metal

In the second type of unlockable cage, the metal acts as the photo-protecting group that cages a biologically active molecule. The concept here is that irradiation changes the coordination around the metal center to release (i.e. uncage) a molecule that has biological activity. A key difference from Type 1 is that the bioactivity of the released ligand is the focus, as opposed to changes at the metal center.

1.2.2.1 Ruthenium Cages

Recognizing that the $Ru^{II}(bpy)_2$ core is photosensitive, Etchenique and coworkers coordinated amine-containing neurochemicals to open sites on the octahedral Ru^{II} center to keep them biologically unavailable. Irradiation into the metal-to-ligand charge transfer (MLCT) of the $Ru^{II}(bpy)_2$ center induces decomposition of the $[Ru(bpy)_2(X)_2]$ complex, where X is a neurochemical, to release $[Ru(bpy)_2(X)]$ and one equivalent of neurochemical, as shown in Scheme 8. Ru was employed to cage various amine-containing neurotransmitters including 4-aminopyridine (4AP), serotonin, butylamine, tryptamine, and tyramine.[73] The compound where X is 4AP has been shown to operate in a biological system when $[Ru(bpy)_2(4AP)_2]$ is irradiated with visible light > 480 nm and one equivalent of 4AP is released. The free 4AP promotes the activation of a leech neuron by blocking its K^+ channels.[74]

Later, triphenylphosphine, PPh_3, was utilized to form $[Ru(bpy)_2(PPh_3)(X)]$. By incorporating only one equivalent of an amine-containing neurochemical, the quantum yield of photolysis increased from 0.03 for $[Ru(bpy)_2(X)_2]$ to 0.21 for $[Ru(bpy)_2(PPh)(X)]$.[75] When X is γ-aminobutyric acid (GABA), the main inhibitory neurotransmitter in the brain, exposure to light at 450 nm has been shown to activate GABA ion channels in frog oocytes.[75] When applied in the dark, no cellular changes were observed. The system in which non-leaving groups occupy five of the six coordination sites has been used to cage amino acids like glutamate.[76] In this case, one of the bpy and the PPh_3 ligands is replaced by a tridentate chelator, tris(pyrazolyl)amine. To

the best of our knowledge, Ru-caged amino acids have not yet been tested *in vivo*.

There are a number of light-activated biomolecules that cage neurochemicals, similar to that of the light-activated ATP molecule by Kaplan, Forbush, and Hoffman. Like many of the examples discussed in this chapter, these strategies require UV light of ~ 300 nm to break a σ covalent bond, which may cause cellular photodamage. An advantage offered by Ru-based caging groups is therefore their longer wavelength photoreactivity.

Scheme 8: Photolysis of $[Ru(bpy)_2(4AP)_2]$

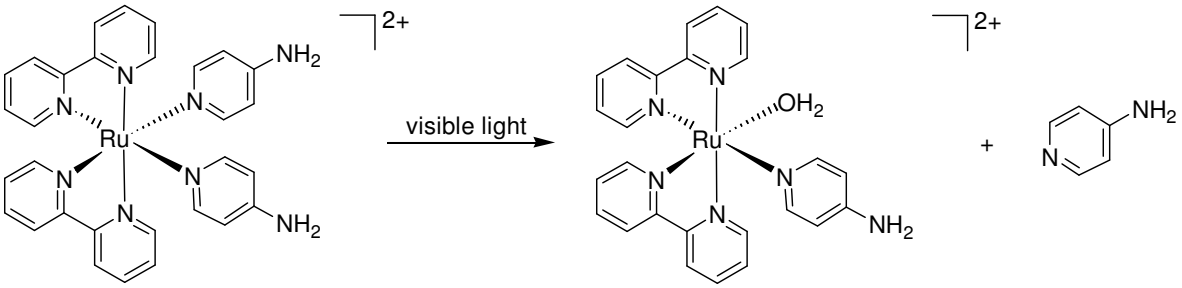

***cis*-$[Ru(bpy)_2(4AP)_2]^{2+}$** ***cis*-$[Ru(bpy)_2(OH_2)(4AP)]^{2+}$**

1.2.2.2 NO Cages

Nitric oxide (NO) is a signaling molecule implicated in various physiological responses including blood pressure regulation, neurotransmission, immune response, and cell death.[77] Metal complexes containing a metal-nitrosyl (M-NO) bond have been

implemented to liberate NO as a therapeutic agent or to investigate the roles of NO in biological pathways. The first metal-containing NO-releasing drug, $Na_2[Fe(NO)(CN)_5]$, while clinically useful for the reduction of hypertension, is not without drawbacks as the loss of its ancillary ligands causes cyanide toxicity.[78,79] As a result, much effort has been dedicated to the development of new metal complexes with improved stability to prevent the loss of supporting ligands and for the controlled delivery of NO. In particular, the known photosensitivity of many M-NO compounds makes light an ideal trigger for the release of NO in a spatial and temporal specific manner.

Mascharak and coworkers developed octahedral metal complexes containing $PaPy_3H$ (N,N-bis(2-carboxamide), a pentadentate ligand, and NO. Both the ruthenium[80] and manganese complexes[81], shown in Figure 7, were found to be stable at physiologically relevant pH and are activated with light to release NO. Even though the Ru analog is activated with UV light and the Mn analog is activated with visible light (500 – 650 nm), both have biological application in the activation of soluble guanylate cyclase activity *in vitro*, trigger a concentration-dependent increase in cGMP in vascular smooth muscle cells, and elicit vasorelaxant activity in a rat thoracic ring.[82]

Variations of the coordinating ligands have been shown to red shift the wavelengths needed for photoactivation. The coordination of a dye to the metal center not only alters the photochemical properties of the metal complex but also provides a means to monitor cellular distribution. Along these lines, Ford and coworkers incorporated chromophores such as, AFchromophore[83], fluorescein[84,85], and

protoporphyrin IX[86] into their metal complexes to increase light absorption and improve NO release at longer wavelengths. Although NO release is not very efficient, these complexes have a two-photon cross section that enables NO release with two-photon excitation with 810 nm femtosecond pulsed light.[87]

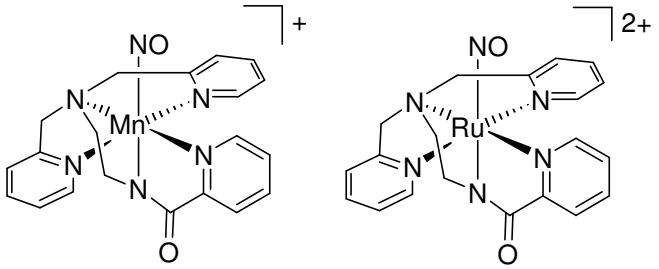

$[Mn(PaPy_3)(NO)]^+$ $[Ru(PaPy_3)(NO)]^{2+}$

Figure 7: Light-Activated NO-Releasing Cages

1.2.2.3 CO Cages

Carbon monoxide (CO) is an important signaling molecule that is implicated in some of the same pathways as NO, as well as other physiological processes.[88] Like NO, the controlled release of CO can be used to study the roles of CO in various pathways or administered as a therapeutic agent. In an effort to control the release of high concentrations of CO, Schatzschneider and coworkers introduced a photolabile octahedral Mn complex,[89] shown in Figure 8. $[Mn(CO)_3(tpm)]^+$ has been shown to release two equivalents of CO to myoglobin upon activation with 365 nm light. *In vivo*,

this compound is non-toxic to human colon cancer cells in the dark, however in the presence of light it displays photoinitated cytotoxicity.[83]

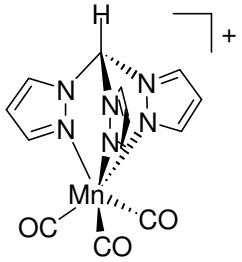

[Mn(CO)$_3$(tpm)]$^+$

Figure 8: Light-Activated CO-Releasing Cage

1.3 Summary and Outlook

As discussed in the previous sections, photolabile metal cages can be used as tools for manipulating the bioavailability of metals or their coordinating ligands in order to study biological pathways or for therapeutic purposes. The remainder of this dissertation investigates uncaging d-block metal ions using a photoactive ligand. In particular, Chapter 2 details the first example reported in the literature of photocaging a biologically important d-block metal ion, Cu^{2+}. To better understand the scope of different biological applications for photolabile transition metal cages we first set out to answer the question: can caged transition metals be used to induce cell death only upon activation with light? This question is answered in Chapter 3 with a photoactive Pt^{II} compound. Next, we

probed the question: can photocaged compounds be used to study intracellular transition metal distribution? Chapter 4 investigates this question using a fluorescent photocaged copper complex that provides a turn-on reponse with UV activation. Finally, Chapter 5 investigates how modifications to our parent caging structure can tune quantum efficiency and metal binding affinity.

2. A Photolabile Ligand for Light-Activated Release of Caged Copper[1]

2.1 Background and Significance

The redox activity of copper makes it an essential cofactor in numerous enzymes critical for life, but also renders it potentially toxic by promoting the formation of reactive oxygen species (ROS) that lead to cellular oxidative stress.[90,91] Understanding the trafficking pathways by which cells and organisms acquire, maintain, and utilize copper while suppressing its toxicity has important ramifications for health and disease.[92,93] Copper's pro-oxidant property is also medicinally promising if it could be harnessed to induce oxidative stress as a cancer chemotherapy strategy.[94-96] New reagents that could deliver copper intracellularly in a site and time specific manner would therefore be useful both for targeted delivery of ROS-active agents and for delineating copper trafficking and utilization pathways. Toward these goals, we present here a caged copper complex in which a photoactive nitrophenyl group is incorporated into the backbone of a tetradentate chelator with high affinity for copper. Activation with UV light induces bond cleavage that releases bidentate components with low affinity for copper (Scheme 9).

The concept of light-activated caged metal ions was first introduced for Ca^{2+}.[12,13,15,16] Caged calcium, in which stable coordination complexes are activated by

[1] Reproduced in part with permission from Ciesienski, K. L.; Haas, K. L.; Dickens, M. G.; Tesema, Y. T. and Franz, K. J. *J. Am. Chem. Soc.* **2008**, *130*, 12246-12247. Copyright 2008 American Chemical Society.

UV light to release Ca^{2+} ions intracellularly, have found widespread use in understanding the many roles of Ca^{2+} in neurotransmission, muscle contraction, and other biological processes.[15,16] The carboxylate-rich chelators used to cage Ca^{2+} have also been used for Sr^{2+}, Ba^{2+}, Mg^{2+}, Cd^{2+}, Mn^{2+}, and Co^{2+},[24] while photo-cleavable cryptands have been reported to release alkali ions[23] and a photoactive crown ether shows modest reversible photorelease of Sr^{2+}.[25] Because Cu^{2+}–carboxylate complexes are themselves photoactive to release CO_2 and carbon-centered radicals,[97] carboxylate ligands are not ideal for caging copper. We therefore chose a nitrogen-rich bispyridylamide ligand (H_2cage) for our first-generation caged copper.

Scheme 9: Synthesis and Photolysis of [Cu(OH$_2$)(cage)]

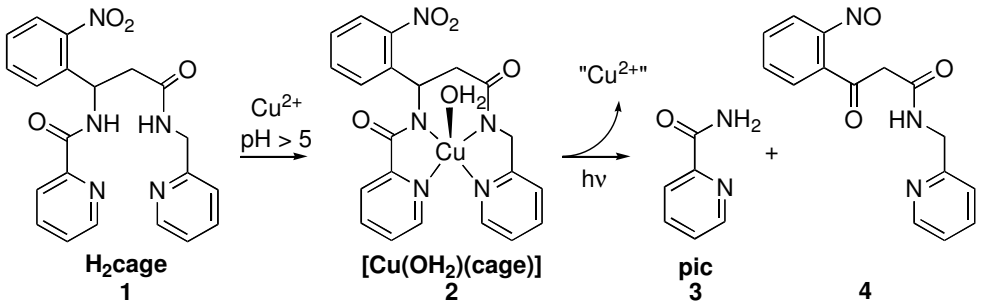

H$_2$cage
1

[Cu(OH$_2$)(cage)]
2

pic
3

4

2.2 Materials and Methods

2.2.1 Materials and Instrumentation

All chemicals were purchased commercially and used without further purification. N-Methylmorpholine (NMM), 2-deoxy-D-ribose, ascorbic acid, 50% hydrogen peroxide, trichloroacetic acid (TCA), and 2-thiobarbituric acid (TBA) were purchased from Acros Organics; picolinic acid, 2-(aminomethyl)pyridine, picolinamide, and $CuSO_4 \cdot 5H_2O$ from Sigma-Aldrich; nitrilotriacetic acid (NTA) from Fluka; 3-amino-3-(2-nitrophenyl)propionic acid from Alfa Aesar, and benzotriazol-yloxytris(dimethyl-amino) phosphoniumhexafluorophosphate (BOP) from Novabiochem. All solvents were reagent grade. Chromatographic purification was carried out on basic aluminum oxide (50-200 micron) from Acros Organics. ^{1}H NMR and ^{13}C NMR spectra were collected on a Varian Inova 400 spectrometer with chemical shifts reported in ppm and J values in Hz. Elemental analysis was performed by Columbia Analytical Services, Inc. IR spectra were measured on a Nicolet 380 FT-IR. High-resolution, fast-atom bombardment (HR-FABMS) mass spectra were recorded on JEOL JMS-SX-102 instrument. Liquid chromatography-electrospray mass spectrometry (LC/MS) was performed using an Agilent 1100 Series apparatus with an LC/MSD trap and a Daly conversion dynode detector. A Varian Polaris C18 (150 × 1.0 mm) column was used and peaks were detected by UV absorption at 254 nm. A linear gradient from 10% A in B to 60% A in B was run from 2 to 18 min with a total run time of 20 min, where A is MeCN / 4% 10 mM ammonium acetate buffer and B is 10 mM ammonium acetate buffer / 2% MeCN. UV-

vis spectra were recorded on a Cary 50 UV-vis spectrophotometer. Photolysis experiments were performed using a screwtop quartz cuvette illuminated in a Rayonet RPR-100 Photochemical Reactor containing 16 bulbs, each 3500 Å.

2.2.2 Synthesis

Scheme 10: Synthesis of H_2cage

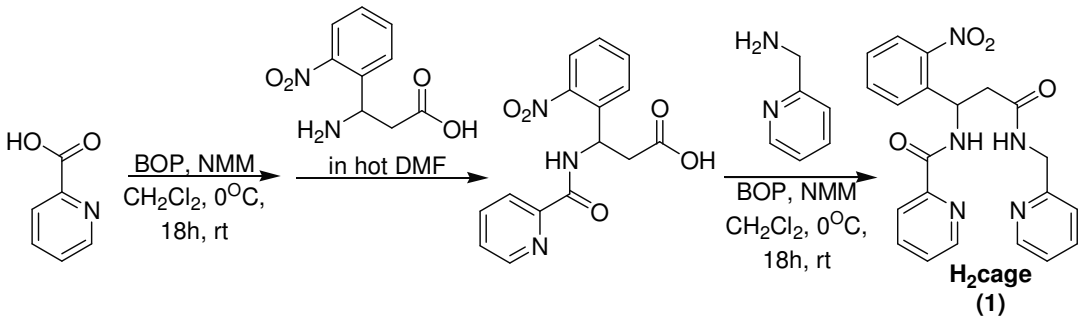

2.2.2.1 Pyridine-2-carboxylic acid {1-(2-nitro-phenyl)-2-[(pyridine-2-ylmethyl)-carbamoyl]-ethyl}-amide (H_2cage)

Equimolar quantities of picolinic acid (0.100 g, 0.813 mmol) and NMM (0.089 mL, 0.813 mmol) in CH_2Cl_2 (3 mL) were added to a 50-mL round-bottom flask equipped with a stir bar. The reaction mixture was cooled over an ice bath for ten min then BOP (0.360 g, 0.813 mmol) in CH_2Cl_2 (2 mL) was added. The reaction mixture was allowed to warm to room temperature with stirring for 18 h. After 18 h, one equivalent of 3-amino-

3-(2-nitrophenyl)propionic acid (0.171 g, 0.813 mmol) dissolved in hot DMF (15 mL) was added and the reaction mixture was stirred for an additional 18 h. NMM (0.089 mL, 0.813 mmol) and 2-(aminomethyl)pyridine (0.083 mL, 0.813 mmol), both in CH_2Cl_2 (3 mL) were added to the reaction mixture. The resulting solution was cooled over an ice bath for ten min then BOP (0.360 g, 0.813 mmol) in CH_2Cl_2 (2 mL) was added, and the reaction mixture stirred for 18 h at room temperature. The solvent was removed and the resulting oil was taken up in CH_2Cl_2 (25 mL), filtered, and washed with saturated aqueous NaCl solution (3 × 10 mL). The organic layers were combined, dried over $MgSO_4$, filtered, and solvent removal gave an oil that was purified by chromatography (basic alumina, EtOAc:hexanes, 8:2, R_f = 0.37), giving a white crystalline solid (0.220 g, 67%). ^{1}H NMR (CD_3OD): δ 8.69 (1H, d, *J* = 4.77), 8.42 (1H, d, *J* = 4.93), 8.03 (2H, dd, *J* = 4.65, *J* = 7.97), 7.95 (1H, td, *J* = 1.66, *J* = 7.68, *J* = 7.80), 7.74 (1H, d, *J* = 6.77), 7.61 (3H, m), 7.53 (1H, dd, *J* = 4.31, *J* = 11.17), 7.25 (1H, m), 7.17 (1H, d, *J* = 7.88), 6.08 (1H, dd, *J* = 5.06, *J* = 7.09), 4.47 (2H, dd, *J* = 15.91, *J* = 42.40), 3.11 (2H, qd, *J* = 6.11, *J* = 14.80, *J* = 14.81, *J* = 14.81). ^{13}C NMR ($CDCl_3$): δ 40.5, 44.1, 47.6, 122.1, 122.2, 122.5, 124.9, 126.3, 128.3, 129.1, 133.6, 137.0, 137.2, 137.3, 148.2, 148.5, 148.6, 149.6, 155.8, 164.0, 170.4; HR-FABMS: m/z 406.11 $[M+H]^+$, calcd 405.14 for M = $C_{21}H_{19}N_5O_4$; IR (MeOH, cm^{-1}): 3309, 1658, 1520, 1433, 1349, 731; UV-vis (3% MeOH in H_2O, pH 6–12), nm ($M^{-1}cm^{-1}$): 270 (8,500), 300 (1,800).

Scheme 11: Synthesis of [Cu(OH2)(cage)]

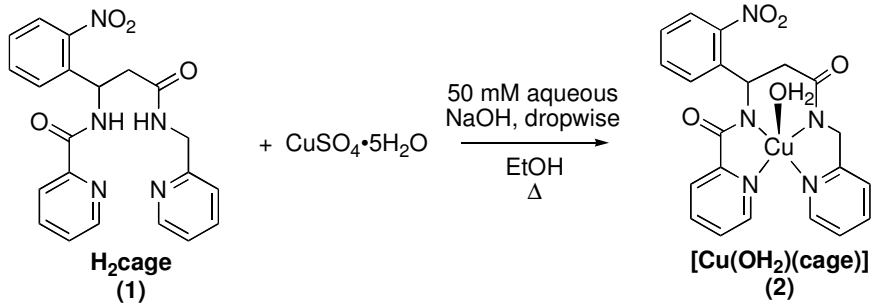

2.2.2.2 [Cu(OH2)(cage)]

A 50 mM aqueous solution of NaOH (9.38 mL) was added dropwise to a refluxing solution of H_2cage (0.095 g, 0.234 mmol) and $CuSO_4$•$5H_2O$ (0.058 g, 0.234 mmol) in 25 mL of EtOH. After refluxing for 1 h, the solvent was removed and the residue was taken up in acetone and filtered. Slow evaporation gave blue, prism-shaped crystals in 81% yield. ESI-MS: m/z 467.0 $[M+H]^+$ for [Cu(cage)], calcd 466.06 for $C_{21}H_{17}CuN_5O_4$; IR (neat, cm-1): 1579, 1556, 1515, 1375, 1346, 1018, 755, 716, 698, 672, 647; UV-vis (H_2O, pH 6–12), nm (M-1cm-1): 580 (112); Anal. calcd. for $C_{21}H_{17}CuN_5O_4 \cdot 2H_2O$: C, 50.15; H, 4.21; N, 13.92; found: C, 51.86; H, 4.25; N, 13.97%.

2.2.3 Deoxyribose Assay

The 2-deoxyribose assay was used to measure hydroxyl radical formation.[98] A mixture of copper, ascorbic acid, and hydrogen peroxide generates hydroxyl radicals by

Fenton-like chemistry. Hydroxyl radicals attack 2-deoxyribose to form malondialdehyde (MDA), which upon heating with TBA under acidic conditions produces a pink chromophore (λ_{max} = 532 nm). Chelators that prevent copper from reacting with ascorbic acid and hydrogen peroxide result in less chromophore formation. All assays were performed using 20 mM NaH_2PO_4 buffered to pH 7.4. The following reagents were added sequentially to obtain a 1 mL buffered solution with these final concentrations: chelator (10–20 μM), $CuSO_4$ (10 μM), 2-deoxyribose (15 mM), H_2O_2 (100 μM), and ascorbic acid (2 mM). For photolyzed samples, 500 μM solutions of [$Cu(OH_2)$(cage)] in 20 mM pH 7.4 NaH_2PO_4 buffer were photolyzed in 1-cm screwtop quartz cuvettes for 4 min in the photoreactor, then immediately diluted into the deoxyribose reaction mixtures to obtain final Cu concentrations of 10 μM. Stock solutions of $CuSO_4$, ascorbic acid, and H_2O_2 were prepared fresh daily, other solutions were prepared weekly. The reaction mixtures were stirred at 37 °C for 1 h, then 1 mL of TBA (1% w/v in 50 mM NaOH) and 1 mL of TCA (2.8% w/v in water) were added. The temperature was increased to 100 °C for 20 min, then cooled to room temperature and the absorbance at 532 nm was recorded. Values are reported as A/A_0 where A_0 is the absorbance without chelator present and A is the absorbance with chelator added. The value for $CuSO_4$ alone is $A/A_0 = 1$. Error bars represent standard deviations from measurements done in at least triplicate.

2.2.4 Quantum Yield

The quantum yields of H_2cage and [Cu(OH_2)(cage)] photolysis were determined by comparison to the quantum yield of 1-(o-nitrophenyl)ethyl phosphate (cage P_i) as previously reported by Ellis-Davis and Kaplan.[99] Samples of H_2cage (500 μM, A_{350} = 0.030), [Cu(OH_2)(cage)] (500 μM, A_{350} = 0.040), or caged P_i (1 mM, A_{350} = 0.065) in 20 mM NaH_2PO_4 buffer pH 7.4 were irradiated in a Rayonet RPR-100 Photochemical Reactor at 350 nm for 15 s. Photodegradation of caged compounds was monitored by LC-MS analysis. Aliquots of 3.0 μL of each sample before and after photolysis were injected by autoinjector and run in triplicate. The experiment was repeated to ensure reproducibility. The quantum yield for each sample (Φ_{sample}) was calculated by using Equation 1:

$$\Phi_{sample} = \Phi_{cp} \times \frac{\%\Delta sample}{\%\Delta cp} \times \frac{A_{350}cp}{A_{350}sample} \quad (1)$$

where Φ_{cp} is 0.54, the previously determined quantum yield of photolysis for caged P_i,[99] %Δsample and %Δcp are the percent change in integrated peak area after photolysis for the sample and caged P_i, respectively, and A_{350} is the absorbance at 350 nm in a 1-mm cuvette for caged P_i (cp) and for the sample.

2.2.5 Potentiometric and Spectrophotometric Titrations

Kathryn Haas, a graduate student in the Franz laboratory, performed the

potentiometric and spectrophotometric titrations described below. Cu^{II} perchlorate solutions (0.1 M) were prepared from solid $Cu(ClO_4)_2 \bullet 6H_2O$ and standardized with 0.05 M EDTA to a murexide endpoint in ammonia buffer. NaOH, $HClO_4$, and $NaClO_4$ solutions (0.1 M) were prepared with boiled nanopure deionized water and were degassed upon cooling to remove dissolved carbonate. NaOH solutions were standardized by titration with both 0.2 M HCl and potassium hydrogen phthalate to a phenolphthalein end point and were stored under Ar; $HClO_4$ stock solutions were prepared from concentrated perchloric acid and standardized by titration with standard NaOH to a phenolphthalein end point. All solutions were degassed with Ar for 45 minutes prior to each experimental run.

Titrations were carried out at 25 °C with 0.1 M $NaClO_4$ supporting electrolyte in a 3-mL cuvette equipped with a pH probe, titrator tip, and stir bar, and blanketed in Ar to preserve an inert environment. The glass-bulb probe (Orion combination pH electrode model 8103BN filled with 3 M NaCl) was calibrated with pH 4 and 7 standard reference buffers (RICCA Chemical Company). Solutions of H_2cage were prepared by dissolving the compound in a minimum volume of MeOH and diluting with 0.1 M $NaClO_4$ in H_2O. Solutions of [$Cu(OH_2)$(cage)] were prepared in the range of 0.5 mM by dissolving the complex, recrystallized from methanol, in 0.1 M $NaClO_4$. Initial volumes were between 2 and 2.2 mL. A Schott Titronic® 110 plus autotitrator kept under constant Ar sparge was used to deliver 2 to 4 µL aliquots of acid or base through the titrator tip into the reaction cuvette. The solutions were stirred constantly and allowed to equilibrate at least

30 s after each addition before data were collected. Titration data were fit using Specfit software (Spectrum Software Associates, version 3.0.30).

2.2.6 Competition Study of Nitrilotriacetic Acid (NTA) vs. H_2cage for Cu^{2+}

Kathryn Haas, a graduate student in the Franz laboratory, performed the competition study described below. Solutions of [Cu(OH_2)(cage)] were prepared by dissolving [Cu(OH_2)(cage)] that was recrystallized from methanol into 50 mM HEPES (N-(2-hydroxyethyl)-piperazine-N'-2-ethanesulfonic acid) buffer, pH 7.4, with initial concentrations ranging from 0.3–1.5 mM. The reaction vessel was a 3-mL cuvette and initial solution volumes were 1 mL. All titrations were carried out at 25 °C. Aliquots (1–2 μL) of the competitive chelator NTA (100 mM) were pipetted into [Cu(OH_2)(cage)] solutions and monitored spectrophotometrically. After each addition, solutions were manually mixed and equilibrated for 5 min before data were collected. Reported errors in log β were calculated from the standard deviation of three runs.

2.2.7 X-Ray Data Collection and Structure Solution Refinement

Marina Dickens, a graduate student in the Franz laboratory, collected and analyzed the data for all crystal structures. Blue prisms of [Cu(OH_2)(cage)] were grown by slow evaporation of acetone. The crystal was mounted on the tip of a glass fiber and held in place by hardened Karo syrup. Data were collected at 296 K on a Bruker Kappa

Apex II CCD diffractometer equipped with a graphite monochromator and a Mo Kα fine-focus sealed tube (λ= 0.71073Å) operated at 1.75 kW power (50 kV, 35 mA). The detector was placed at a distance of 5.010 cm from the crystal. A total of 2655 frames were collected with a scan width of 0.5º and an exposure time of 90.0 sec/frame. The frames were integrated with the Bruker SAINT v7.12A software package using a narrow-frame integration algorithm. Empirical absorption corrections were applied using SADABS v2.10 and the structure was checked for higher symmetry with PLATON v1.07. The structure was solved by direct methods with refinement by full-matrix least-squares based on F^2 using the Bruker SHELXTL Software Package. All non-hydrogen atoms were refined anisotropically. Hydrogen atoms of sp^2 hybridized carbons and nitrogens were located directly from the difference Fourier maps; all others were calculated.

2.3 Results

2.3.1 [Cu(OH$_2$)(cage)] pK$_a$ and log β Determination

Potentiometric titrations for both H$_2$cage and [Cu(OH$_2$)(cage)] were carried out from low to high and from high to low pH with similar results. Figure 9 shows the potentiometric titration curves of H$_2$cage and [Cu(OH$_2$)(cage)] (abbreviated as H$_2$L and CuL, respectively). Titration data of H$_2$cage reveal no ionizable protons in the pH range between 2–12. This is not surprising, based on literature pK$_a$ values of amide protons (pK$_a$ > 20) and relevant substituted pyridine rings (pK$_a$ < 2).[100]

Titration data for the [Cu(OH$_2$)(cage)] complex show two ionizable protons below pH 5. The pH-dependent spectra are shown in Figure 10. These data were fit using Specfit software according to the model in Table 1, where β is defined by Equation 2 for the general equilibrium reaction in Equation 3 where L = cage^{2-}.

$$\beta_{mlh} = \frac{[\mathrm{Cu}_m\mathrm{L}_l\mathrm{H}_h]}{[\mathrm{Cu}]^m[\mathrm{L}]^l[\mathrm{H}]^h} \qquad (2)$$

$$m\mathrm{Cu} + l\mathrm{L} + h\mathrm{H} \rightleftharpoons \mathrm{Cu}_m\mathrm{L}_l\mathrm{H}_h \qquad (3)$$

The Specfit program produced log β values of 15.63 and 18.96 for the CuLH and CuLH$_2$ species respectively, which correspond to the pK$_a$ values of 4.83 and 3.33, consistent with the deprotonation of both amides. Attempts to include the species CuLH$_{-1}$, which

represents the deprotonation of the coordinated water molecule in [Cu(OH_2)(cage)], into the model did not fit the data, indicating that this event is not observable in the tested pH range. The calculated speciation curve is shown in Figure 11.

An overall stability constant of log β = 10.8 was calculated for [Cu(OH_2)(cage)]. This value converts to a conditional dissociation constant, K_d, at 7.4 for Cu-cage of 16 pM. Titration of the common chelator nitrilotriacetic acid (NTA) into a solution of [Cu(OH_2)(cage)], confirmed this value. A typical titration is shown in Figure 12. Data were fit to the model shown in Table 2 with Specfit software.

Table 1: Model Used for the pH-Dependent Spectrophotometric Titrations of CuL

where L = $cage^{2-}$. β is defined in Equation 2.

Species	Log β	Cu m	L l	H h	
CuL	10.80 ± 0.01	1	1	0	refined
CuLH	15.63 ± 0.08	1	1	1	refined
$CuLH_2$	18.96 ± 0.03	1	1	2	refined
CuOH	-8.2	1	0	-1	constant[19]
$Cu(OH)_2$	-17.5	1	0	-2	constant[19]
$Cu(OH)_3$	-27.8	1	0	-3	constant[19]
$Cu(OH)_4$	-39.1	1	0	-4	constant[19]
OH	-13.74	0	0	-1	constant[18]

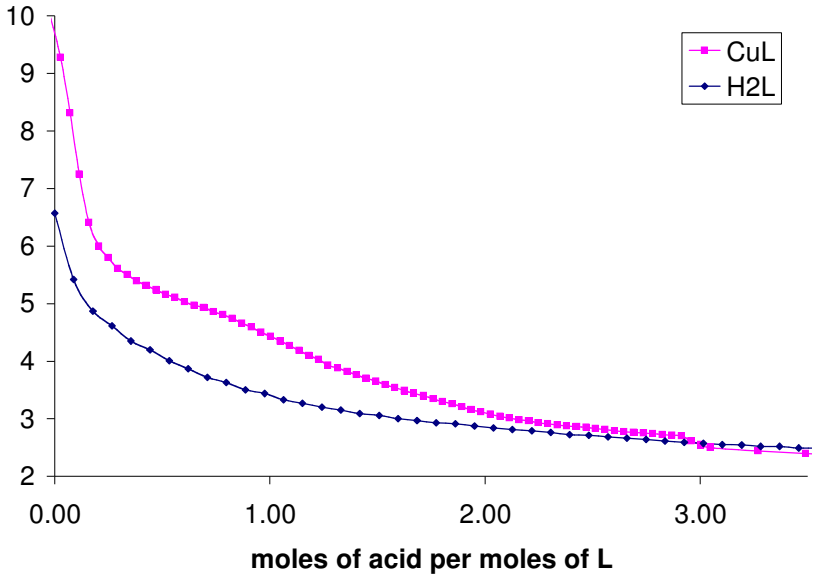

Figure 9: Potentiometric Titration Curves for H_2L and CuL

Potentiometric titration curves of H_2L (blue diamonds, [L] = 1.46 mM) and CuL (pink squares, [CuL] = 1.33 mM), where L = $cage^{2-}$. T = 25 °C, μ = 0.1 M $NaClO_4$.

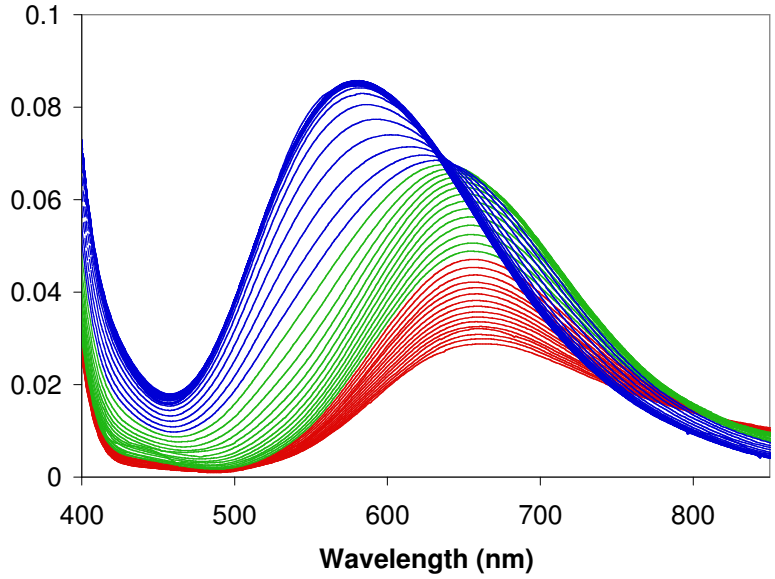

Figure 10: pH-Dependent Spectrophotometric Titration of [Cu(OH$_2$)(cage)]

Titration was carried out from pH 2.7 to 12. T = 25 °C, [Cu] = [cage] = 0.71 mM, μ = 0.1M $NaClO_4$.

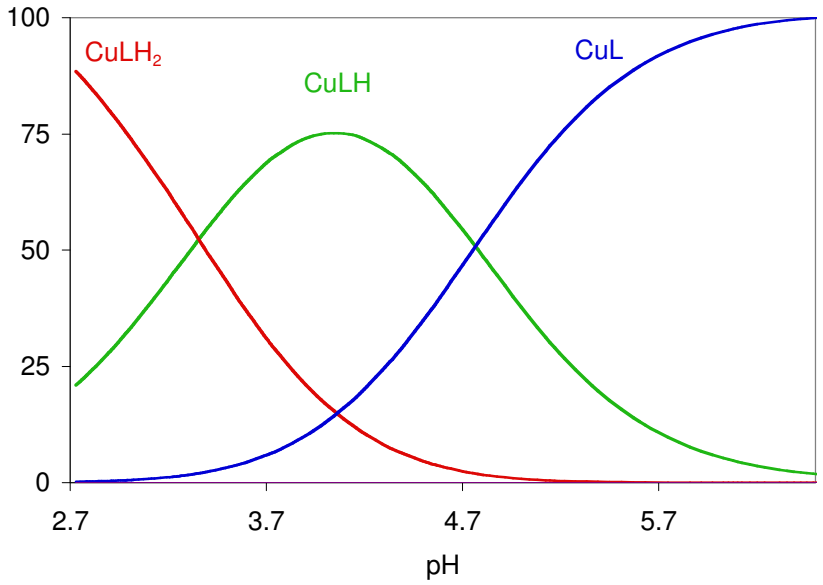

Figure 11: Speciation Curve for CuL

Calculated species distribution for Cu^{2+} complexes of L, L = $cage^{2-}$. Conditions as described in Figure 9.

Table 2: Model for the Cu^{2+} Competition Study of NTA vs. L

L = $cage^{2-}$ and β is defined in Equation 2

Species	Log β	Cu m	NTA l	L l	H h	
CuL	10.79± 0.06	1	0	1	0	refined
Cu(NTA)	12.7	1	1	0	0	constant[18]
$Cu(NTA)_2$	17.4	1	2	0	0	constant[18]
NTAH	9.46	0	1	0	1	constant[18]
$NTAH_2$	11.95	0	1	0	2	constant[18]
$NTAH_3$	13.76	0	1	0	3	constant[18]
$NTAH_4$	14.76	0	1	0	4	constant[19]
CuOH	-8.2	1	0	0	-1	constant[20]

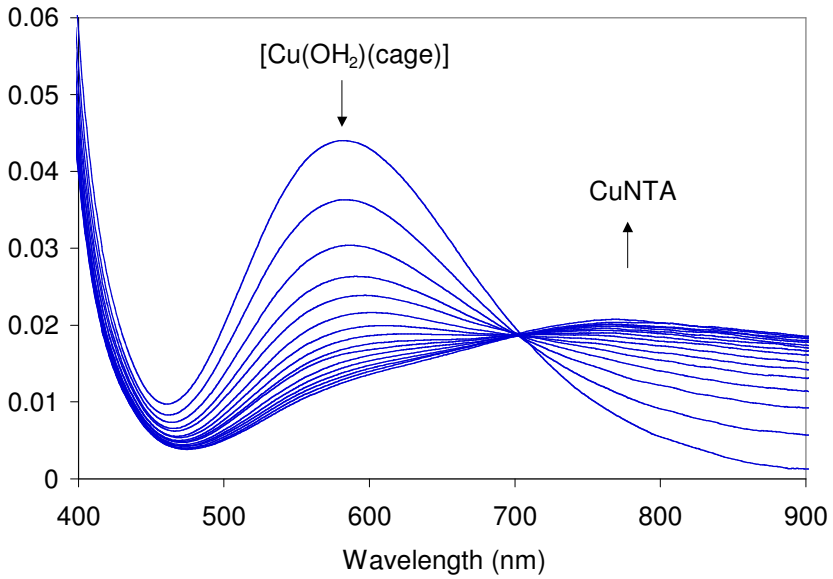

Figure 12: Competition Experiment of NTA vs. H_2cage for Cu^{2+}

Titration of NTA into a 0.39 mM solution of [Cu(OH_2)(cage)] in 50 mM HEPES buffer.

2.3.2 Crystal Structure of [Cu(OH_2)(cage)]

Recrystallization of [Cu(OH_2)(cage)] from acetone in the presence of base confirmed that 2 deprotonated amide nitrogens and 2 pyridyl nitrogens coordinate Cu^{2+} in a distorted trigonal bipyramidal geometry, with a water molecule lying in the trigonal plane at a Cu–O distance of 2.299(3) Å. The average Cu–N_{amide} distance of 1.943 Å and Cu–$N_{pyridine}$ distance of 2.034 Å are similar to other bispyridylamide Cu^{2+} complexes.[99] Figure 13 shows the fully labeled structure with select bond distances and angles. Table 3 contains a summary of crystal data, intensity collection and structure refinement parameters. Bond lengths and angles are listed in Table 4.

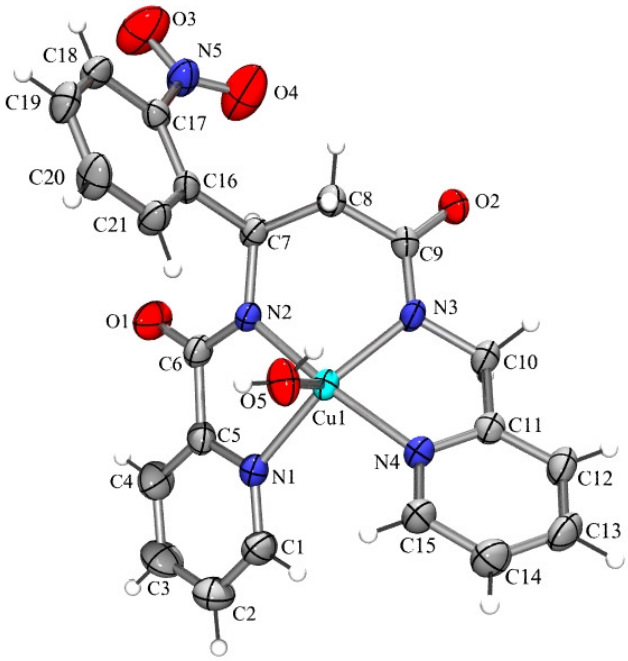

Figure 13: ORTEP Diagram of [Cu(OH_2)(cage)]

ORTEP diagram of [Cu(OH_2)(cage)] showing 50% thermal ellipsoids. Selected bond distances: Cu–N1, 2.052(2); Cu–N2, 1.948(3); Cu–N3, 1.943(3); Cu–N4, 2.013(3), Cu–O5, 2.295(3) Å. Distance between the ortho H's on C1 and C15 (H1–H15), 2.4955 Å. Selected bond angles: N2–Cu–N4, 172.8(1); O5–Cu–N3, 117.0(1); O5–Cu–N1, 100.9(1); N1–Cu–N3, 141.9(1); N2–Cu–N3, 92.9(1); N3–Cu–N4, 80.8(1); N1–Cu–N4, 100.7(1); N2–Cu–N1, 82.1(1); N2–Cu–O5, 100.8(1); O5–Cu–N4, 85.3(1)°.

Table 3: **Crystal Data and Structure Refinement for [Cu(OH$_2$)(cage)]**

Identification code	md54	
Empirical formula	$C_{21}H_{19}N_5O_5Cu$	
Formula weight	484.95	
Temperature	296(2) K	
Wavelength	0.71073 Å	
Crystal system	Monoclinic	
Space group	P2(1)/n	
Unit cell dimensions	a = 7.7037(4) Å	α = 90°
	b = 12.2546(8) Å	β = 95.364(3) °
	c = 21.0831(12) Å	γ = 90°
Volume	1981.6(2) Å^3	
Z	4	
Density (calculated)	1.625 Mg/m^3	
Absorption coefficient	1.149 mm^{-1}	
F(000)	996	
Crystal size	0.12 x 0.05 x 0.04 mm^3	
Crystal color and habit	Blue prism	
Diffractometer	Bruker Kappa Apex II	
Theta range for data collection	1.92 to 24.96°	
Limiting indices	-9<=h<=8, -14<k<=14, -25<=l<=25	
Reflections collected	30154	
Independent reflections	3429 [R(int) = 0.0815]	
Completeness to theta = 24.96	98.9 %	
Absorption correction	Semi-empirical from equivalents	
Max. and min. transmission	0.9555 and 0.8744	
Solution method	SHELXS-97 (Sheldrick, 1990)	
Refinement method	SHELXL-97 (Sheldrick, 1997)	
Data / restraints / parameters	3429 / 0 / 293	
Goodness-of-fit on F^2	1.152	
Final R indices [I>2σ(I)]	R1 = 0.0410, wR2 = 0.0983	
R indices (all data)	R1 = 0.0664, wR2 = 0.1093	
Largest diff. peak and hole	0.773 and -0.333 e·Å^{-3}	

Table 4: Bond Lengths [Å] and Angles [°] for [Cu(OH$_2$)(cage)]

Cu(1)-N(2)	1.944(3)	C(4)-H(4A)	0.93
Cu(1)-N(3)	1.943(3)	C(5)-C(6)	1.510(5)
Cu(1)-N(4)	2.013(3)	C(7)-C(8)	1.534(5)
Cu(1)-N(1)	2.054(3)	C(7)-C(16)	1.536(5)
Cu(1)-O(5)	2.295(3)	C(7)-H(7A)	0.98
O(1)-C(6)	1.241(4)	C(8)-C(9)	1.517(4)
O(2)-C(9)	1.253(4)	C(8)-H(8A)	0.97
O(3)-N(5)	1.202(4)	C(8)-H(8B)	0.97
O(4)-N(5)	1.193(4)	C(10)-C(11)	1.499(5)
O(5)-H(5A)	0.82	C(10)-H(10A)	0.97
O(5)-H(5B)	0.69(4)	C(10)-H(10B)	0.97
N(1)-C(1)	1.324(5)	C(11)-C(12)	1.370(5)
N(1)-C(5)	1.338(4)	C(12)-C(13)	1.375(5)
N(2)-C(6)	1.317(4)	C(12)-H(12A)	0.93
N(2)-C(7)	1.460(4)	C(13)-C(14)	1.375(5)
N(3)-C(9)	1.306(4)	C(13)-H(13A)	0.93
N(3)-C(10)	1.453(4)	C(14)-C(15)	1.369(5)
N(4)-C(15)	1.341(4)	C(14)-H(14A)	0.93
N(4)-C(11)	1.344(4)	C(15)-H(15A)	0.93
N(5)-C(17)	1.457(4)	C(16)-C(17)	1.389(4)
C(1)-C(2)	1.365(6)	C(16)-C(21)	1.390(5)
C(1)-H(1A)	0.93	C(17)-C(18)	1.393(5)
C(2)-C(3)	1.372(6)	C(18)-C(19)	1.367(5)
C(2)-H(2A)	0.93	C(18)-H(18A)	0.93
C(3)-C(4)	1.382(6)	C(19)-C(20)	1.360(5)
C(3)-H(3A)	0.93	C(19)-H(19A)	0.93
C(4)-C(5)	1.371(5)	C(20)-C(21)	1.380(5)
C(20)-H(20A)	0.93	C(21)-H(21A)	0.93
N(2)-Cu(1)-N(3)	92.90(11)	C(2)-C(1)-H(1A)	118.2
N(2)-Cu(1)-N(4)	172.75(11)	C(3)-C(2)-C(1)	118.8(4)

Table 4 continued.

N(3)-Cu(1)-N(4)	80.80(11)	C(3)-C(2)-H(2A)	120.6
N(2)-Cu(1)-N(1)	82.02(12)	C(1)-C(2)-H(2A)	120.6
N(3)-Cu(1)-N(1)	141.94(12)	C(2)-C(3)-C(4)	118.3(4)
N(4)-Cu(1)-N(1)	100.70(12)	C(2)-C(3)-H(3A)	120.8
N(2)-Cu(1)-O(5)	100.82(11)	C(4)-C(3)-H(3A)	120.8
N(3)-Cu(1)-O(5)	117.00(12)	C(5)-C(4)-C(3)	119.3(4)
N(4)-Cu(1)-O(5)	85.32(11)	C(5)-C(4)-H(4A)	120.4
N(1)-Cu(1)-O(5)	100.95(11)	C(3)-C(4)-H(4A)	120.4
Cu(1)-O(5)-H(5A)	109.5	N(1)-C(5)-C(4)	122.2(4)
Cu(1)-O(5)-H(5B)	132(4)	N(1)-C(5)-C(6)	116.2(3)
H(5A)-O(5)-H(5B)	109.9	C(4)-C(5)-C(6)	121.6(3)
C(1)-N(1)-C(5)	117.8(3)	O(1)-C(6)-N(2)	127.4(3)
C(1)-N(1)-Cu(1)	130.9(3)	O(1)-C(6)-C(5)	119.1(3)
C(5)-N(1)-Cu(1)	110.7(2)	N(2)-C(6)-C(5)	113.5(3)
C(6)-N(2)-C(7)	115.8(3)	N(2)-C(7)-C(8)	110.5(3)
C(6)-N(2)-Cu(1)	116.6(2)	N(2)-C(7)-C(16)	111.9(3)
C(7)-N(2)-Cu(1)	125.6(2)	C(8)-C(7)-C(16)	106.4(3)
C(9)-N(3)-C(10)	120.2(3)	N(2)-C(7)-H(7A)	109.3
C(9)-N(3)-Cu(1)	125.4(2)	C(8)-C(7)-H(7A)	109.3
C(10)-N(3)-Cu(1)	113.3(2)	C(16)-C(7)-H(7A)	109.3
C(15)-N(4)-C(11)	118.3(3)	C(9)-C(8)-C(7)	116.6(3)
C(15)-N(4)-Cu(1)	127.9(2)	C(9)-C(8)-H(8A)	108.1
C(11)-N(4)-Cu(1)	113.7(2)	C(7)-C(8)-H(8A)	108.1
O(4)-N(5)-O(3)	120.8(3)	C(9)-C(8)-H(8B)	108.2
O(4)-N(5)-C(17)	120.2(3)	C(7)-C(8)-H(8B)	108.2
O(3)-N(5)-C(17)	118.9(3)	H(8A)-C(8)-H(8B)	107.3
N(1)-C(1)-C(2)	123.6(4)	O(2)-C(9)-N(3)	125.4(3)
N(1)-C(1)-H(1A)	118.2	O(2)-C(9)-C(8)	119.5(3)
N(3)-C(9)-C(8)	115.0(3)	N(4)-C(15)-H(15A)	118.7
N(3)-C(10)-C(11)	107.4(3)	C(14)-C(15)-H(15A)	118.7
N(3)-C(10)-H(10A)	110.2	C(17)-C(16)-C(21)	115.2(3)

Table 4 continued.

C(11)-C(10)-H(10A)	110.2	C(17)-C(16)-C(7)	126.6(3)
N(3)-C(10)-H(10B)	110.2	C(21)-C(16)-C(7)	118.0(3)
C(11)-C(10)-H(10B)	110.2	C(16)-C(17)-C(18)	123.1(3)
H(10A)-C(10)-H(10B)	108.5	C(16)-C(17)-N(5)	122.5(3)
N(4)-C(11)-C(12)	121.6(3)	C(18)-C(17)-N(5)	114.4(3)
N(4)-C(11)-C(10)	115.8(3)	C(19)-C(18)-C(17)	118.9(3)
C(12)-C(11)-C(10)	122.5(3)	C(19)-C(18)-H(18A)	120.6
C(11)-C(12)-C(13)	120.0(4)	C(17)-C(18)-H(18A)	120.6
C(11)-C(12)-H(12A)	120	C(18)-C(19)-C(20)	120.0(3)
C(13)-C(12)-H(12A)	120	C(18)-C(19)-H(19A)	120
C(14)-C(13)-C(12)	118.4(4)	C(20)-C(19)-H(19A)	120
C(14)-C(13)-H(13A)	120.8	C(19)-C(20)-C(21)	120.5(3)
C(12)-C(13)-H(13A)	120.8	C(19)-C(20)-H(20A)	119.7
C(13)-C(14)-C(15)	119.2(4)	C(21)-C(20)-H(20A)	119.8
C(13)-C(14)-H(14A)	120.4	C(20)-C(21)-C(16)	122.3(3)
C(15)-C(14)-H(14A)	120.4	C(20)-C(21)-H(21A)	118.9
N(4)-C(15)-C(14)	122.5(3)	C(16)-C(21)-H(21A)	118.9

2.3.3 Photolysis of [Cu(OH_2)(cage)]

When solutions of [Cu(OH_2)(cage)] in pH 7.4 phosphate buffer are exposed to 350 nm UV light, changes in its UV-vis spectra are apparent within seconds, with a shift in the d-d band centered at 580 nm indicating a reorganization of the coordination sphere (Figure 14). Under our photolysis conditions, cleavage of the ligand backbone is complete within 4 min, as confirmed by LC-MS analysis shown in Figures 15 and 16. The band for the intact Cu complex **2** disappears and is replaced by bands corresponding to the expected photoproducts **3** and **4**, as confirmed by their mass spectra and by comparison to a picolinamide standard for **3**. The uncaged copper is likely bound to these photoproducts in solution, but with significantly diminished affinity compared to the intact ligand **1**, as the log β values for picolinamide are only 2.87 and 5.40 for the 1:1 and 1:2 species.[99]

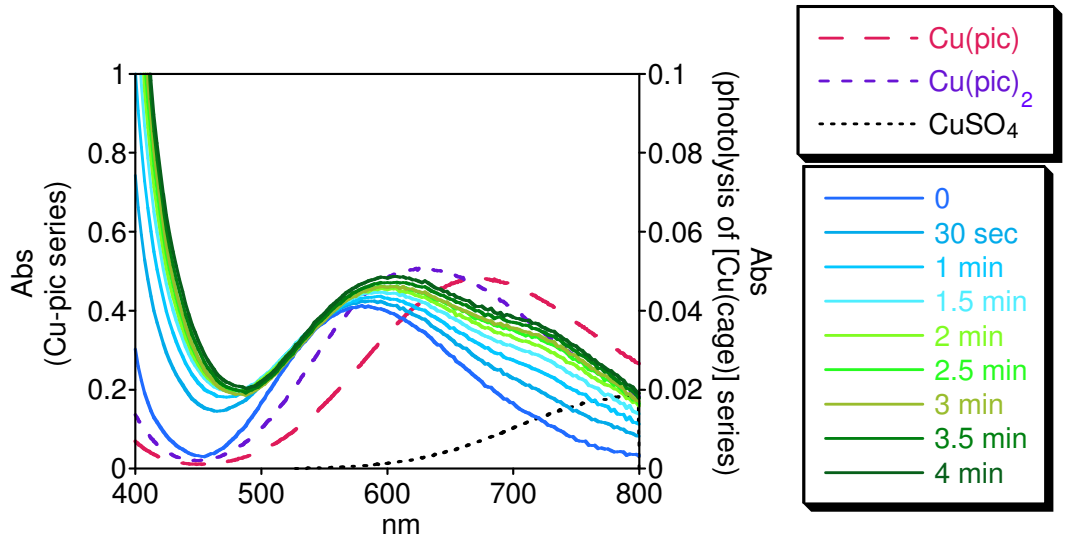

Figure 14: Absorption Spectra for Photolysis of [Cu(OH$_2$)(cage)]

Absorption spectra showing the changes in the Cu^{2+} d-d region for a 350 µM solution of [Cu(OH$_2$)(cage)] in 20 mM NaH_2PO_4 buffer pH 7.4 (t = 0) following 30 sec intervals of photolysis for a total of 4 min of UV exposure. The spectra of $CuSO_4$ alone and in the presence of one and two equivalent of picolinamide are also shown for comparison.

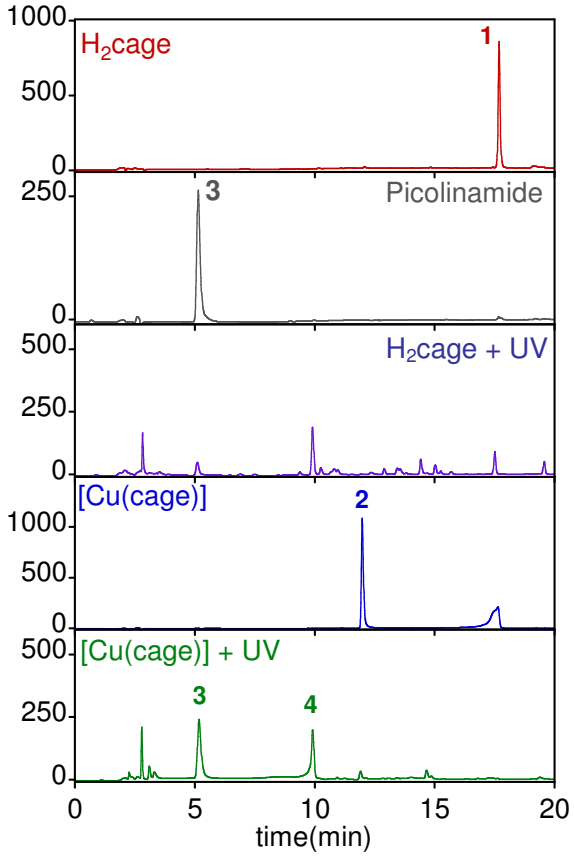

Figure 15: Chromatography Traces for the Photolysis of H_2cage and [Cu(OH_2)(cage)]

Chromatography traces for H_2cage (**1**), standard picolinamide (**3**), [Cu(cage)] (**2**), and [Cu(cage)] + UV are shown here to compare to the trace for H_2cage after 4 min of exposure to UV light (H_2cage + UV), which gives major photolysis products **3** and **4**. For each run, 6 µL of a 100 µM solution in phosphate buffer of H_2cage or photolyzed H_2cage (or 3 µL of 500 µM for the Cu-containing samples and picolinamide) were injected onto the LC/MS. Mass spectra extracted from the ion chromatograms that are associated with these LC traces are shown in Figure 16.

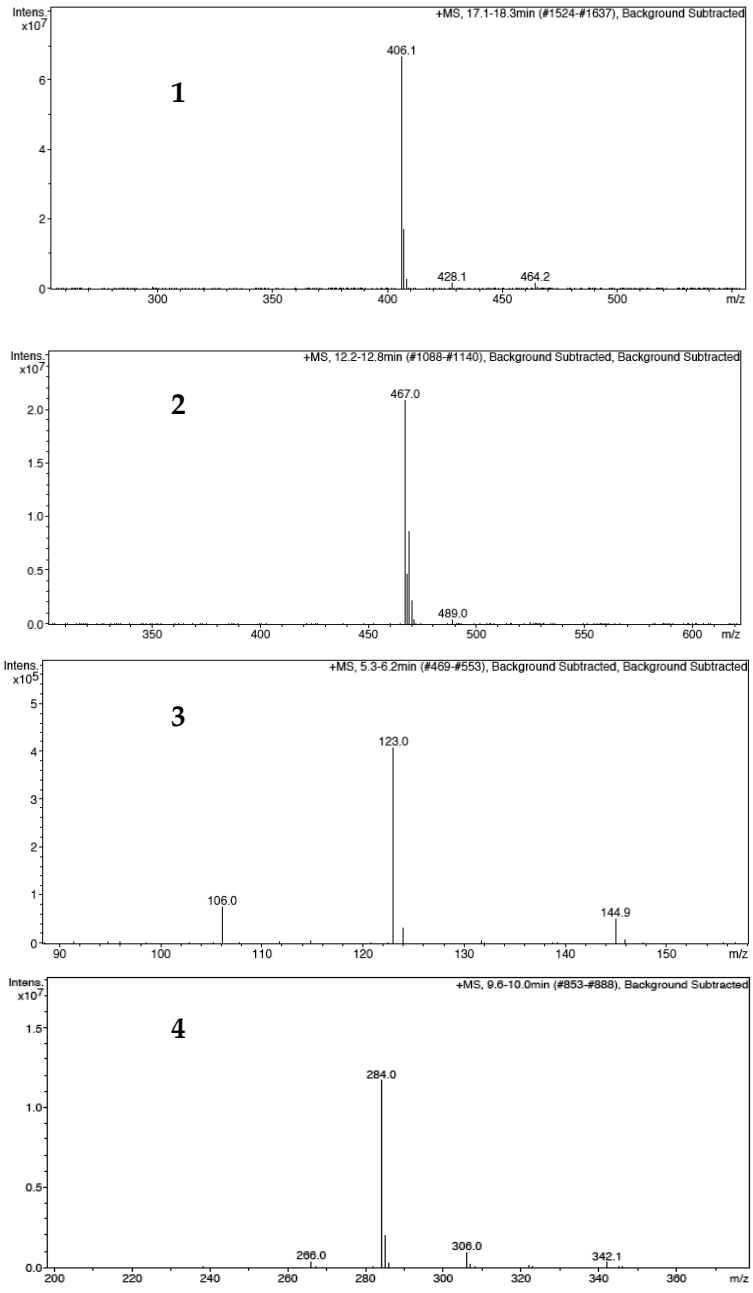

Figure 16: Mass Spectra for the Photolysis of H_2cage and [Cu(OH_2)(cage)]

Positive-mode mass spectra extracted from the ion chromatograms associated with the LC traces in Figure 15. Primary ion values of m/z are calculated in all cases for m = ($M+H^+$) and z = 1. **1** is H_2cage eluting ~ 18 min, calcd: 406.15, found: 406.1; **2** corresponds to [Cu(cage)] eluting ~ 12 min, calcd: 467.12, found: 467.0; **3** is picolinamide ~ 5 min, calcd: 123.06, found: 123.0; and **4** is the nitroso-containing photoproduct that elutes ~ 10 min, calcd 284.11, found: 284.0.

2.3.4 Quantum Yield

Comparison of the LC integrated peak areas indicated that after 15 s of UV exposure, 31.8% of the caged P_i, 20.0% of H_2cage, and 11.5% of [Cu(OH_2)(cage)] had been photolyzed. The calculated quantum yields of photolysis for H_2cage and [Cu(OH_2)(cage)] are 0.73 and 0.32, respectively, which indicates that coordination of the ligand to Cu^{2+} decreases photolysis efficiency but does not prevent it.

2.3.5 Effects of [Cu(OH_2)(cage)] in the Deoxyribose Assay

In order to show that photolysis of [Cu(OH_2)(cage)] causes a change in the reactivity of the caged vs. uncaged copper, we monitored the ability of the compounds pre- and post- photolysis to generate $OH^{\bullet}$ radicals by subjecting them to the deoxyribose assay. Hydroxyl radicals, which are generated in this assay by Fenton-like conditions of copper, ascorbic acid, and H_2O_2, degrade deoxyribose to give thiobarbituric acid (TBA)-reactive products with absorbance at 532 nm. Values of A/A_o above 1 indicate the promotion of $OH^{\bullet}$ formation, whereas values below 1 indicate an inhibition of $OH^{\bullet}$ formation.

In order to show that ligands added to the reaction mixture effect the amount of TBA-reactive species by altering the coordination environment around copper, we tested [Cu(OH_2)(cage)] both pre- and post- photolysis, Cu^{2+} combined with one and two equivalents of picolinamide and Cu^{2+} combined with one equivalent of NTA (Figure 17). As expected, [Cu(OH_2)(cage)] has an inhibitatory effect on $OH^{\bullet}$ formation, as shown by

an A/A_o value less than 1. The photo-products, on the other hand, increase the amount of $OH^{\bullet}$ produced. The reactivity of the photo-products matches that of control reactions run with 1 or 2 equivalents of picolinamide. NTA, which has a similar affinity for Cu^{2+} as H_2cage at this pH, also promotes $OH^{\bullet}$ formation by copper (Figure 17).

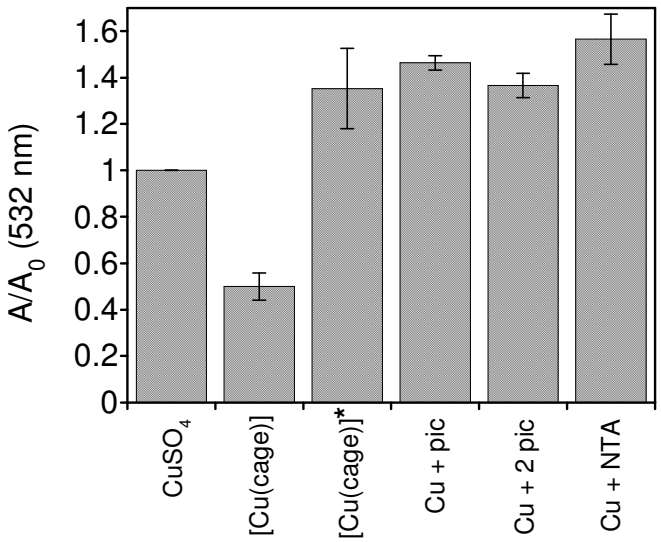

Figure 17: Deoxyribose Assay for [Cu(cage)]

Uncaging copper from [Cu(cage)] in pH 7.4 phosphate buffer by UV photolysis increases $OH^{\bullet}$ production as measured by the increase in A_{532} for deoxyribose degradation. A and A_0 are the absorbance with and without ligand, so $A/A_0 = 1$ for $CuSO_4$ alone; lower values indicate an inhibitory effect and higher values indicate a promotional effect of the ligand with respect to copper's reactivity for $OH^{\bullet}$ production. [Cu(cage)]* was photolyzed for 4 min.

2.4 Discussion

2.4.1 Stability of [Cu(OH_2)(cage)]

Potentiometric titration of H_2cage shows that it contains no dissociable protons between pH 2 and 12, as expected since pK_a values of similarly substituted pyridines are below 2 and those of amide NH are above 12. In the presence of Cu^{2+}, however, protons are released from H_2cage at pH 3.3 and 4.8, consistent with deprotonation of both amides (Figure 9). Analysis of the pH-dependent spectrophotometric titration of a 1:1 mixture of H_2cage and Cu^{2+} shows that the predominant species in solution from pH 5–12 is the neutral compound [Cu(OH_2)(cage)] (Figures 10-11), with an overall stability constant of $\log \beta = 10.8$. This value converts to a conditional dissociation constant, K_d, at pH 7.4 for [Cu(OH_2)(cage)] of 16 pM, which was further confirmed by a competition reaction between H_2cage and the common chelator nitrilotriacetic acid (NTA), which has a K_d of 23 pM for Cu^{2+} at this pH (Figure 12). The 16 pM affinity of our first-generation caged copper, while significant, may not be strong enough to keep copper sequestered in the presence of endogenous copper-binding proteins; for example, human serum albumin binds Cu^{2+} with 1 pM affinity at pH 7.4.

2.4.2 Crystal Structure of [Cu(OH_2)(cage)]

Figure 13 shows that Cu^{2+} is coordinated to H_2cage through 2 deprotonated amide nitrogens and 2 pyridyl nitrogens in a distorted trigonal bipyramidal geometry, with a water molecule lying in the trigonal plane. The cause for this distortion in the trigonal

bipyramidal geometry is due to a steric interaction between the α protons on C1 and C15 of the pyridyl rings (Figure 13).

2.4.3 Efficiency of Photolysis

Figure 14 shows that within seconds of UV exposure the coordination environment around caged copper changes. After 4 minutes cleavage of the ligand is complete, as confirmed by LC-MS analysis shown in Figure 15 and 16. Although, the quantum yield of photolysis decreases from 0.73 for H_2cage to 0.32 for [Cu(OH_2)(cage)], indicating that coordination by Cu^{2+} decreases photolysis efficiency, it does not prevent it. In contrast, binding of Ca^{2+} in caged calcium complexes like NP-EGTA does not significantly alter the quantum yield of photolysis. The quantum yield for H_2cage is similar to other caged compounds that release amide groups upon photolysis.[101,102]

2.4.4 Hydroxyl Radical Formation

The *in vitro* deoxyribose assay was used in order to show that photolysis of [Cu(OH_2)(cage)] causes a change in the reactivity of caged vs. uncaged Cu^{2+} for promoting $OH^{\bullet}$ formation. Ligands added to the reaction mixture effect the formation of the chromophore by altering the coordination environment around copper. As shown in Figure 17, our caging ligand, H_2cage, provides 50% protection of deoxyribose degradation compared to the background reaction of Cu^{2+} alone. On the other hand, the ability of copper to undergo Fenton-like reactivity and promote $OH^{\bullet}$ formation increases

by 160% following light-induced uncaging.

The reactivity of the photo-products matches that of control reactions run with 1 and 2 equivalents of picolinamide, indicating that these bidentate ligands improve the catalytic properties of the metal with respect to Fenton-like chemistry. NTA, which has a similar affinity for Cu^{2+} as H_2cage at this pH, also promotes $OH^{\bullet}$ production by copper (Figure 17). This result highlights the fact that thermodynamic stability of a metal complex is not the fundamental factor dictating Fenton reactivity. Stability, redox potential, and the availability of reactive coordination sites all combine to modulate the reactivity of the metal center for oxidative reactions.

2.5 Summary and Conclusions

In conclusion, we have presented a new photo-active ligand that can cage copper in a tetracoordinate binding site. Activation with UV light uncages the metal cargo by cleaving the ligand backbone to release photoproducts with diminished affinity for Cu^{2+}. The ability of copper to undergo Fenton-like reactivity and promote $OH^{\bullet}$ formation increases following light-induced uncaging. This is a promising step in developing compounds that are triggered by light to increase oxidative stress. The caged copper is a neutral compound with a molecular weight under 500, which may be favorable for cellular permeability. The stability of our first-generation caged copper, while significant, is likely too low to keep copper sequestered in cellular environments. Future work in this dissertation is focused on improving the stability of caged copper complexes, as well as applying photoactive ligands to other metals. These new reagents will be valuable tools for on-demand delivery of metal ions to study mechanisms of metal ion trafficking, as well as applications such as chemotherapy where toxic metal ions could be released to induce cell death.

3. A Caged Platinum(II) Complex that Increases Cytotoxicity upon Light Activation[1]

3.1 Background and Significance

Since the initial discovery of cisplatin's cytotoxicity by Rosenberg in the 1960s, platinum-based drugs, which now include carboplatin and oxaliplatin as well as cisplatin, have become a cornerstone of modern anticancer chemotherapy regimens.[103] The clinical effectiveness of these agents, unfortunately, is restricted by dose-limiting toxicity and intrinsic or acquired resistance of some tumors. Significant efforts to understand the cellular response and tumor resistance mechanisms of platinum drugs[104,105] have inspired the development of new compounds to overcome these limitations. Strategies include altering the coordinating ligands on platinum, designing drug delivery systems that distribute platinum compounds selectively to tumor cells, and developing prodrugs that release cytotoxic agents following an activation step.[106,107] In this area, substitution-inert Pt^{IV} agents that are reduced intracellularly to active Pt^{II} compounds are attractive for diminishing off-target cytotoxicity and resistance.[107] More recently, Sadler and coworkers introduced photoactive Pt^{IV} prodrugs in which the reduction occurs only upon illumination with UV light.[64,108,109]

---

[1] Reproduced in part with permission from Ciesienski, K. L.; Hyman, L. M.; Yang, D. T.; Haas, K. L.; Dickens, M. G.; Holbrook, R. J. and Franz, K. J. *Eur. J. Inorg. Chem.* **2010**, In Press DOI: 10.1002/ejic.201000098. Copyright 2010 Wiley-VCH Verlag GmbH & Co. KGaA, Weinheim.

Photoactive compounds that can deliver cytotoxic drugs intracellularly only at the irradiated site can potentially increase the specificity of a drug and thereby minimize its toxicity to surrounding healthy tissue.[55,110] Such a strategy is envisioned for surface-associated diseases or for internal tissue accessible via endoscopic fiber optic technology.[55] A drawback of the Pt^{IV} complexes reported to date is their sluggish photoactivation, which can take upwards of an hour of UV irradiation.

As an alternative to photoactive Pt^{IV} compounds, we present here a novel photo-caged Pt^{II} complex in which a photoactive nitrophenyl group is incorporated into the ligand backbone. The tetradentate chelating ligand suppresses ligand-exchange reactions to provide a nontoxic Pt^{II} complex, [Pt(cage)]. Activation with light induces bond cleavage of the ligand, as shown in Scheme 12, which converts neutral [Pt(cage)] into a charged and exchange labile Pt^{II} complex (**3**). Both properties may be beneficial for cellular retention of the photolyzed compound. Importantly, photoactivation occurs within minutes and induces significant photo-dependent cytotoxicity.

Photoactive nitrophenyl groups have been used in countless examples to block (i.e. "cage") the biological activity of a variety of molecules such that exposure to UV light turns on a biological function.[111,112] This strategy is also being explored to develop complexes that allow photoinitiated drug release for applications in photochemotherapy.[110,113-116] The concept of light-activated caged metal ions was first introduced for Ca^{2+},[15] and has only recently been expanded to biologically important d-block metal ions like Cu^{2+} and Zn^{2+}.[35,36,117] Metal complexes themselves have also been

exploited as caging groups, for example ruthenium polypyridines that release bioactive compounds by light-induced ligand dissociation.[75,118] In these contexts, the terminology "cage" refers to photocage, where light is used to effect a molecular change that alters a biological response. It does not imply a geometric configuration and is in fact distinct from the classical inorganic definition of cage, which refers to a polycyclic compound having the shape of a cage, or an inclusion compound. The report here demonstrates that a photoactive ligand can be used to unleash the cytotoxicity of a metal-based agent.

Scheme 12: [Pt(cage)] Synthesis and Photolysis

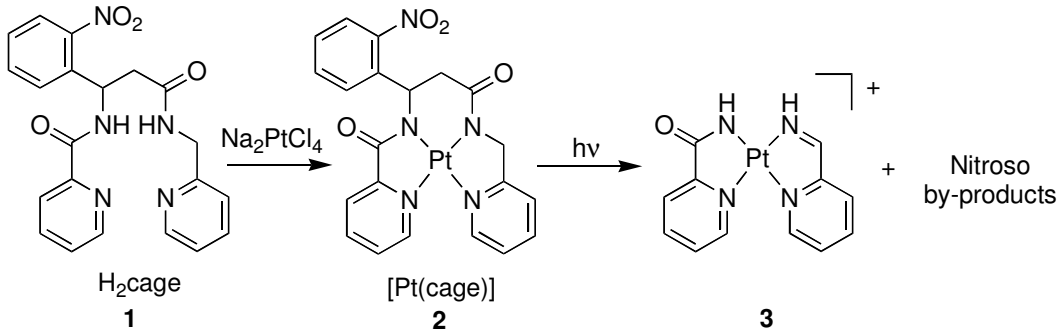

3.2 Materials and Methods

3.2.1 Materials and Instrumentation

Unless otherwise noted, chemicals were purchased commercially and used without further purification. The ligand H_2cage was synthesized and purified as described previously.[26] The peptide AcMMMMPMTFK, which contains an N-terminal acetyl cap and a C-terminal amide, was prepared by standard solid-phase peptide synthesis as reported.[119] Spectra for ^{1}H NMR were collected on a Varian Inova 400 spectrometer with chemical shifts reported in ppm and J values in Hz. Elemental analysis was performed by Columbia Analytical Services, Inc. Liquid chromatography/mass spectrometry (LC/MS) was performed using an Agilent 1100 Series apparatus with an LC/MSD trap and a Daly conversion dynode detector. A Varian Polaris C18 (150 × 1.0 mm) column was used and peaks were detected by UV absorption at 256 nm. High-resolution, fast-atom bombardment (HR-FABMS) mass spectra were recorded on JEOL JMS-SX-102 instrument. All photolysis experiments were conducted by using a Rayonet RPR-100 Photochemical Reactor containing 16 bulbs (14 watts each), with a maximum intensity output centered at 350 nm. To determine the source intensity of the photochemical reactor, chemical actinometry was carried out using potassium ferrioxalate as a standard.[120] The photon flux (source intensity) was determined to be 1.3×10^{18} quanta s^{-1} L^{-1}, which corresponds to 1.17×10^{-4} watts/cm^2 or 6.48×10^{-9} einsteins/s.

3.2.2 Synthesis

3.2.2.1 [Pt(cage)]

A 50 mM aqueous solution of NaOH (9.38 mL) was added dropwise to a refluxing solution of H_2cage (0.095 g, 0.234 mmol) and $Na_2PtCl_4 \bullet xH_2O$ (0.090 g, 0.234 mmol) in 25 mL of EtOH. After refluxing for 18 h, the solvent was removed and the residue was taken up in acetone and filtered. The resulting solution was purified by preparative reverse-phase HPLC on a YMC C18 column (250 × 200 mm I.D.) with a linear 40-min gradient from 7–70% acetonitrile in water. The final yellow solid was obtained in 63 % yield (0.088 g) . ^{1}H NMR (500 MHz, CD_3OD) δ 8.89 (dd, *J* = 20.0, *J* = 5.5, 2H), 8.37 (dd, *J* = 8.0, *J* =1.2, 1H), 8.18 (t, *J* = 7.3, 1H), 8.08 (t, *J* = 7.4, 1H), 7.90 – 7.83 (m, 1H), 7.80 – 7.73 (m, 1H), 7.69 (t, *J* = 6.4, 2H), 7.53 – 7.46 (m, 2H), 7.39 – 7.29 (m, 1H), 5.79 (dd, J = 4.9, *J* = 3.2, 1H), 5.05 (d, *J* = 19.1, 1H), 4.65 (d, *J* = 19.1, 1H), 3.12 (dd, *J* = 14.7, *J* = 4.7, 1H), 2.77 (dd, *J* = 14.7, *J* = 3.2, 1H). HR-FAB: m/z 599.0760 $[M+H]^+$ for [^{195}Pt(cage)]; UV-vis (10 mM aqueous NaH_2PO_4, pH 7.4), 343 nm (4981 $M^{-1}cm^{-1}$); Anal. calcd. for $C_{21}H_{17}PtN_5O_4 \bullet 5H_2O$: C, 36.63; H, 3.95; N, 10.17; found: C, 36.0; H, 3.9; N, 10.0 %.

3.2.3 X-Ray Data Collection and Structure Solution Refinement

Marina Dickens, a graduate student in the Franz laboratory, collected and analyzed the data for all crystal structures. Yellow-orange prisms of [Pt(cage)] were grown by slow evaporation of acetone:H_2O (1:1). The crystal was mounted on a Hampton

Research Mounted CryoLoop with paratone oil. Data were collected at 296 K on a Bruker Kappa Apex II CCD diffractometer equipped with a graphite monochromator and a Mo Kα fine-focus sealed tube (λ= 0.71073Å) operated at 1.75 kW power (50 kV, 35 mA). The detector was placed at a distance of 5.010 cm from the crystal. A total of 2655 frames were collected with a scan width of 0.5º and an exposure time of 5.0 s/frame. The frames were integrated with the Bruker SAINT v7.12A software package using a narrow-frame integration algorithm. Empirical absorption corrections were applied using SADABS v2.10 and the structure was checked for higher symmetry with PLATON v1.07. The structure was solved by direct methods with refinement by full-matrix least-squares based on F^2 using the Bruker SHELXTL Software Package. All non-hydrogen atoms were refined anisotropically. Hydrogen atoms of sp^2 hybridized carbons and nitrogens were located directly from the difference Fourier maps; all others were calculated.

3.2.4 Characterization of Photoproducts

Solutions of [Pt(cage)] were prepared in a minimum amount of DMSO and diluted into 10 mM phosphate buffer, pH 7.4, such that the final DMSO concentration is less than 0.25%. Photoproducts were obtained by photolyzing solutions of [Pt(cage)] for 2 min. All photolysis experiments were performed in a screwtop quartz cuvette illuminated in the Rayonet photoreactor.

3.2.5 Quantum Yield

The quantum yield of photolysis for [Pt(cage)] was determined by comparison to the quantum yield of 1-(o-nitrophenyl)ethyl phosphate (caged Pi) as initially reported by Ellis-Davis and Kaplan.[99] Samples of [Pt(cage)] (100 μM) or caged Pi (1 mM) in 20 mM NaH_2PO_4 buffer pH 7.4 were irradiated in a Rayonet RPR-100 Photochemical Reactor at 350 nm for 15 s. Photodegradation of caged compounds was monitored by LC-MS analysis. Aliquots of 6.0 μL of each sample before and after photolysis were injected by autoinjector and run in triplicate. The experiment was repeated to ensure reproducibility. The quantum yield for the sample (Φ_{sample}) was calculated by using the following equation (Equation 4):

$$\Phi_{sample} = \Phi_{cp} \times \frac{\%\Delta sample}{\%\Delta cp} \times \frac{A_{350}cp}{A_{350}sample} \quad (4)$$

where Φ_{cp} is 0.54, the reported quantum yield of photolysis for caged Pi, %Δsample and %Δcp are the percent change in integrated peak area after photolysis for the sample and caged Pi, respectively, and A_{350} is the absorbance at 350 nm in a 1-mm cuvette for caged Pi (cp) and for the sample.

An alternate method for calculating quantum efficiency is outlined below. The quantum efficiency for each sample (QE) was calculated using the following equation (Equation 5):

$$QE = \frac{\Delta[Pt(cage)] \times N_A}{\text{irradiation time} \times \text{source intensity}} \quad (5)$$

where N_A is Avogadro's number. The change in [Pt(cage)] concentration, Δ [Pt(cage)], was determined by monitoring changes in absorbance spectra at 320 nm. Samples of [Pt(cage)] in 10 mM NaH_2PO_4 buffer pH 7.4 in a 1-cm pathlength quartz cuvette were irradiated in a Rayonet RPR-100 Photochemical Reactor. Photodegradation of [Pt(cage)] was monitored by UV-vis analysis. Samples were photolyzed in 10 s intervals and monitored until no further changes in the absorbance were observed. The concentration of [Pt(cage)] at each time point was determined by solving the following equation (Equation 6) for c_{Ptcage}:

$$A_{total} = \varepsilon_{Ptcage} \times c_{Ptcage} + \varepsilon_{Photoproducts} \times (c_{initial} - c_{Ptcage}) \quad (6)$$

where A_{total} is the absorbance at 320 nm, ε_{Ptcage} is 4561.7 $M^{-1}cm^{-1}$, $\varepsilon_{Photoproducts}$ is 6677.4 $M^{-1}cm^{-1}$ and c_{inital} is the initial concentration of [Pt(cage)] before irradiation. The value for $\varepsilon_{Photoproducts}$ was determined from a completely photolyzed sample. The calculated quantum efficiency of photolysis for [Pt(cage)] was determined to be 0.42.

The calculated quantum efficiency using this method does not match the value obtained using the method developed by Ellis-Davis and Kaplan. The source of error is the assumption that only the nitroso photoproduct has an absorbance at 320 nm without considering the other compounds in solution. Therefore, the correct value is 0.75 and the Ellis-Davis and Kaplan method will be used from here on out.

3.2.6 Cell Culture

Lynne Hyman, a graduate student in the Franz laboratory, performed all cell culture experiments. All cell culture reagents, including minimal essential medium (MEM), Dulbecco's modified eagle medium (DMEM), fetal bovine serum (FBS) and trypsin-EDTA (0.25%) were purchased from Gibco. LDH Release Assay Kit was obtained from Roche Diagnostics and assays were performed on a Perkin Elmer Victor^3 1420 plate reader. MCF-7 cells were graciously obtained from Dr. Mark Dewhirst's lab (Duke University) and were cultured in complete medium containing DMEM supplemented with 10% (v/v) FBS. Cells were incubated at 37°C with a fully humidified atmosphere containing 5% CO_2.

3.2.7 Cytotoxicity Assay

Lynne Hyman, a graduate student in the Franz laboratory, performed the cytotoxicity assay described below. For each experiment, cells were seeded at a density of 80,000 cells per well into a flat bottom 96-well plate and incubated overnight. The growth medium was carefully removed and the cells were washed once with phosphate buffered saline (PBS). 200 μL solutions of cisplatin (dissolved in MEM) and [Pt(cage)] (dissolved in MEM with no more than 0.1% DMSO) at various drug concentrations were added to the wells and incubated for 48, 72, and 96 h. Control wells containing the corresponding amount of DMSO as compared to the [Pt(cage)] wells were also prepared and assayed. For samples exposed to UV light, the entire plate was placed in the Rayonet

photoreactor for 2 min, then placed back in the incubator and left in the dark for 48, 72, and 96 h. At the end of the incubation time, 100 μL aliquots of the medium were removed, fractionated by centrifugation (1200 rpm for 10 min), and 70 μL of the solution was placed in a 96-well plate. A 30-μL portion of PBS was added to each well, followed by freshly prepared LDH reaction mixture (100 μL). After 30 min of incubation at room temperature in the dark, the absorbance of each solution at 490 nm was measured on a plate reader. The percentage of cell death was calculated using the formula in Equation 7:

$$\% \text{ Cytotoxicity} = \frac{\text{experimental value} - \text{low control}}{\text{high control} - \text{low control}} \times 100 \qquad (7)$$

where the low control is the average absorbance of triplicate wells containing MEM only and the high control is the average absorbance of triplicate wells containing 1% Triton X-100 in MEM. All conditions were tested in at least triplicate with results presented as the mean value ± standard deviation.

3.2.8 DNA Gels

Kathryn Haas, a graduate student in the Franz laboratory, loaded and ran all DNA gels. Samples of pUC18 DNA (100 ng, either circular or linearized with EcoR1 restriction enzyme then gel purified) were incubated with 0–300 μM samples of [Pt(Cage)] (and samples of [Pt(Cage)] that had been photolyzed for 2 min prior to DNA

incubation) at 37°C for 24–96 hours. After incubation, samples were loaded with 5× DNA loading buffer onto a 1% agarose gel in 1X TBE and run at 30V for 16–30 h. Gels were stained with ethidium bromide and visualized using a gel doc system (BioRad).

3.2.9 Reactions of [Pt(cage)] with AcMMMMPMTFK

Portions of [Pt(cage)] (0.5 mM, before and after photolysis) and AcMMMMPMTFK (1.0 mM) were combined in 10 mM pH 7.4 phosphate buffer:DMSO (9:1). Solutions were incubated at 37°C and aliquots were removed after 24 h for analysis by LC/MS. A linear gradient from 10% A in B to 60% A in B was run from 2 to 37 min, where A is MeCN / 4% 10 mM ammonium acetate buffer and B is 10 mM ammonium acetate buffer / 2% MeCN. Aliquots of 6.0 μL of each sample were injected by autoinjector and run in triplicate. The experiment was repeated to ensure reproducibility.

3.3 Results

3.3.1 Crystal Structure of [Pt(cage)]

[Pt(cage)] was prepared in one step by combining equimolar quantities of H_2cage[117] and Na_2PtCl_4 in basic ethanol. Recrystallization from acetone/H_2O permitted analysis by X-ray crystallography that confirmed that two deprotonated amide nitrogens and two pyridyl nitrogens coordinate the Pt^{II} center in square planar geometry. Figure 18 shows the fully labeled structure with select bond distances and angles. Table 5 contains a summary of crystal data, intensity collection and structure refinement parameters. Bond lengths and angles are listed in Table 6.

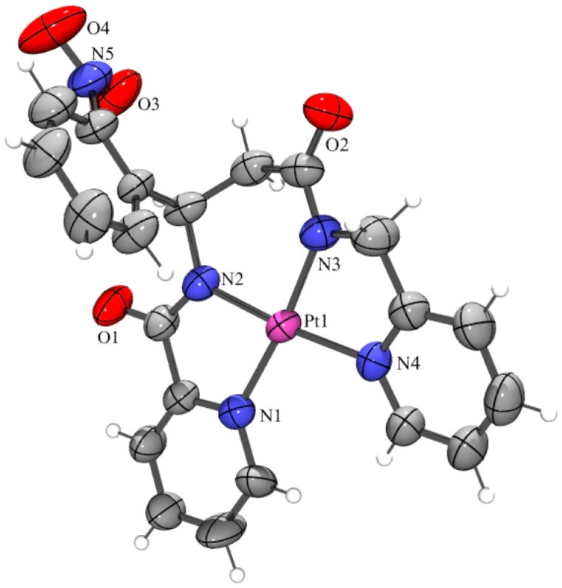

Figure 18: ORTEP Diagram of [Pt(cage)]

ORTEP plot of [Pt(cage)] showing 50% thermal ellipsoids. Selected bond distances and angles: Pt–N1, 2.036(6); Pt–N2, 1.979(6); Pt–N3, 1.994(7); Pt–N4, 2.036(6) Å; N2–Pt–N3, 93.7(3); N2–Pt–N1, 79.8(3); N3–Pt–N1, 173.4(3); N2–Pt–N4, 173.7(3); N3–Pt–N4, 80.2(3); N1–Pt–N4, 106.4(3)°.

Table 5: Crystal Data and Structure Refinement for [Pt(cage)]

Identification code	md57a	
Empirical formula	$C_{21}H_{17}N_5O_4Pt$	
Formula weight	598.49	
Temperature	296(2) K	
Wavelength	0.71073 Å	
Crystal system	Monoclinic	
Space group	C2/c	
Unit cell dimensions	a = 28.696(2) Å	α= 90°
	b = 9.8361(7) Å	β= 114.0590(10)°
	c = 16.3573(12) Å	γ = 90°
Volume	4215.8(5) $Å^3$	
Z	8	
Density (calculated)	1.886 Mg/m^3	
Absorption coefficient	6.695 mm^{-1}	
F(000)	2304	
Crystal size	0.48 x 0.11 x 0.09 mm^3	
Crystal color and habit	yellow prism	
Diffractometer	Bruker SMART Apex II	
Theta range for data collection	2.43 to 29.23°.	
Index ranges	-39<=h<=39, -13<=k<=8, -22<=l<=22	
Reflections collected	34063	
Independent reflections	5660 [R(int) = 0.0550]	
Observed reflections (I > 2σ(I))	3872	
Completeness to theta = 29.23°	98.7 %	
Absorption correction	Semi-empirical from equivalents	
Max. and min. transmission	0.5841 and 0.1414	
Solution method	SHELXS-97 (Sheldrick, 1990)	
Refinement method	SHELXL-97 (Sheldrick, 1997)	
Data / restraints / parameters	5660 / 0 / 281	
Goodness-of-fit on F^2	1.138	
Final R indices [I>2σ(I)]	R1 = 0.0485, wR2 = 0.1366	
R indices (all data)	R1 = 0.0788, wR2 = 0.1554	
Largest diff. peak and hole	3.812 and -1.129 $e \cdot Å^{-3}$	

Table 6: Bond Lengths [Å] and Angles [°] for [Pt(cage)]

Pt(1)-N(2)	1.979(6)	C(10)-H(10B)	0.9700
Pt(1)-N(3)	1.994(7)	C(11)-C(12)	1.360(14)
Pt(1)-N(1)	2.036(6)	C(12)-C(13)	1.396(15)
Pt(1)-N(4)	2.036(6)	C(12)-H(12A)	0.9300
O(1)-C(6)	1.237(10)	C(13)-C(14)	1.367(16)
O(2)-C(9)	1.246(11)	C(13)-H(13A)	0.9300
O(3)-N(5)	1.181(11)	C(14)-C(15)	1.361(12)
O(4)-N(5)	1.172(10)	C(14)-H(14A)	0.9300
N(1)-C(5)	1.340(9)	C(15)-H(15A)	0.9300
N(1)-C(1)	1.386(10)	C(16)-C(21)	1.334(10)
N(2)-C(6)	1.310(10)	C(16)-C(17)	1.382(11)
N(2)-C(7)	1.471(9)	C(17)-C(18)	1.377(14)
N(3)-C(9)	1.301(10)	C(17)-H(17A)	0.9300
N(3)-C(10)	1.437(12)	C(18)-C(19)	1.351(17)
N(4)-C(15)	1.331(10)	C(18)-H(18A)	0.9300
N(4)-C(11)	1.367(10)	C(19)-C(20)	1.357(16)
N(5)-C(21)	1.483(12)	C(19)-H(19A)	0.9300
C(1)-C(2)	1.410(14)	C(20)-C(21)	1.353(13)
C(1)-H(1A)	0.9300	C(20)-H(20A)	0.9300
C(2)-C(3)	1.358(18)	N(2)-Pt(1)-N(3)	93.7(3)
C(2)-H(2A)	0.9300	N(2)-Pt(1)-N(1)	79.8(3)
C(3)-C(4)	1.379(14)	N(3)-Pt(1)-N(1)	173.4(3)
C(3)-H(3A)	0.9300	N(2)-Pt(1)-N(4)	173.7(3)
C(4)-C(5)	1.343(12)	N(3)-Pt(1)-N(4)	80.2(3)
C(4)-H(4A)	0.9300	N(1)-Pt(1)-N(4)	106.4(3)
C(5)-C(6)	1.510(10)	C(5)-N(1)-C(1)	117.4(7)
C(7)-C(8)	1.509(12)	C(5)-N(1)-Pt(1)	114.2(5)
C(7)-C(16)	1.600(11)	C(1)-N(1)-Pt(1)	128.3(6)
C(7)-H(7A)	0.9800	C(6)-N(2)-C(7)	117.2(7)
C(8)-C(9)	1.506(12)	C(6)-N(2)-Pt(1)	118.4(5)
C(8)-H(8A)	0.9700	C(7)-N(2)-Pt(1)	124.3(5)
C(8)-H(8B)	0.9700	C(9)-N(3)-C(10)	117.0(7)
C(10)-C(11)	1.495(13)	C(9)-N(3)-Pt(1)	127.3(6)
C(10)-H(10A)	0.9700	C(10)-N(3)-Pt(1)	115.6(6)
C(15)-N(4)-C(11)	116.5(7)	O(2)-C(9)-N(3)	124.3(9)
C(15)-N(4)-Pt(1)	128.5(6)	O(2)-C(9)-C(8)	117.7(8)
C(11)-N(4)-Pt(1)	115.0(5)	N(3)-C(9)-C(8)	117.8(8)
O(4)-N(5)-O(3)	119.0(10)	N(3)-C(10)-C(11)	110.2(8)
O(4)-N(5)-C(21)	120.8(9)	N(3)-C(10)-H(10A)	109.6
O(3)-N(5)-C(21)	119.9(8)	C(11)-C(10)-H(10A)	109.6
N(1)-C(1)-C(2)	119.8(9)	N(3)-C(10)-H(10B)	109.6
N(1)-C(1)-H(1A)	120.1	C(11)-C(10)-H(10B)	109.6

Table 6 continued.

C(2)-C(1)-H(1A)	120.1	H(10A)-C(10)-H(10B)	108.1
C(3)-C(2)-C(1)	120.4(10)	C(12)-C(11)-N(4)	122.4(9)
C(3)-C(2)-H(2A)	119.8	C(12)-C(11)-C(10)	121.8(9)
C(1)-C(2)-H(2A)	119.8	N(4)-C(11)-C(10)	115.7(8)
C(2)-C(3)-C(4)	117.8(9)	C(11)-C(12)-C(13)	119.4(10)
C(2)-C(3)-H(3A)	121.1	C(11)-C(12)-H(12A)	120.3
C(4)-C(3)-H(3A)	121.1	C(13)-C(12)-H(12A)	120.3
C(5)-C(4)-C(3)	121.1(9)	C(14)-C(13)-C(12)	118.1(9)
C(5)-C(4)-H(4A)	119.4	C(14)-C(13)-H(13A)	121.0
C(3)-C(4)-H(4A)	119.4	C(12)-C(13)-H(13A)	121.0
N(1)-C(5)-C(4)	123.1(7)	C(15)-C(14)-C(13)	119.3(10)
N(1)-C(5)-C(6)	114.6(7)	C(15)-C(14)-H(14A)	120.4
C(4)-C(5)-C(6)	122.3(7)	C(13)-C(14)-H(14A)	120.4
O(1)-C(6)-N(2)	127.4(8)	N(4)-C(15)-C(14)	124.2(9)
O(1)-C(6)-C(5)	119.8(7)	N(4)-C(15)-H(15A)	117.9
N(2)-C(6)-C(5)	112.8(7)	C(14)-C(15)-H(15A)	117.9
N(2)-C(7)-C(8)	109.6(7)	C(21)-C(16)-C(17)	118.7(8)
N(2)-C(7)-C(16)	110.6(6)	C(21)-C(16)-C(7)	124.8(7)
C(8)-C(7)-C(16)	111.1(7)	C(17)-C(16)-C(7)	116.5(7)
N(2)-C(7)-H(7A)	108.5	C(18)-C(17)-C(16)	119.6(9)
C(8)-C(7)-H(7A)	108.5	C(18)-C(17)-H(17A)	120.2
C(16)-C(7)-H(7A)	108.5	C(16)-C(17)-H(17A)	120.2
C(9)-C(8)-C(7)	118.9(7)	C(19)-C(18)-C(17)	120.0(11)
C(9)-C(8)-H(8A)	107.6	C(19)-C(18)-H(18A)	120.0
C(7)-C(8)-H(8A)	107.6	C(17)-C(18)-H(18A)	120.0
C(9)-C(8)-H(8B)	107.6	C(18)-C(19)-C(20)	119.6(10)
C(7)-C(8)-H(8B)	107.6	C(18)-C(19)-H(19A)	120.2
H(8A)-C(8)-H(8B)	107.0	C(20)-C(19)-H(19A)	120.2
C(21)-C(20)-C(19)	120.2(10)	C(16)-C(21)-C(20)	121.7(9)
C(21)-C(20)-H(20A)	119.9	C(16)-C(21)-N(5)	124.5(8)
C(19)-C(20)-H(20A)	119.9	C(20)-C(21)-N(5)	113.6(8)

3.3.2 Photolysis of [Pt(cage)]

To investigate the photoreactivity of [Pt(cage)], solutions of the complex dissolved in pH 7.4 phosphate buffer were irradiated in a Rayonet photoreactor and monitored by UV-Vis spectrophotometry. As shown in Figure 19, spectral changes are apparent within seconds of illumination and exhibit an increase at 320 nm that is characteristic of a nitroso photoproduct. These data suggest that the photoreaction and in turn cleavage of the ligand backbone is complete in approximately 2 min, as confirmed by LC-MS analysis shown in Figure 20 and 21. The peak for intact [Pt(cage)] (**2**) disappears and is replaced by a peak corresponding to photoproduct **3**, as confirmed by their corresponding mass spectra. The reaction solution was also analyzed on a high-resolution electrospray ionization (HR-ESI) mass spectrometer (model: Agilent 6224) to obtain the exact mass and composition of the Pt-containing photoproduct, found to be 422.0593 m/z, which corresponds exclusively to $C_{12}H_{11}ON_4{}^{195}Pt$ (compound **3**) (see Figure 21). Attempts to characterize the remaining fragment(s), which must contain the aromatic nitroso byproduct(s), were unfortunately not successful. As seen in Figure 20, no other discrete peak is observed in the UV chromatogram, indicating that the missing fragment from the reaction likely decomposes or further reacts to produce a mixture of species that are difficult to identify.

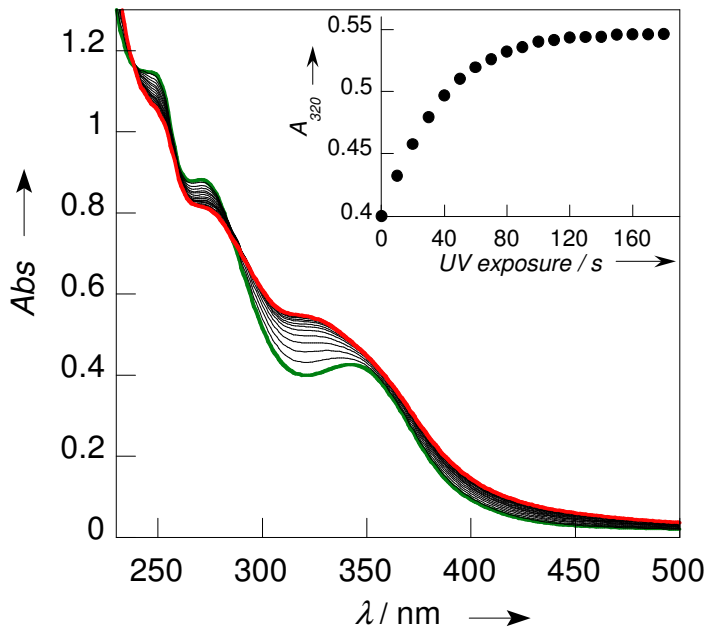

Figure 19: Absorbance Spectra for Photolysis of [Pt(cage)]

UV-vis spectra of 80 μM [Pt(cage)] in phosphate buffer at pH 7.4 photolyzed in 10 s intervals for a total of 180 s (initial spectrum at time zero is green, final spectrum is red); inset: Absorbance at 320 nm vs. irradiation time shows that the compound is completely photolyzed within 2 min.

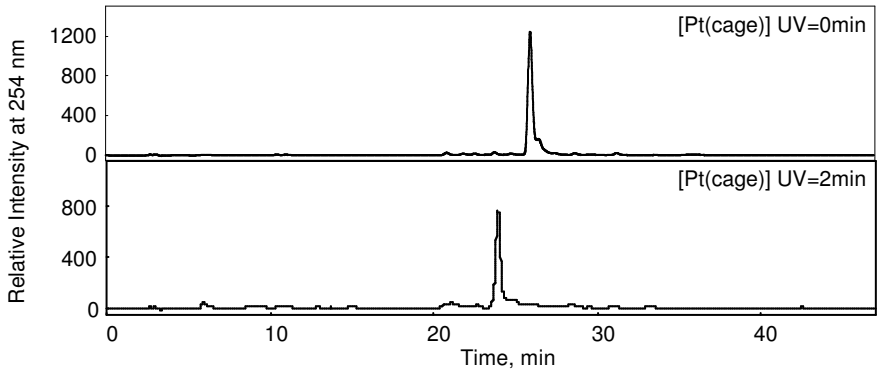

Figure 20: Chromatography Traces for [Pt(cage)] Pre- and Post-Photolysis

Chromatography traces for intact [Pt(cage)] (top) and [Pt(cage)] after 2 min of UV exposure (bottom), showing the complete transformation of starting compound to photolyzed product. Mass spectra corresponding to the LC peaks confirm the identity of [Pt(cage)] (calcd: 599.10, found: 599.1 m/z) and photoproduct **3** (calcd: 422.06, found: 422.1 m/z). Primary ion values of m/z are calculated in all cases for m = $(M+H^+)$ and z = 1.

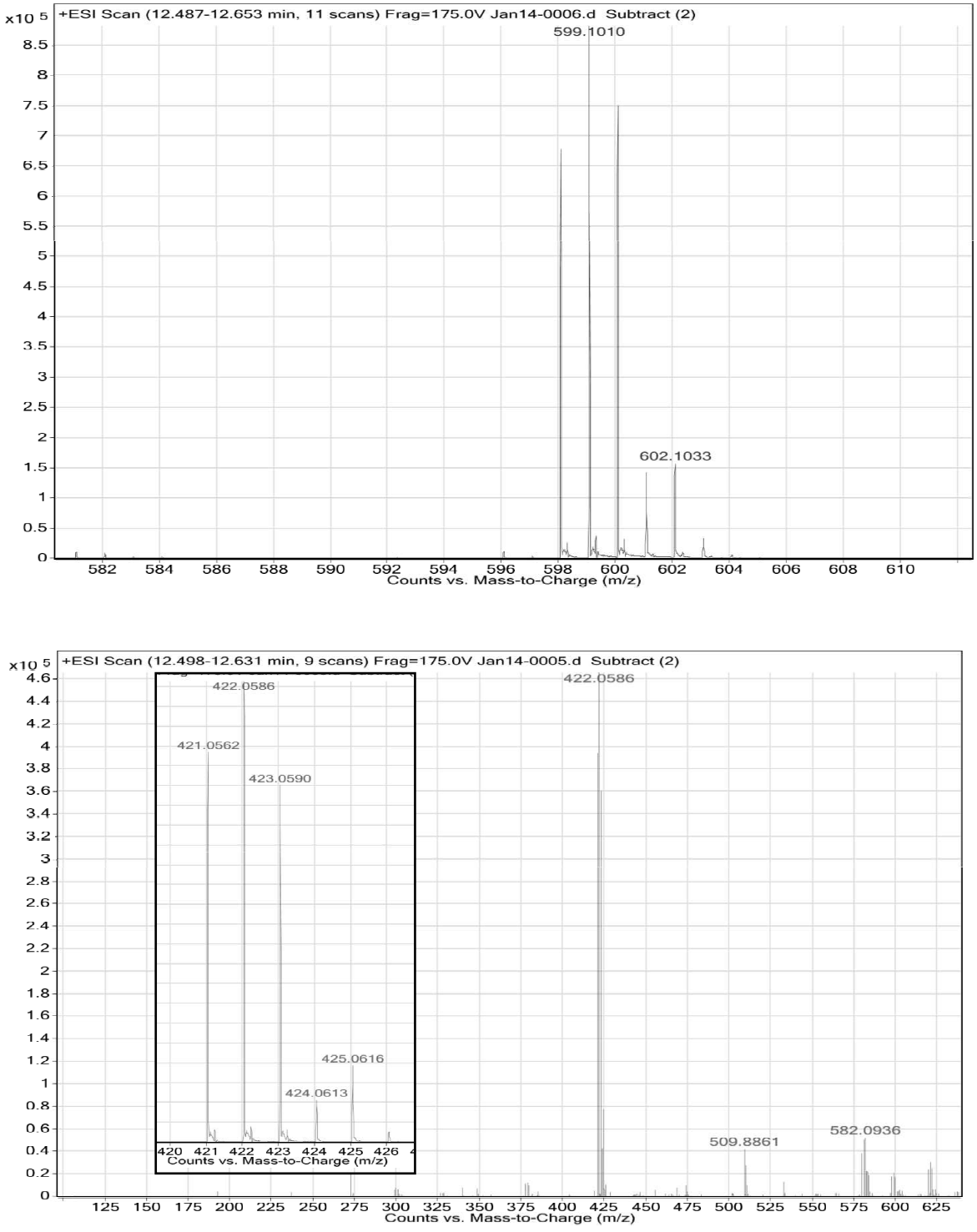

Figure 21: High-Resolution Mass Spectra of [Pt(cage)] Pre- and Post-Photolysis

High-resolution mass spectra of [Pt(cage)] (top) and photoproduct **3** (bottom and inset).

3.3.3 Quantum Yield

Comparison of the integrated peak areas indicated that after 15 s of UV exposure, 45.3% of the caged Pi and 65.4% of [Pt(cage)] had been photolyzed. The calculated quantum yield of photolysis for [Pt(cage)] is 0.75, which indicates that coordination of the ligand to Pt^{2+} does not decrease photolysis efficiency of the caging ligand.

3.3.4 Cytotoxicity Assays

The photolysis experiments described above indicate that two bidentate photoproducts remain coordinated to Pt^{II} following illumination. In order to determine whether such a product could induce cell death, we treated human breast carcinoma MCF-7 cells with [Pt(cage)] and monitored cytotoxicity of irradiated vs. non irradiated samples. For comparison, cells were also treated with cisplatin. As shown in Figure 22, control cells exposed to 2 min of UV light remain viable over the course of 96 h and display no increase in cell death compared to cells kept in the dark. As expected, cisplatin induces cytotoxicity in a dose-dependent manner with concentrations ranging from 50–200 μM. Exposure of cisplatin-treated cells to UV light only subtly increases sensitivity of the cells to cisplatin cytotoxicity. On the other hand, cells treated with up to 200 μM [Pt(cage)] and left in the dark remain viable over the 96 h timecourse, whereas those that are also exposed to 2 min of UV irradiation show a significant increase in cell death. These results suggest that intact [Pt(cage)] itself is non-toxic, but activation with UV-light releases photoproducts that induce cell death in a light-dependent fashion.

Control experiments using H_2cage show that the ligand itself is cytotoxic, even in the dark. As shown in Figure 23, a 200-μM dose of H_2cage causes nearly 60% cell death within 48 h, even in the absence of UV irradiation. Cytotoxicity further increases when the cells also receive 2 min of UV exposure, even at the earliest timepoint monitored in these experiments (48 h). In contrast, cells treated with 200 μM [Pt(cage)] and irradiation remain mostly viable at 48h, showing less than 15% cell death.

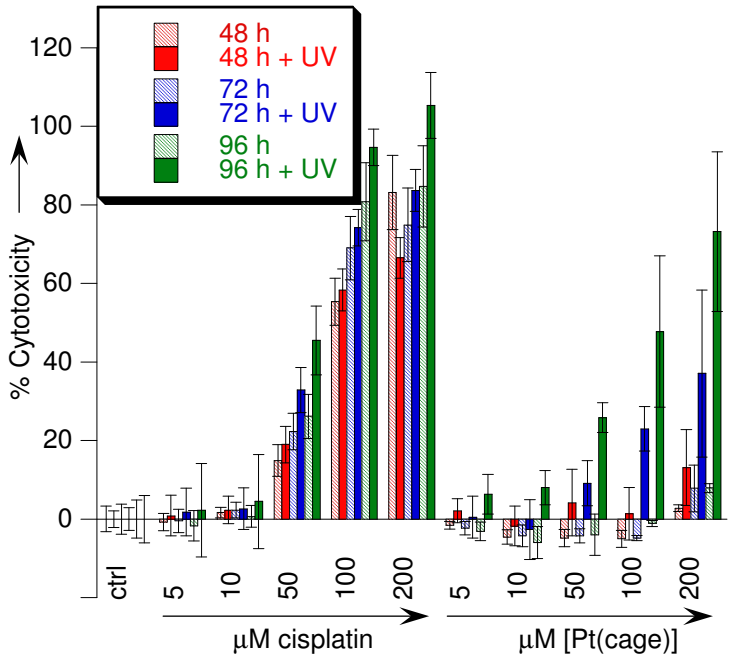

Figure 22: Results of Cytotoxicity Assay of MCF-7 Cells Treated with Cisplatin and [Pt(cage)]

Results of cytotoxicity assay performed on MCF-7, human breast carcinoma cell line. Cells were treated with 5–200 µM cisplatin or [Pt(cage)] and either left in the dark or exposed to UV light for 2 min (+ UV). Cell death was assessed by the LDH release assay after 48, 72, or 96 h, as indicated. Control cells (ctrl) received no drug treatment but were exposed to UV light.

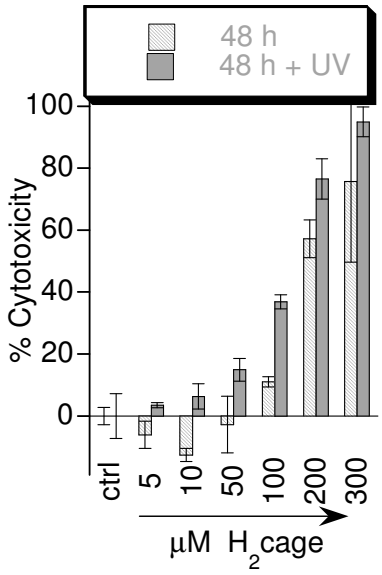

Figure 23: Results of Cytotoxicity Assay of MCF-7 Cells Treated with H_2cage

Results of LDH cytotoxicity assay performed on MCF-7 cells treated with 5–200 µM H_2cage and either left in the dark or exposed to UV light for 2 min prior to 48 h incubation.

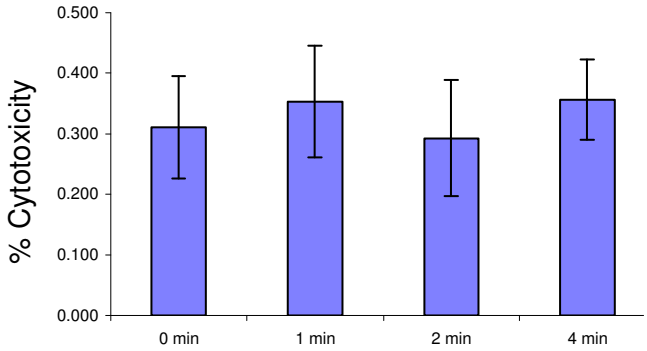

Figure 24: Results of Cytotoxicity Assay of MCF-7 Cells Irradiated with UV light

MCF-7 cells were irradiated with UV light at varying time intervals and then incubated for 24 h prior to assessing cytotoxicity. Results indicate that an equal amount of LDH was released under each condition, suggesting cell viability is maintained, even when cells are irradiated in the Rayonet Photoreactor for 4 min.

3.3.5 DNA Binding

The binding of platinum drugs to DNA is believed to be the primary biological interaction responsible for their anticancer properties.[104] In an attempt to visualize such interactions for [Pt(cage)] or its photoproducts, we used agarose gel electrophoresis. Intact [Pt(cage)] at concentrations up to 300 μM had no effect on the migration of either circular or linear plasmid DNA through the gel, suggesting that the compound does not react with DNA to form platinum adducts, at least under the conditions tested (Figure 25). This result was expected, given the stability of the tetradentate chelator designed to minimize ligand exchange reactions. However, photolyzed samples of [Pt(cage)] also failed to cause a shift in DNA migration (Figure 25).

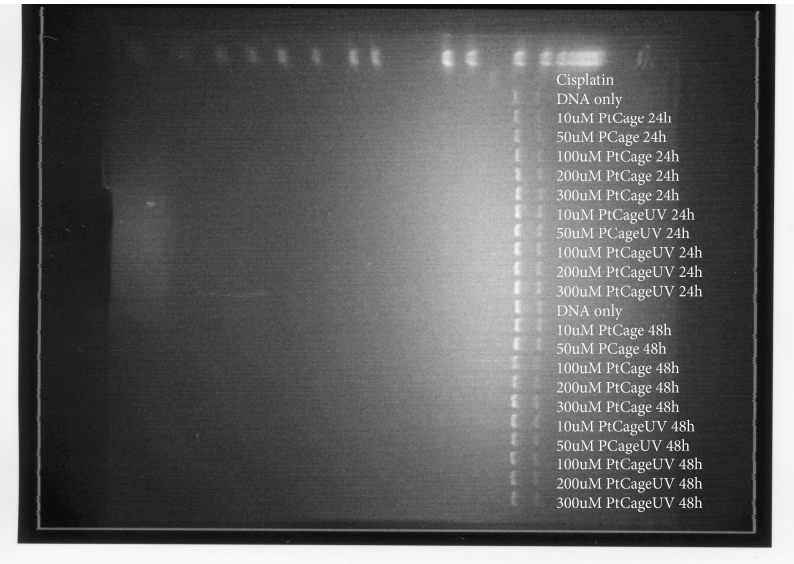

Figure 25: Representative Gel of pUC18 DNA and [Pt(cage)]

Agarose gel of circular plasmid DNA incubated with intact and photolyzed (+UV) samples of [Pt(cage)]. No shift in the DNA bands are observed. In contrast, incubation with cisplatin shows the expected band shift.

3.3.6 Interaction of Ctr-1 Model Peptide with [Pt(cage)]

To show that photolysis of [Pt(cage)] causes a change in its reactivity we monitored the ability of the complex to react with the peptide AcMMMMPMTFK that we have previously shown reacts with cisplatin, carboplatin, and oxaliplatin.[119] As shown by the LC/MS data in Figure 26, intact [Pt(cage)] shows no interaction with AcMMMMPMTFK even after 24 h of incubation at 37 °C. On the other hand, photolyzed samples show a decrease in signal intensity for both **3** (compared to photolyzed [Pt(cage)] samples without peptide) and the peptide (see Figure 27), suggesting that a reaction has occurred. Furthermore, new peaks emerge in the UV chromatogram that indicate a complex mixture of products. While most of these species were not able to be identified, one provided a strong ion peak in the mass spectrum at 1382.5 m/z, which is consistent with formation of $[Pt(AcMMMMPMTFK)]^{+}$. This result further confirms that the intact [Pt(cage)] is inert to ligand substitution, whereas the photoproduct can react with biomolecules and shed the bidentate ligands.

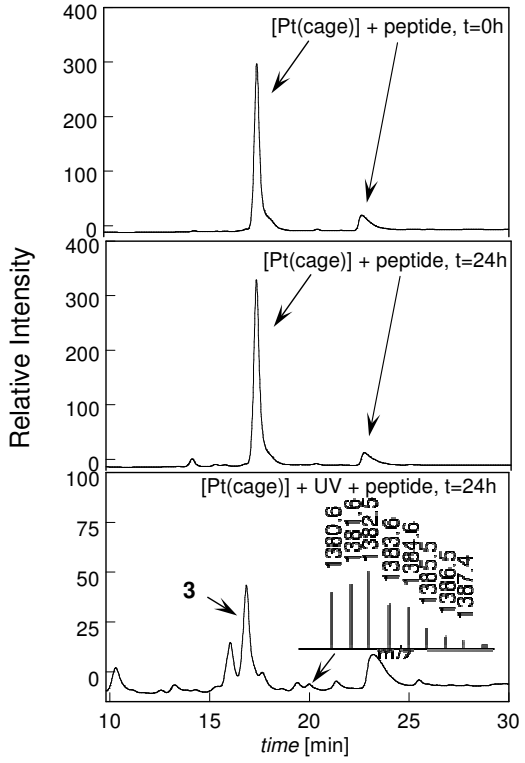

Figure 26: Chromatography Traces for Reaction Mixtures of [Pt(cage)] and Peptide AcMMMMPMTFK

Reaction mixtures were incubated at 37 ^{o}C with or without photolysis. Top: trace recorded just after mixing at time zero. Middle: 24 h sample that was not photolyzed shows no changes. Bottom: The UV trace for photoproduct **3** elutes at the same time as [Pt(cage)], but is identified by its mass spectrum. Inset: a characteristic mass spectrum corresponding to elution time 19–21 min, identified as the expected isotopic mass distribution for a $[Pt(AcMMMMPMTFK)]^{+}$complex. For all traces: the peptide absorbs weakly at 254 nm, so provides a weak intensity signal compared to [Pt(cage)]. See Figure 27 for analysis at 228 nm, where the peptide intensity is greater.

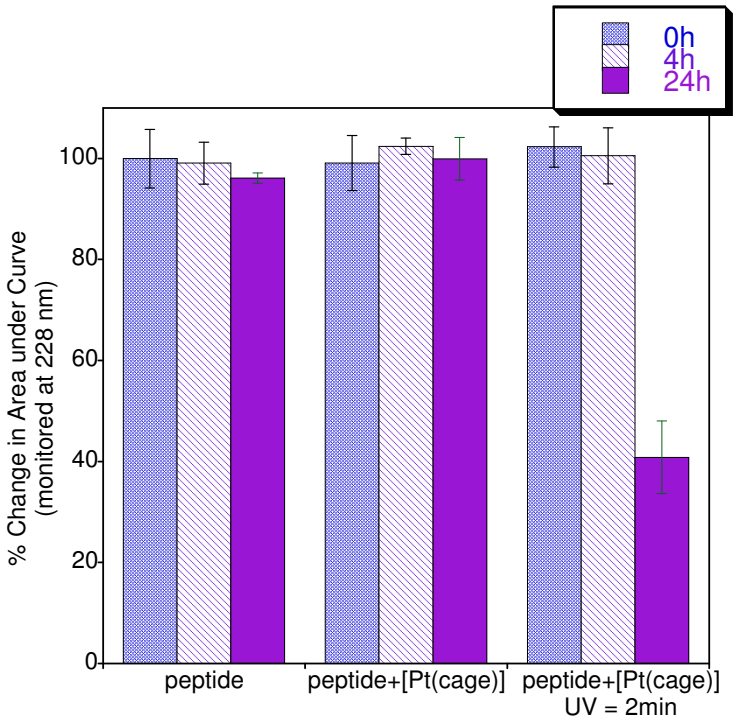

Figure 27: Percent Change in Area under the Curve for Peptide AcMMMMPMTFK at 228 nm over 24 h

Chromatography data corresponding to the experiment shown in Figure 26, but monitored at 228 nm, where the peptide has significant absorbance. The data are plotted as the change in area under the curve for the chromatography peak of the full-length peptide centered at 24 min. This peak loses 60% of its intensity only after incubating with the photolyzed [Pt(cage)] species for 24 h, indicating light-dependent reactivity.

3.4 Discussion

3.4.1 Crystal Structure of [Pt(cage)]

Figure 18 shows that two deprotonated amide nitrogens and two pyridyl nitrogens coordinate the Pt^{II} center in a square planar geometry. In comparison, the copper complex of this ligand, [$Cu(OH_2)$(cage)], has distorted trigonal bipyramidal geometry that can be attributed to a steric interaction between the α hydrogens on the pyridyl rings.[117] The increased radius of Pt^{II} compared to Cu^{II} alleviates this steric clash to accommodate the square planar arrangement preferred by this d^8 metal ion. The average Pt–amide bond distance of 1.987 Å and Pt–pyridyl distance of 2.036 Å are similar to those of [$Cu(OH_2)$(cage)], 1.943 Å and 2.034 Å respectively.

3.4.2 Photolysis of [Pt(cage)]

Analysis of reaction mixtures of [Pt(cage)] post-photolysis by LC-MS revealed **3** as the major product (see Figure 20-21), implying that ligand cleavage occurs at two sites. The products are slightly different from those observed for the apo-ligand or its Cu(II) complex, where the ligand is cleaved only at one position.[117] We hypothesize that upon excitation of the nitrophenyl group, initial bond cleavage occurs to release the picolinamide fragment shown coordinated to Pt in **3** and a nitroso photoproduct that subsequently undergoes a Norrish type II photoreaction to liberate the imine fragment bound to Pt in compound **3** along with nitroso-containing by-products (Scheme 12). The quantum efficiency for the photolysis of [Pt(cage)] was determined to be 0.75. The

ligand itself has a quantum efficiency of 0.73, which indicates that coordination by Pt^{II} does not decrease photolysis efficiency, as previously observed for [Cu(cage)].[117]

3.4.3 Cytotoxicity of [Pt(cage)] and H_2cage in MCF-7 Cells

The combined results shown in Figures 22 and 23 indicate that coordination to Pt^{II} actually mitigates an inherent cytotoxicity of the ligand. Furthermore, the timing discrepancy in light-activated cell killing implies different mechanisms of toxicity for [Pt(cage)] and H_2cage, which photolytically decompose into different organic fragments. The observations that the carrier ligand's toxicity is increased by light-activation but can be masked by metal binding suggests a possible synergy between the metal component and ligand component that could be further exploited to improve light-activated cell killing.

3.4.4 DNA Platination Pre- and Post-Photolysis

The lack of evidence for light-dependent DNA platination requires further investigation in order to understand the biological activity of **3** that induces the cytotoxicity observed in Figure 22. Notably, other tetraamine Pt^{II} complexes have shown cytotoxicity in cancer cell lines.[121]

3.4.5 Interaction of Ctr-1 Model Peptide with [Pt(cage)]

Pt^{II} interactions with sulfur-containing biomolecules are believed to play various roles in the uptake, excretion, resistance and toxicity of platinum drugs.[122] Current Pt-based drugs are thought to enter cells by a combination of passive diffusion and facilitated uptake by transporters that include the sulfur-rich copper transport protein Ctr1. We, and others, have shown that the methionine-rich extracellular regions of Ctr1 are capable of coordinating Pt drugs and, especially in the case of cisplatin, inducing complete loss of the carrier ligands.[119,123,124] Because such interactions are likely to diminish the cytotoxic potential of Pt drugs, we were curious to compare the difference in reactivity of [Pt(cage)] pre- and post-photolysis with a model Ctr1 peptide.

The lack of interaction between the methionine-rich peptide and [Pt(cage)] implies that, prior to photo treatment, [Pt(cage)] is unlikely to enter cells via a Ctr1-mediated pathway or be stripped of its carrier ligand. [Pt(cage)] is a neutral complex with a molecular weight less than 500 g/mol, which may be favorable for passive diffusion into cells. Like cisplatin, the [Pt(cage)] photoproduct (**3**) is a charged complex, which makes it less likely to diffuse through biological membranes and suggests that it could become trapped in the cell to facilitate its cytotoxic effects. This change from a neutral to charged complex may be another beneficial property imparted by the photoactivation of [Pt(cage)] in addition to the tetradentate-to-bidentate conversion.

3.5 Summary and Conclusions

In conclusion, we have presented an inert Pt^{II} compound that upon irradiation with UV light uncages a biologically active Pt^{II} complex by cleavage of the ligand backbone. [Pt(cage)] was shown to be non-toxic to human breast carcinoma MCF-7 cells in the dark, however upon irradiation its cytotoxicity increased by 65% and was similar to that of cisplatin. [Pt(cage)] will be a valuable tool for delivering Pt intracellularly in a site and time specific manner and represents an alternative strategy for activating metal-based drugs with light.

4. Detection of Cellular Copper(II) by Light-Activated Fluorescence Increase[1]

4.1 Background and Significance

Copper, the third most abundant transition metal in the human body, plays a critical role in many fundamental physiological processes; however, it also catalyzes the production of highly reactive oxygen species that damage biomolecules.[125,126] Due to copper's dual nature, cells have developed strict regulatory processes to control its cellular distribution.[125,126] Alterations in copper homeostasis are linked to neurodegenerative diseases such as Menkes and Wilson diseases, Alzheimer's, familial amyotrophic lateral sclerosis, and prion diseases.[90,93,127] Being able to visualize the cellular distribution of copper in both its physiological oxidation states, Cu^{+} and Cu^{2+}, would offer insight into how cells acquire, maintain, and utilize copper while suppressing its toxicity. Whereas reliable fluorescence sensors exist for Cu^{+}, there are fewer options for detecting Cu^{2+} in living cells.[128]

A common strategy in designing fluorescent probes for metal ions is to link a ligand to a fluorophore such that metal binding causes an increase in fluorescence only in response to the target ion. Cell permeable fluorescent sensors have proven useful for investigating intracellular metal ion distribution, particularly for Ca^{2+}, [28] Zn^{2+} ,[29,30,129] and Cu^{+}.[31,32,130] The development of this type of "turn-on" sensor for Cu^{2+}, however, is

---

[1] Reproduced in part with permission from Ciesienski, K. L.; Hyman, L. M.; Derisavifard, S. and Franz, K. J. *Inorg. Chem.* **2010**, Manuscript Submitted. Copyright 2010 American Chemical Society.

hampered by the fluorescence quenching effect of this paramagnetic metal ion. As a consequence, many Cu^{2+} sensors have a "turn-off" mechanism,[131-135] which is generally less sensitive, gives false-positive results, and offers limited spatial resolution. Several examples of turn-on sensors have appeared recently,[128,136-145] but limitations include sensing mechanisms that operate only in organic solvent or at non-physiological pH,[136-138,142] low quantum yields in aqueous solution,[140] or potential off-target responses.[139,143,146,147] Therefore, there is a need to develop new strategies that provide a fluorescent turn-on response in order to investigate intracellular Cu^{2+}. We present here coucage, a new type of fluorescent sensor that uses UV light to uncage a Cu^{2+}-dependent fluorescence response.

Coucage is based on our previously reported copper caging ligand H_2cage,[26] but adapted with coumarin as a fluorescence reporter that is quenched upon Cu^{2+} coordination. The nitrophenyl group incorporated into the backbone of the fluorescent tetradentate chelator is the caging element that blocks activity until activated with light.[3] Exposure to UV light induces bond cleavage, as shown in Scheme 13, which triggers two-fold activity: release of copper by decreasing ligand denticity, and restoration of fluorescence by disengaging the copper-induced quenching.

Scheme 13: Synthesis and Photolysis of [Cu(coucage)]

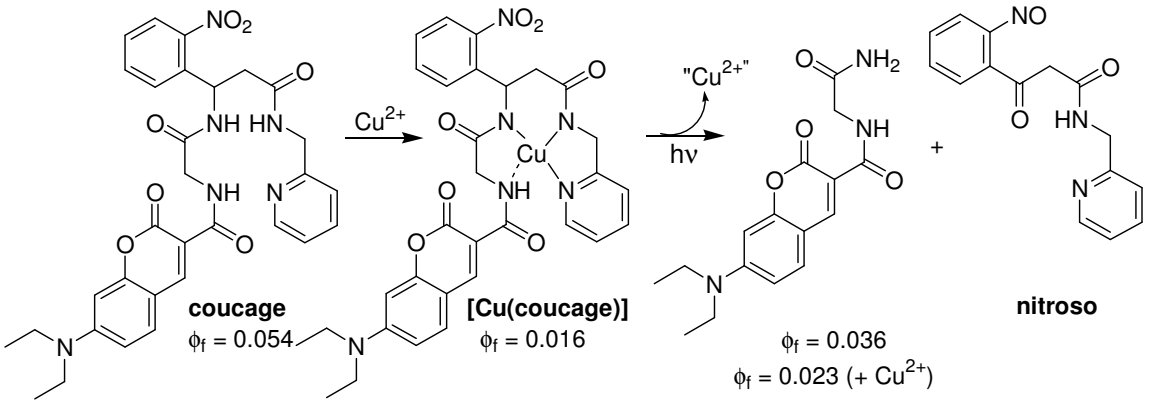

4.2 Materials and Methods

4.2.1 Materials and Instrumentation

Chemicals were purchased commercially and used without further purification. The coumarin derivative 7-diethylamino-2-oxo-2H-chromene-3-carboxylic acid was prepared as described in the literature,[148] or purchased from Aldrich. All reactions were carried out in the dark and glassware was covered with foil. Spectra for 1H NMR were collected on a Varian Inova 400 spectrometer with chemical shifts reported in ppm and J values in Hz. Liquid chromatography/mass spectrometry (LC/MS) was performed using an Agilent 1100 Series apparatus with an LC/MSD trap and a Daly conversion dynode detector. A Varian Polaris C18 (150 × 1.0 mm) column was used and peaks were detected by UV absorption at 256 nm. A linear gradient from 3% A in B to 60% A in B was run from 5 to 40 min with a total run time of 47 min, where A is MeCN / 4% 10 mM ammonium acetate buffer and B is 10 mM ammonium acetate buffer / 2% MeCN. High-resolution electrospray ionization (HR-ESI) mass spectra were recorded on an Agilent 6224 spectrometer. UV-vis spectra were recorded on a Cary 50 UV-vis spectrophotometer and emission spectra were recorded on a Jobin-Yvon-Horiba Fluorolog 3 fluorimeter in a 1 cm pathlength quartz cell. Excitation and emission slit widths were 4 nm and emission spectra were collected from 440 – 600 nm after excitation at 430 nm. Photolysis experiments were performed using a screwtop quartz cuvette illuminated in a Rayonet RPR-100 Photochemical Reactor containing 16 bulbs, each 3500 Å.

4.2.2 Synthesis

Scheme 14: Amcage Synthesis

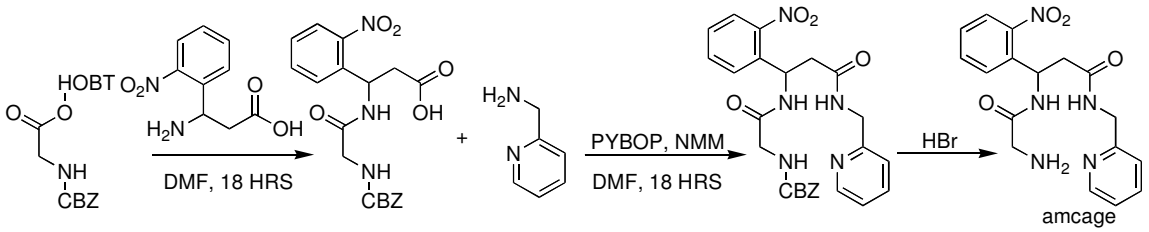

4.2.2.1 3-(2-Amino-acetylamino)-3-(2-nitro-phenyl)-N-pyridin-2-ylmethyl-propionamide (Amcage)

Carbobenzyloxyglycine (0.400 g, 1.912 mmol) and NMM (N-methyl morpholine) (0.420 mL, 3.824 mmol) in CH_2Cl_2 (6 mL) were added to a 150-mL round-bottom flask equipped with a stir bar. Then PyBOP (benzotriazol-1-yl-oxytripyrrolidinophosphonium hexafluorophosphate) (0.996 g, 1.912 mmol) in CH_2Cl_2 (4 mL) was added and the reaction mixture was allowed to stir for 18 h at room temperature. After 18 h, one equivalent of 3-amino-3-(2-nitrophenyl)propionic acid (0.400 g, 1.912 mmol) dissolved in hot DMF (30 mL) was added and the reaction mixture was stirred for an additional 18 h. NMM (0.420 mL, 3.824 mmol) and 2-(aminomethyl)pyridine (0.196 mL, 1.912 mmol), both in CH_2Cl_2 (6 mL) were added to the reaction mixture. PyBOP (0.996 g, 1.912 mmol) in CH_2Cl_2 (4 mL) was then added, and the reaction mixture stirred for 18 h at room temperature. The solvent was removed and the resulting oil was taken up in CH_2Cl_2 (25 mL), filtered, and washed with 1N HCl (3×10 mL). The aqueous layer was

then adjusted to pH 12 and washed with CH_2Cl_2 (4 × 10 mL). The organic layers were combined, dried over $MgSO_4$, filtered, and solvent removal gave an oil that was purified by preparative reverse-phase HPLC on a YMC C18 column (250 × 200 mm I.D.) with a linear 40-min gradient from 7–70% acetonitrile in water, to give a white solid after solvent evaporation. The white solid was then dissolved in CH_2Cl_2 (15 mL) and hydrobromic acid (> 33% in glacial acetic acid) (5 mL) was added and the reaction mixture was allowed to stir for 2 h at room temperature. After 2 h, the reaction mixture was washed with H_2O (4 × 10 mL). The aqueous layer was then adjusted to pH 12 and washed with CH_2Cl_2 (4 × 10 mL). The organic layers were combined, dried over $MgSO_4$, filtered, and solvent removal gave a white solid (0.2164 g, 31.7 %). ^{1}H NMR ($(CD_3)_2CO$): δ 8.45 (1H, d, *J* = 3.97), 7.97 (1H, d, *J* = 8.02), 7.72 (1H, d, *J* = 7.62), 7.64 (2H, m), 7.53 (1H, t, *J* = 7.62, *J* = 7.62), 7.21 (1H, d, *J* = 7.64), 5.91 (1H, t, *J* = 5.37, *J* = 5.37), 4.43 (2H, dd, *J* = 15.98, *J* = 40.76), 3.74 (2H, m), 3.06 (1H, dd, *J* = 6.62, *J* = 14.52), 2.94 (1H, dd, *J* = 4.79, *J* = 14.76). ^{13}C NMR ($(CD_3)_2CO$): δ 169.86, 169.75, 158.24, 148.83, 148.59, 137.67, 136.41, 133.29, 129.20, 128.18, 124.31, 121.90, 120.97, 54.00, 46.47, 44.25, 39.94; LC-MS: m/z 358.1 [M+H]+, M = $C_{17}H_{19}N_5O_4$.

Scheme 15: Coucage Synthesis

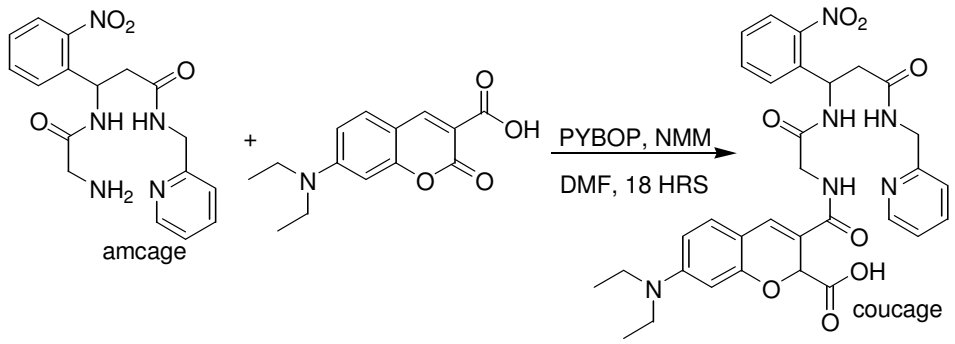

4.2.2.2 Diethylamino-2-oxo-2H-chromene-3-carboxylic acid ({1-(2-nitro-phenyl)-2-[(pyridin-2-ylmethyl)-carbamoyl]-ethylcarbamoyl}-methyl)-amide (Coucage)

Portions of amcage (0.082 g, 0.229 mmol), 7-diethylamino-2-oxo-2H-chromene-3-carboxylic acid (0.050 g, 0.191 mmol) and NMM (0.04 mL, 0.382 mmol) in CH_2Cl_2 (10 mL) were added to a 50-mL round-bottom flask equipped with a stir bar. Then PyBOP (0.099 g, 0.191 mmol) in CH_2Cl_2 (4 mL) was added and the reaction mixture was allowed to stir for 18 h at room temperature. The solvent was removed and the resulting oil was taken up in CH_2Cl_2 (20 mL) and washed with 1N HCl (4 × 10 mL). The aqueous layer was then adjusted to pH 12 and washed with CH_2Cl_2 (4 × 10 mL). The organic layers were combined, dried over $MgSO_4$, filtered, and solvent removal gave a yellow solid (0.040 g, 35%). Analysis by LC-MS and 1H NMR showed > 98% purity. ^{1}H NMR ($(CD_3)_2CO$): δ 8.517 (1H, s), 8.308 (1H, d, *J* = 4.885), 7.821 (1H, d, *J* = 6.839), 7.638 (1H, d, *J* = 7.816), 7.533 (3H, m), 7.388 (1H, t, *J* = 7.816), 7.028 (2H, m), 6.714 (1H, dd, *J* = 2.931, *J* = 5.862), 6.437 (1H, d, *J* = 1.954), 5.720 (1H, m), 4.269 (2H, m),

3.965 (2H, d, *J* = 4.885), 3.4655 (4H, q, *J* = 6.839), 2.984 (2H, m), 1.111 (6H, t, *J* = 7.816); LC-MS: m/z 601.2 [M+H]+, M = $C_{31}H_{32}N_6O_7$; UV-vis (9:1 Hepes:DMSO, pH 7.4), nm ($M^{-1}cm^{-1}$): 430 (16004).

4.2.3 Photolysis of Coucage and [Cu(coucage)]

Solutions of coucage and [Cu(coucage)] were prepared in 9:1 10 mM Hepes, pH 7.4:DMSO. Photoproducts were obtained by photolyzing solutions of coucage for 4 min. All photolysis experiments were performed in a screwtop quartz cuvette illuminated in a Rayonet RPR-100 Photochemical Reactor containing 16 bulbs (14 watts each), with a maximum intensity output at 350 nm. Reaction solutions were analyzed by LC-MS and high resolution electrospray ionization (HR-ESI) to obtain the exact mass and composition of the photoproducts.

4.2.4 Quantum Yield of Fluorescence

100 μM stock solutions of coucage, coucage + UV, coucage + 25 equivalents of $Cu(ClO_4)_2$, coucage + 50 equivalents of $Cu(ClO_4)_2$, coucage + 25 equivalents of $Cu(ClO_4)_2$ + UV, and coucage + 50 equivalents of $Cu(ClO_4)_2$ + UV were diluted to make 1, 2, 3, 4 and 5 μM solutions in 9:1 10 mM Hepes, pH 7.4 : DMSO. Samples designated "+ UV" indicate that they were irradiated for 4 min in the photoreactor. The UV-vis absorbance and fluorescence spectra were obtained for each sample and repeated to ensure reproducibility. Excitation was performed at 430 nm and the integrated

fluorescence emission was recorded from 440–600 nm. A plot of the integrated fluorescence intensity vs. absorbance was prepared for each solution and the result was a straight line. The data were compared to a fluorescein standard in 0.10 M NaOH using the following equation (Equation 8), where ϕ_R is the quantum yield of the standard (0.95) Grad is the slope of the integrated fluorescence intensity vs. absorbance line found for each solution, $Grad_R$ is the slope found for the fluorescein standard, η is the refractive index of 9:1 10 mM Hepes:DMSO solvent system (1.33) and η_R is the refractive index of the fluorescein solution (1.33):

$$\Phi = \Phi_R \frac{\text{Grad}}{\text{Grad}_R} \times \frac{\eta^2}{\eta_R^2} \quad (8)$$

4.2.5 Quantum Yield of Photolysis

The quantum yields of photolysis for coucage and [Cu(coucage)] were determined by comparison to the quantum yield of 1-(o-nitrophenyl)ethyl phosphate (caged Pi) as previously reported by Ellis-Davis and Kaplan.[99] Samples of coucage (100 μM in DMSO), [Cu(coucage)] (100 μM coucage + 5 mM $Cu(ClO_4)_2$ in DMSO), or caged Pi (1 mM in 10 mM Hepes pH 7.4) in 1-cm pathlength cuvettes were irradiated in a Rayonet RPR-100 Photochemical Reactor at 350 nm for 15 s. Photodegradation of the caged compounds was monitored by LC-MS analysis. Aliquots of 6.0 μL of each sample before and after photolysis were injected by autoinjector and run in triplicate. The experiment was repeated to ensure reproducibility. The quantum yield for each sample (Φsample)

was calculated by using the following equation (Equation 9):

$$\Phi_{sample} = \Phi_{cp} \times \frac{\%\Delta sample}{\%\Delta cp} \times \frac{A_{350}cp}{A_{350}sample} \quad (9)$$

where Φcp is 0.54, the reference quantum yield of photolysis for caged Pi, %Δsample and %Δcp are the percent change in integrated peak area after photolysis for the sample and caged Pi, respectively, and A_{350} is the absorbance at 350 nm in a 1-mm cuvette for caged Pi (cp) and for the sample.

4.2.6 UV and Fluorescence Spectra of Coucage

Solutions of 1-5 μM coucage in 9:1 10 mM Hepes, pH 7.4:DMSO were used for fluorescence and UV experiments. The reaction vessel was a 3-mL cuvette and initial solution volumes were at least 1 mL. All experiments were carried out at 25°C. Aliquots of $Cu(ClO_4)_2$ were pipetted into coucage solutions and monitored spectrophotometrically.

4.2.7 Conditional Binding Constant, K_d

Fluorescence spectra of 1 μM coucage in aqueous solution (9:1 10 mM Hepes, pH 7.4:DMSO) with excitation at 430 nm displays an emission maximum at 479 nm that decreases upon titration of $Cu(ClO_4)_2$. The conditional dissociation constant, K_d, was obtained from Equation 10, which relates fluorescence intensity to the concentration of

Cu^{2+}, $[Cu^{2+}]$:

$$\frac{F_o - F}{F - F_\infty} = \left(\frac{[Cu^{2+}]}{K_d} \right)^n \qquad (10)$$

where F_o, F, and F_∞ are the relative fluorescence intensities of coucage, coucage in the presence of a known concentration of Cu^{2+}, and coucage saturated with Cu^{2+} (100 equivalents), respectively, and n is the number of equivalent binding sites on coucage. By plotting log $(F_o - F) / (F - F_\infty)$ vs. log $[Cu^{2+}]$ the slope of the line is equal to n and log (K_d) is equal to log$[Cu^{2+}]$ where log $(F_o - F) / (F - F_\infty) = 0$.

4.2.8 Method of Continuous Variation (Job's Plot)

When carrying out the method of continuous variation the total concentration of coucage and Cu^{2+} were kept constant at 1 μM. All spectra were recorded in aqueous solution (9:1 10 mM Hepes, pH 7.4:DMSO), excitation was performed at 430 nm and emission intensity was measured at 479 nm. $\chi(Cu^{2+})$ is plotted vs. adjusted fluorescence intensity where χ is the mole fraction of Cu^{2+} and the adjusted fluorescence is equal to the fluorescence intensity of sample solution minus the intensity of Cu^{2+} alone, multiplied by the mole fraction of Cu^{2+}.

4.2.9 Metal Specificity Experiments

To monitor the effect of various metal ions on coucage, the integrated

fluorescence response from 440–600 nm was recorded before and after the addition of various metals, following the addition of $Cu(ClO_4)_2$ to solutions containing a metal ion, and after photolysis. Intitial sprectra were taken in 9:1 10 mM Hepes, pH 7.4:DMSO. Various metal ions: 1 mM NaCl, KCl, $MgCl_2$, $CaCl_2$, $ZnSO_4$ or 50 μM $MnSO_4$, $(NH_4)_2[Fe(OH_2)_6(SO_4)_2]$, $CoCl_2$, $NiCl_2$, $[(CH_3CN)_4Cu]PF_6$ were combined with 1 μM coucage and allowed to equilibrate for at least 1 hour. Solutions containing Fe^{2+} and Cu^{+} were kept sealed under N_2. Then 50 μM $Cu(ClO_4)_2$ was added into solution and the final solution was irradiated with 4 min of UV light.

4.2.10 Cell Culture

Lynne Hyman, a graduate student in the Franz laboratory, performed all cell culture experiments. All cell culture reagents, including minimal essential medium (MEM), Dulbecco's modified eagle medium (DMEM), fetal bovine serum (FBS) and trypsin-EDTA (0.25%) were purchased from Gibco. MCF-7 cells were graciously obtained from Dr. Mark Dewhirst's lab (Duke University) and were cultured in complete medium containing DMEM supplemented with 10% (v/v) FBS. Cells were incubated at 37 °C with a fully humidified atmosphere containing 5% CO_2.

4.2.11 Fluorescence Imaging Experiments

Lynne Hyman, a graduate student in the Franz laboratory, performed the fluorescence imaging experiments described below. All live cell confocal images were

taken on a Zeiss Axio Observer widefield fluorescence microscope under 20× magnification using a Plan Neofluar objective lens. A CFP filter set (Zeiss no. 47; BP436/20, FT455, BP480/40) was used to collect fluorescence emission data and a DAPI filter set (Zeiss no. 49; G365, FT395, BP445/50) was used to irradiate samples with UV light (excitation centered at 365 nm with transmittance spanning 300–400 nm). Quantification and image processing were performed with MetaMorph. All microscope settings, including transmission density, brightness, contrast and scan speed, were held constant.

For each experiment, cells were seeded at a density of 40,000 cells/well into a 12-well MatTek glass bottom plate and incubated overnight to ~60% confluence. The growth medium was removed and the cells were washed once with phosphate buffered saline (PBS). 1 mL solutions of 5 μM coucage in MEM with 10% DMSO were added to the wells and incubated for 20 min. The cells were again washed once with PBS and 2 mL of MEM was added. For samples treated with Cu^{2+}, various concentrations of $CuCl_2$ were added directly to the sample and the cells were incubated at 37 °C for 20 minutes. For samples exposed to UV light, two methods were used: 1) the entire plate was placed in the Rayonet photoreactor for 4 min or 2) the samples were directly irradiated on the microscope using the DAPI filter.

4.3 Results

4.3.1 Characterization of Photoproducts

When solutions of coucage and [Cu(coucage)] in 10 mM Hepes, pH 7.4:DMSO are exposed to 350 nm UV light, cleavage of ligand backbone is complete within 4 min, as confirmed by LC-MS and shown in Figure 28. A peak for the intact [Cu(coucage)] complex is not observed as the binding affinity of coucage for Cu^{2+} does not allow it to stay intact as it travels through the LC-MS. Therefore, when coucage in the presence of two equivalents of Cu^{2+} is injected into the LC-MS only a peak for coucage is observed, Figure 28. The peak for intact coucage disappears and is replaced by peaks corresponding to the expected photoproducts **1** and **2**, as confirmed by their mass spectra. The reaction solution was also analyzed by high resolution electrospray ionization (HR-ESI) to obtain the exact mass and composition of the photoproducts, found to be 318.1455 m/z, which corresponds to $C_{16}H_{19}N_3O_4$ (compound **1**) and 284.1033 m/z, which corresponds to $C_{15}H_{13}N_3O_3$ (compound **2**).

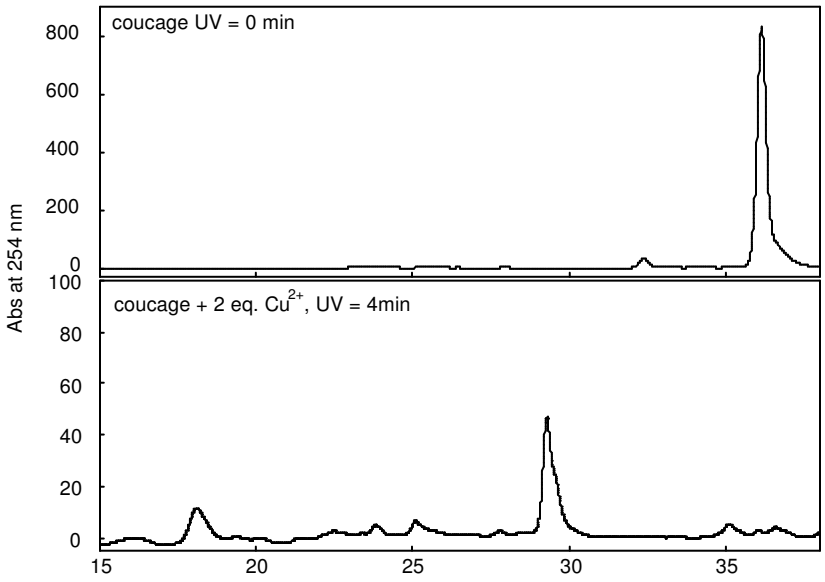

Figure 28: Chromatography Traces for [Cu(coucage)] Pre- and Post- Photolysis

(Top) Chromatography trace from LC/MS analysis of [Cu(coucage)] prior to photolysis, showing peak at 36.0 min for intact coucage (601.2 *m/z*). The copper complex does not remain intact under the LC conditions, so only the free ligand is observed. (Bottom) Chromatography trace of coucage in the presence of 2 equivalents of $Cu(ClO_4)_2$ after 4 min of exposure to UV light. The major products are **1** (18.1 min, 284.1 *m/z*) and **2** (29.3 min, 318.1 *m/z*). For each run, 6 µL aliquots of a 444 µM solution of coucage or 235 µM coucage + 470 µM $Cu(ClO_4)_2$ in 9:1 10 mM Hepes, pH 7.4:MeOH were injected onto the LC/MS.

4.3.2 Quantum Yield of Fluorescence

The calculated quantum yields of fluorescence for coucage and coucage + 25 or 50 equivalents of Cu^{2+} pre- and post-photolysis are shown in Table 5. A plot of the integrated fluorescence intensity vs. absorbance was prepared for each sample at various concentrations and the results were compared to a fluorescein standard using Equation 8.

Table 7: Calculated Quantum Yields

Sample	ϕ
coucage	0.054
coucage + UV	0.036
coucage + 25 eq Cu^{2+}	0.018
coucage + 50 eq Cu^{2+}	0.016
coucage + 25 eq Cu^{2+} + UV	0.023
coucage + 50 eq Cu^{2+} + UV	0.023

4.3.3 Quantum Yield of Photolysis

Comparison of the integrated peak areas indicated that after 15 s of UV exposure, 43.3% of the caged Pi, 24.5% of coucage, and 31.4% of [Cu(coucage)] had been photolyzed. The calculated quantum yields of photolysis for coucage and [Cu(coucage)] are 0.51 and 0.68, respectively, which indicates that coordination of the ligand to Cu^{2+} does not decrease photolysis efficiency.

4.3.4 UV and Fluorescence Spectra of Coucage

The absorbance spectrum of 5 μM coucage in aqueous solution (9:1 10 mM Hepes, pH 7.4:DMSO) displays a peak in the visible region centered at 432 nm. Addition of 0, 5 10, 15, 20, 25, 30, 35, 40, 45 and 50 μM $Cu(ClO_4)_2$ shows a decrease in the peak at 430 nm and an increase in the peak at 260 nm, no additional spectral changes are apparent after the addition of 30 μM Cu^{2+}, Figure 29.

Fluorescence spectra of 1 μM coucage in aqueous solution (9:1 10 mM Hepes, pH 7.4:DMSO) with excitation at 430 nm has an emission maximum at 479 nm that decreases upon titration of $Cu(ClO_4)_2$ with maximum quenching observed after the addition of approximately 50 equivalents (Figure 30). The depressed fluorescence of solutions containing coucage and Cu^{2+} can be restored to nearly half the original intensity by irradiation at 350 nm, as shown by the thick spectral trace in Figure 30.

To ensure that the decrease in fluorescence is caused by reversible Cu^{2+} binding, 1.5 μM coucage was combined with 10 μM $Cu(ClO_4)_2$ to observe the quenched fluorescence, then 10 μM EDTA was added into the reaction mixture. The fluorescence was nearly restored, as shown in Figure 31, indicating that the decease in intensity is caused by Cu^{2+} and is reversible.

To investigate the effect of pH on [Cu(coucage)], 1 μM coucage was combined with 10 equivalents of $Cu(ClO_4)_2$ in 9:1 10 mM Hepes:DMSO. The pH was adjusted with 1 M NaOH to obtain solutions of pH 6, 7, 8, 9 and 11. Fluorescence spectra were recorded at each pH. As shown in Figure 32, altering the pH of the reaction mixture to

pH $\geq$ 8 causes a dramatic decrease in fluorescence. This result implies that at pH < 8 the proton on the amide nitrogen closest to coumarin is not deprotonated. However, at pH $\geq$ 8 this amide is deprotonated bringing Cu^{2+} in close proximity to coumarin and causing additional quenching.

To identify the effect of Cu^{2+} on the fluorescence intensity of the photoproducts, 1 μM coucage in the absence of metal was exposed to 4 min UV light. As shown in Figure 33, the addition of 50 equivalents of Cu^{2+} to this photolyzed solution causes a 26% decrease in intensity. In contrast, Cu^{2+} causes a 70% decrease in fluorescence of intact coucage. These results show that the presence of Cu^{2+} has less of an effect on the fluorescence output of the photoproducts compared to intact coucage.

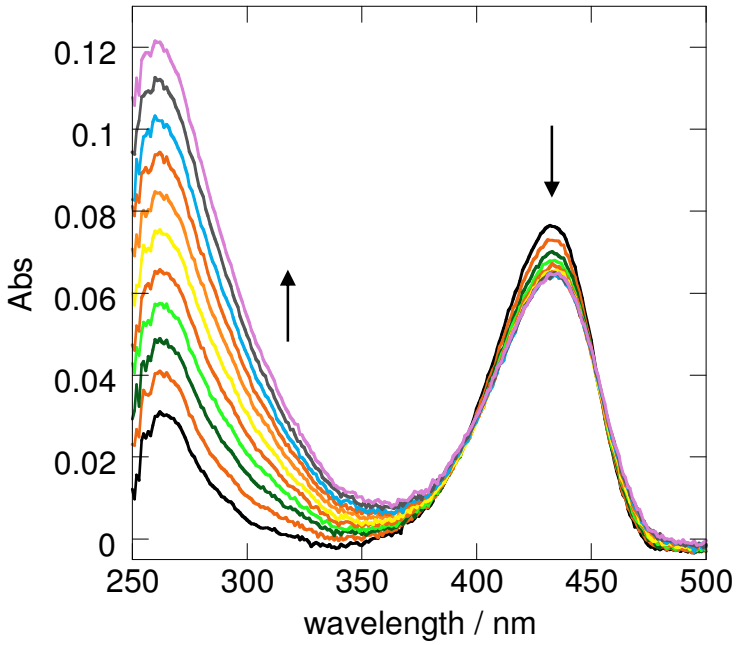

Figure 29: Absorbance Spectra of $Cu(ClO_4)_2$ Titrated into a Solution of Coucage

Absorbance spectra of 5 µM coucage in aqueous solution (9:1 10 mM Hepes, pH 7.4: DMSO) titrated with 10 equivalents $Cu(ClO_4)_2$. Coucage has a λ_{max} centered at 432 nm. Titration of $Cu(ClO_4)_2$ causes a decrease in the peak at 432 nm and an increase in the peak at 260 nm.

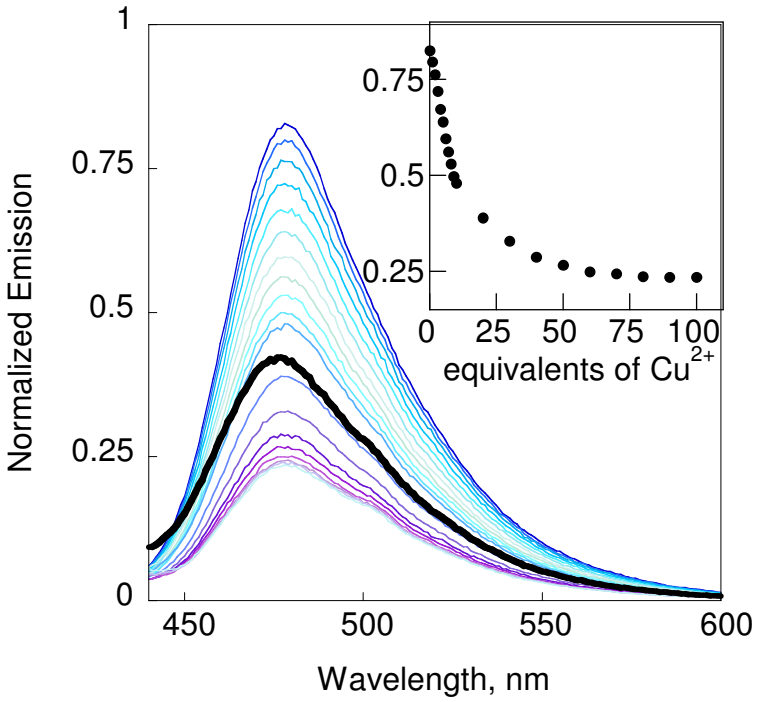

Figure 30: Fluorescence Spectra of Coucage Titrated with $Cu(ClO_4)_2$ then Photolyzed

Fluorescence decrease of 1 μM coucage with 0–100 equivalents Cu^{2+}, along with the subsequent increase following UV exposure (thick black trace). Inset: Emission at 479 nm vs. added Cu^{2+}.

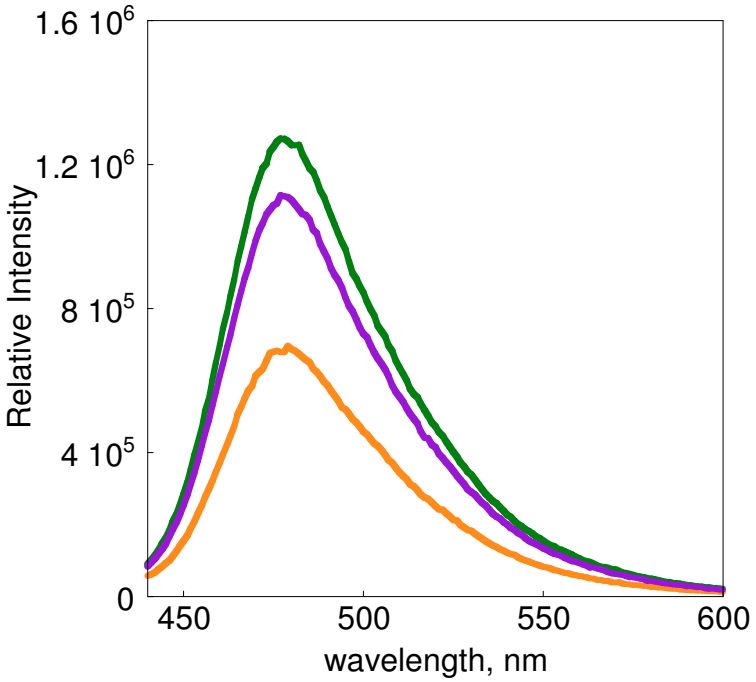

Figure 31: Reversible Fluoresescence Quenching upon the Addition of EDTA

The fluorescence spectrum of 1.5 µM coucage in 9:1 10 mM Hepes, pH 7.4:DMSO (green line) decreases by half following addition of 15 µM $Cu(ClO_4)_2$ (orange line), then nearly returns to initial intensity upon addition of 15 µM EDTA (purple line). These spectra show that the decrease in fluorescence due to Cu^{2+} is reversible upon the addition of EDTA as a competitive chelator.

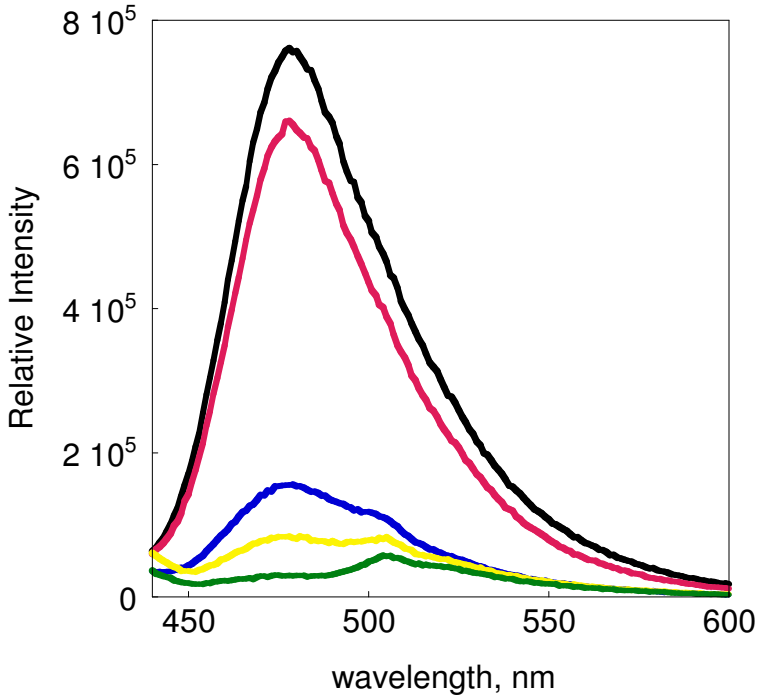

Figure 32: pH Variation of [Cu(coucage)] Solutions

1 µM coucage + 10 µM $Cu(ClO_4)_2$ in 9:1 10 mM Hepes:DMSO at pH 6 (black line), 7 (red line), 8 (blue line), 9 (yellow line), 11 (green line). These results support the hypothesis that at pH ≥ 8 the amide closest to coumarin is deprotonated bringing Cu^{2+} in close proximity for maximal quenching.

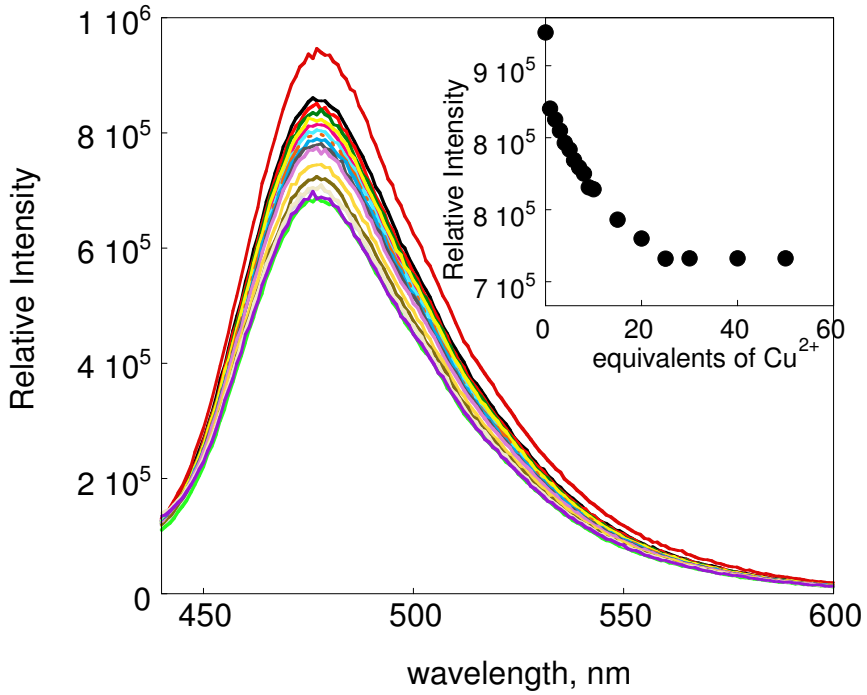

Figure 33: Fluorescence Spectra of Coucage Photoproducts Titrated with $Cu(ClO_4)_2$

Fluorescence spectra of 1 μM coucage after 4 min of UV light exposure (top, red line), then titrated with up to 50 μM $Cu(ClO_4)_2$, which causes a decrease in fluorescence. All samples in 9:1 10 mM Hepes, pH 7.4:DMSO. Inset: Relative intensity vs. equivalents of Cu^{2+} shows that the photoproducts are completely saturated with Cu^{2+} at a concentration of 25 μM.

4.3.5 Conditional Binding Constant, K_d

The affinity of coucage for $Cu(ClO_4)_2$ was assessed using fluorescence by titrating copper into a solution of the ligand. The conditional binding constant can be obtained by plotting log $(F_o - F) / (F - F_\infty)$ vs. log $[Cu^{2+}]$, log (K_d) is equal to log$[Cu^{2+}]$ where log $(F_o - F) / (F - F_\infty) = 0$. Figure 34 represents a typical plot of log $(F_o - F) / (F - F_\infty)$ vs. log $[Cu^{2+}]$ for coucage, which gives an apparent K_d for [Cu(coucage)] of 7.32 (0.89) μM.

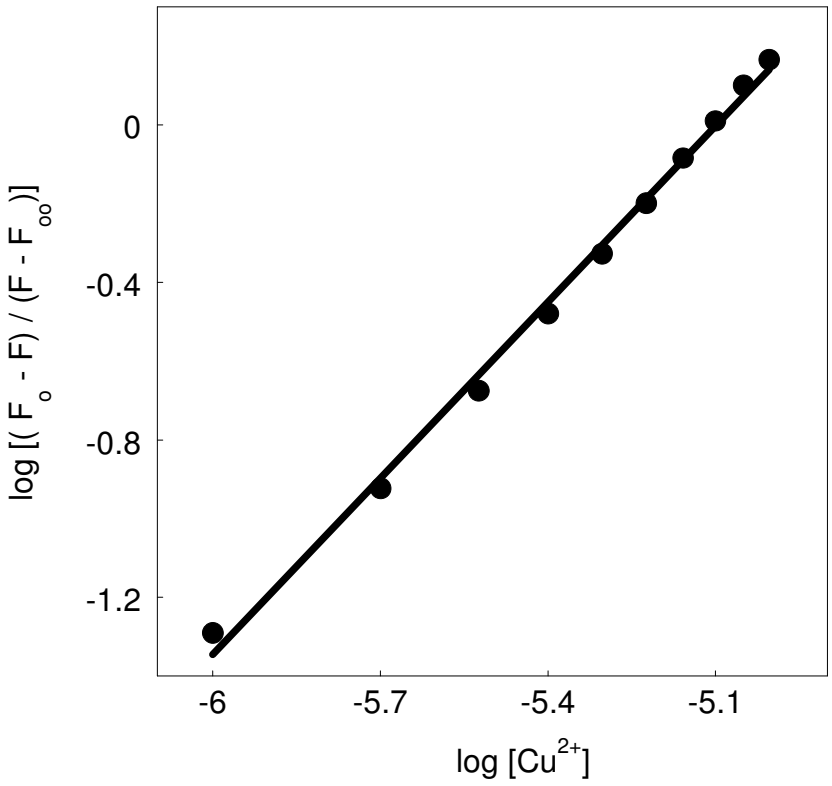

Figure 34: Double-Logarithmic Plot of the Quenching of Fluorescence of Coucage by the Titration of Cu^{2+}

Where F_o, F and F_∞ are the relative fluorescence intensities of coucage, coucage in the presence of a known concentration of Cu^{2+} and coucage saturated with Cu^{2+} (100 equivalents), respectively. The slope of the linear least squares line is equal to the number of equivalent binding sites on coucage and log K_d is equal to log[Cu^{2+}] where log (F_o-F) / (F-F_∞) = 0.

4.3.6 Method of Continuous Variation (Job's Plot)

The binding of $Cu(ClO_4)_2$ to coucage was assessed using fluorescence and the method of continuous variation. The total concentration of coucage and copper were kept constant at 1 μM. As the mole fraction of copper in solution increases the fluorescence intensity at 479 nm decreases. A plot of adjusted fluorescence intensity vs. $\chi(Cu^{2+})$, where adjusted fluorescence intensity is equal to the fluorescence intensity of sample solution minus the intensity of Cu^{2+} alone, multiplied by the mole fraction of Cu^{2+} and $\chi(Cu^{2+})$ is the mole fraction of Cu^{2+}. This plot maximizes at 0.5 mole fraction of Cu^{2+} (Figure 35), indicating that Cu^{2+} and coucage form a 1:1 complex.

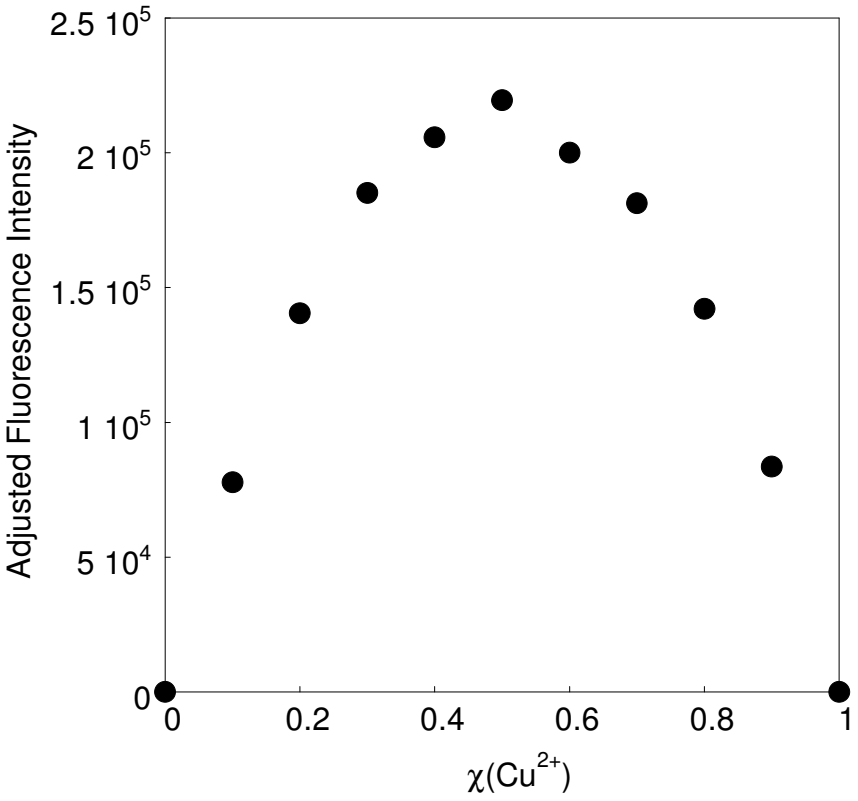

Figure 35: Job's Plot of Coucage and Cu^{2+}

Job's Plot of coucage and Cu^{2+}, indicating formation of a 1:1 complex. $\chi(Cu^{2+})$ is the mole fraction of Cu^{2+}, and the adjusted fluorescence intensity is equal to the fluorescence intensity of sample solution minus the intensity of Cu^{2+} alone, multiplied by the mole fraction of Cu^{2+}. The total concentration of coucage and Cu^{2+} were kept constant at 1 μM. All spectra were collected in aqueous solution (9:1 10 mM Hepes: DMSO) at pH 7.4.

4.3.7 Metal Specificity of Coucage

As shown if Figure 36, no significant fluorescence changes were observed when high concentrations of various metal cations (1 mM Na^+, K^+, Mg^{2+}, Ca^{2+}, Zn^{2+} or 50 μM Mn^{2+}, Fe^{2+}, Co^{2+}, Ni^{2+}, Cu^+) were added into a 1 μM solution of coucage. Upon the addition of 50 μM $Cu(ClO_4)_2$ the fluorescence intensity decreases and is partially restored after 4 minutes of UV exposure.

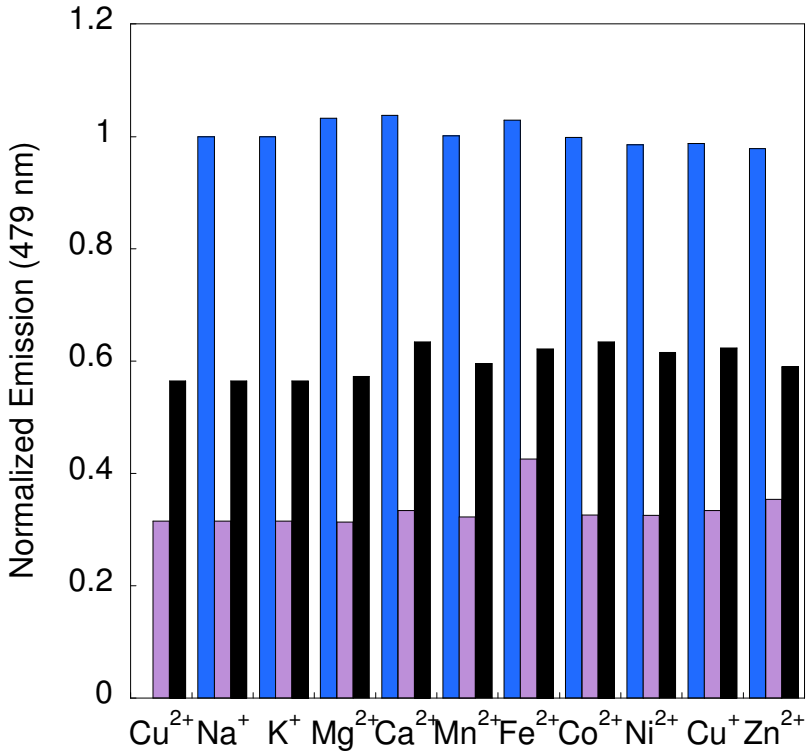

Figure 36: Metal Specificity of Coucage

Blue bars: the unchanged fluorescence of 1 μM coucage in the presence of 1 mM Na^+, K^+, Mg^{2+}, Ca^{2+} and Zn^{2+} or 50 μM for others; Purple bars: quenched emission upon addition of 50 μM Cu^{2+}; black bars: restored fluorescence after 4 min of UV exposure. All samples prepared in 10 mM Hepes buffer at pH 7.4 with 10% DMSO and excited at 430 nm.

4.3.8 Imaging Experiments and Effects of Coucage, Cu^{2+}, and UV on MCF-7 Cells

Cells incubated with coucage alone (Figure 37) show a high fluorescence response. Coordination of Cu^{2+} dims the fluorescence output until irradiation with UV light cleaves the ligand backbone, which relieves the copper-induced quenching to provide a turn-on response (Figure 38-41). These experiments demonstrate that coucage is cell permeable and can detect an increase of intracellular Cu^{2+} at concentrations ranging from 25-125 μM exogenous copper.

Brightfield images after treatment with Cu^{+2} and UV exposure show that cells remain viable throughout the imaging experiment (Figure 42). In addition, Figure 43 shows that cells irradiated with UV light at varying time intervals remain viable for at least 24 hours.

To assess photobleaching under our experimental conditions a CFP filter set was used to continuously excite the sample at 436 nm and collect the emission intensity at 480 nm every 5 seconds. With this filter set, direct photocleavage of coucage is negligible, so any loss in intensity can be attributed to photobleaching. Data were collected for a total of 145 seconds and normalized to 100% to show that the emission signal only decreases by 15% after 40 seconds (Figure 44). For imaging experiments described throughout this work, samples were irradiated for only 3 seconds before collecting emission data, a timeframe for which photobleaching is not a concern.

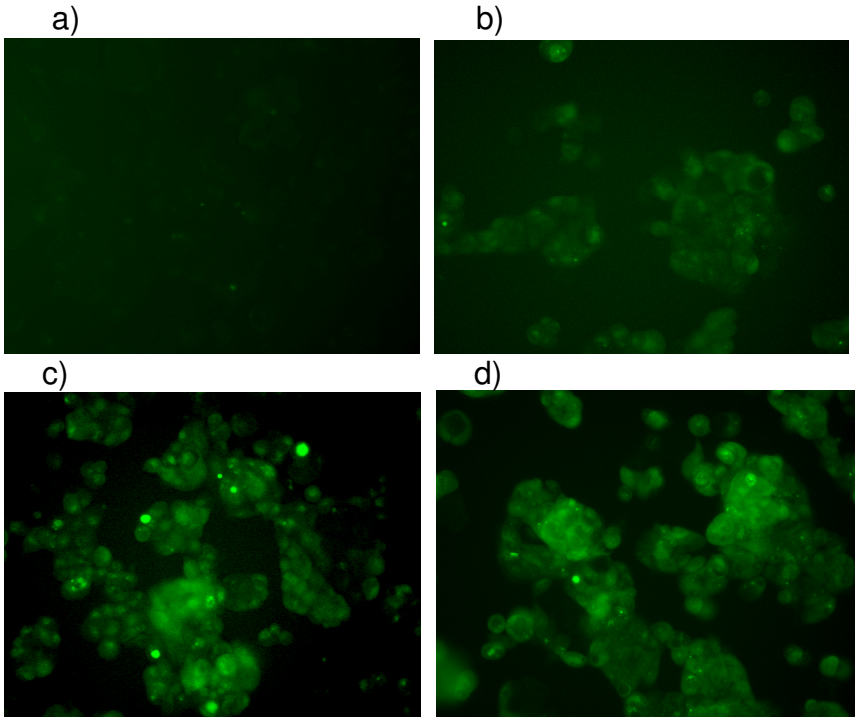

Figure 37: Fluorescence Microscopy Images of MCF-7 Cells Incubated with Coucage

MCF-7 cells incubated for 20 minutes at 37 ºC with a) 0 µM coucage, b) 1 µM coucage, c) 3 µM coucage, and d) 5 µM coucage.

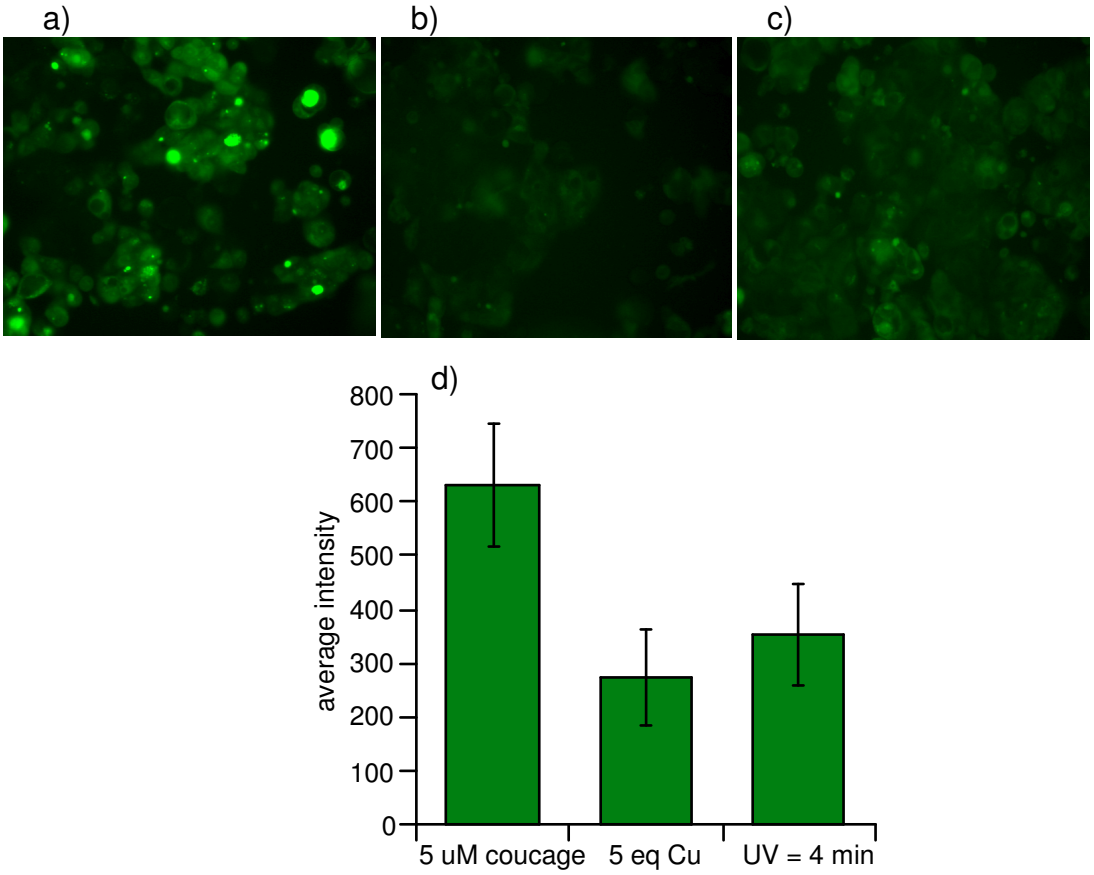

Figure 38: Fluorescence Microscopy Images of MCF-7 Cells Incubated with Coucage and 5 Equivalents Cu^{2+}

Fluorescence microscopy images of MCF-7 cells incubated with a) 5 µM coucage. b) Image of MCF-7 cells from a) incubated with 5 equivalents of $CuCl_2$ (25 µM). c) Image of the cells irradiated with 4 minutes of UV light (350 nm) in a Rayonet photoreactor. d) Bar graph representing the average intensity of illuminated fields on 10 images collected from each condition where the average intensity of the background from all 10 images was subtracted to obtain the final value.

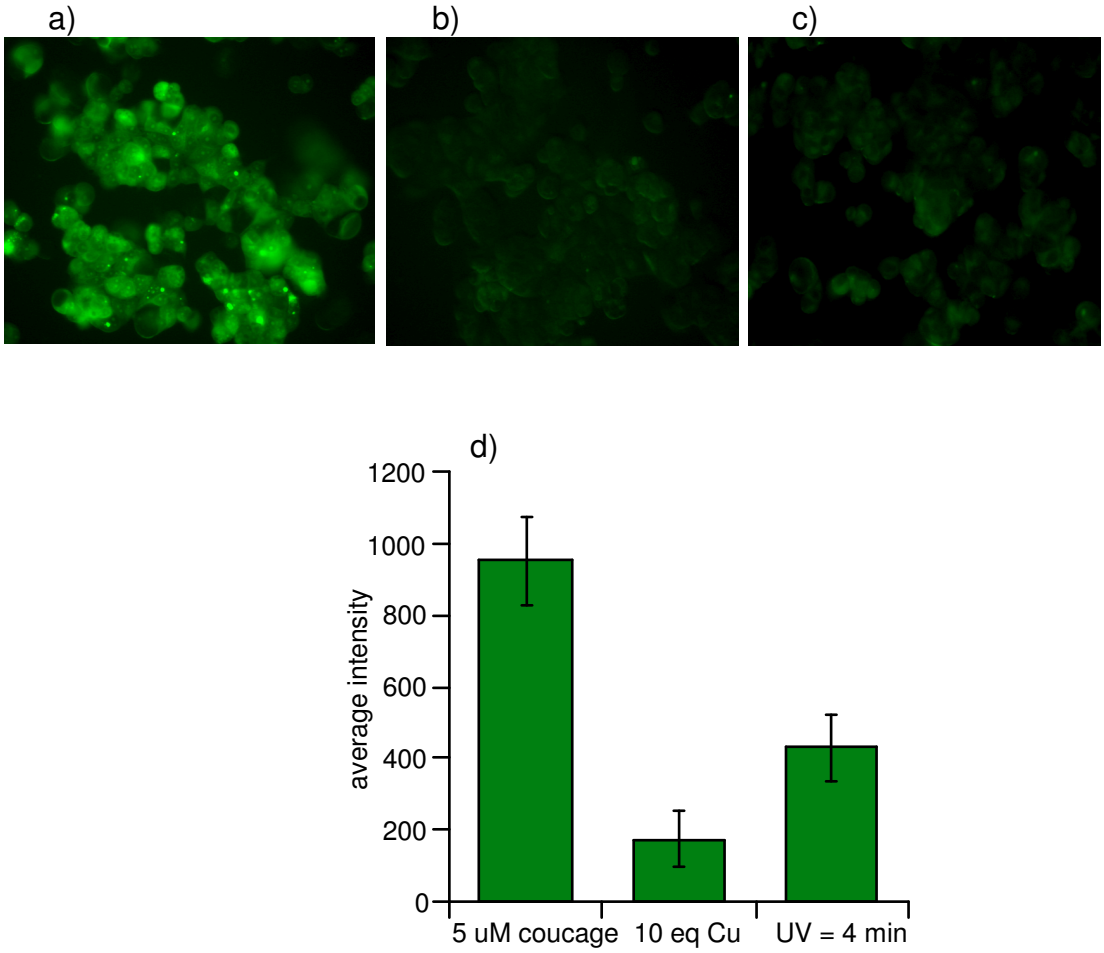

Figure 39: Fluorescence Microscopy Images of MCF-7 Cells Incubated with Coucage and 10 Equivalents Cu^{2+}

Fluorescence microscopy images of MCF-7 cells incubated with a) 5 µM coucage. b) Image of MCF-7 cells from a) incubated with 10 equivalents of $CuCl_2$ (50 µM). c) Image of the cells irradiated with 4 minutes of UV light (350 nm) in a Rayonet photoreactor. d) Bar graph representing the average intensity of illuminated fields on 10 images collected from each condition where the average intensity of the background from all 10 images was subtracted to obtain the final value.

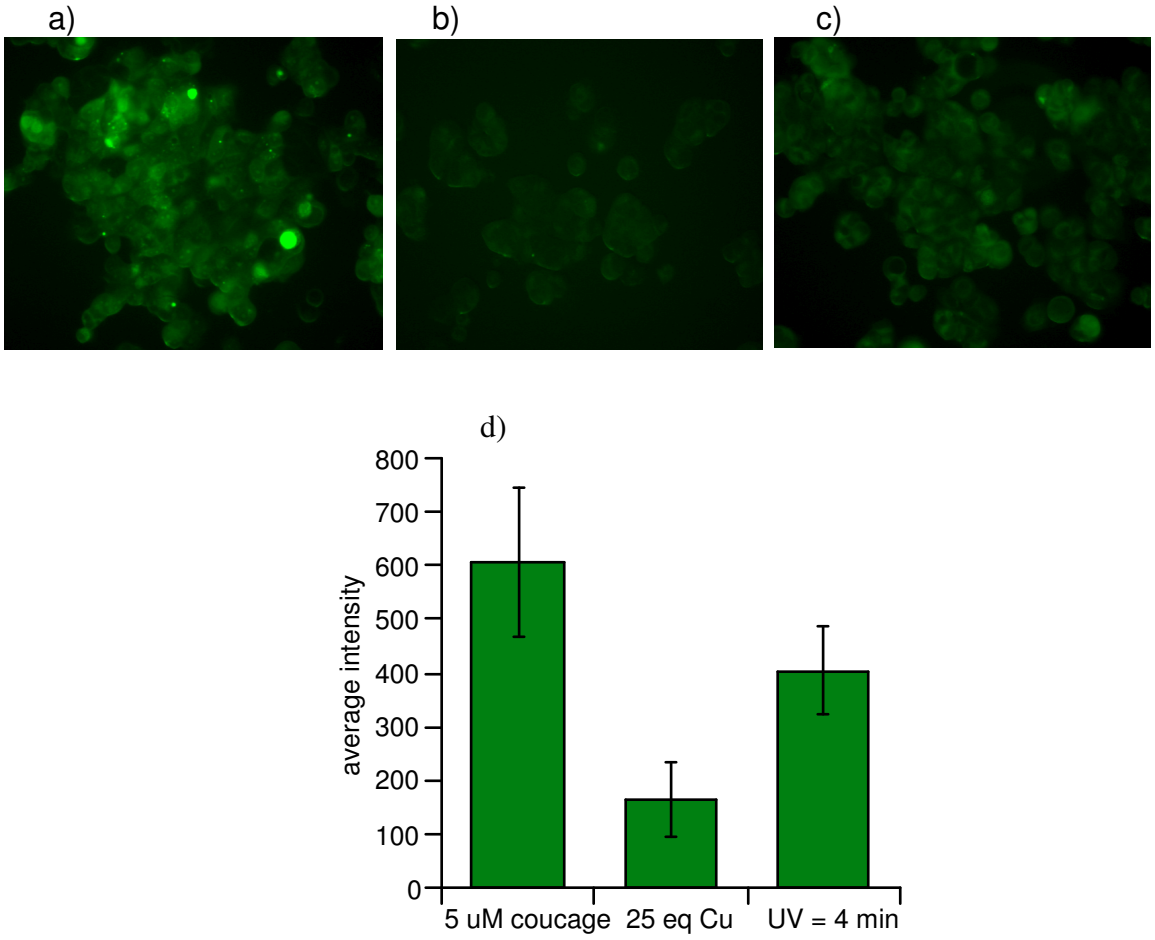

Figure 40: Fluorescence Microscopy Images of MCF-7 Cells Incubated with Coucage and 25 Equivalents Cu^{2+} and Photolyzed in a Photoreactor

Fluorescence microscopy images of MCF-7 cells incubated with a) 5 µM coucage. b) Image of MCF-7 cells from a) incubated with 25 equivalents of $CuCl_2$ (125 µM). c) Image of the cells irradiated with 4 minutes of UV light (350 nm) in a Rayonet photoreactor. d) Bar graph representing the average intensity of illuminated fields on 10 images collected from each condition where the average intensity of the background from all 10 images was subtracted to obtain the final value.

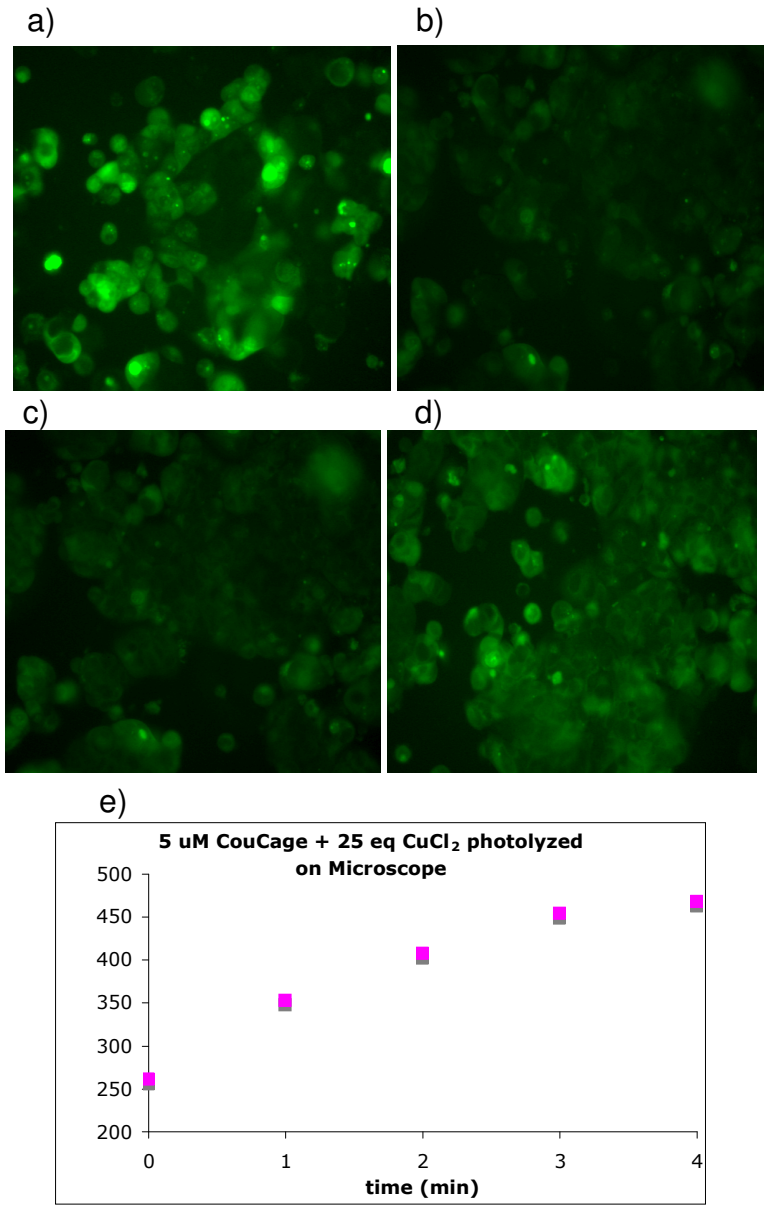

Figure 41: Fluorescence Microscopy Images of MCF-7 Cells Incubated with Coucage and 25 Equivalents Cu^{2+} and Photolyzed on Microscope

Fluorescence microscopy images of a) 5 µM coucage b) after the addition of 25 equivalents $CuCl_2$, c) followed by 4 minutes of UV exposure on the confocal microscope, and d) after 4 minutes UV exposure with the Rayonet photoreactor. Images b and c show the same field of cells before and after UV exposure. Images a) and d) are taken from the same plate of cells, only at a different field of view. e) Plot showing the change in fluorescence intensity of a single spot of illuminated cells after UV exposure through the DAPI filter on the confocal microscope (excitation centered at 365 nm).

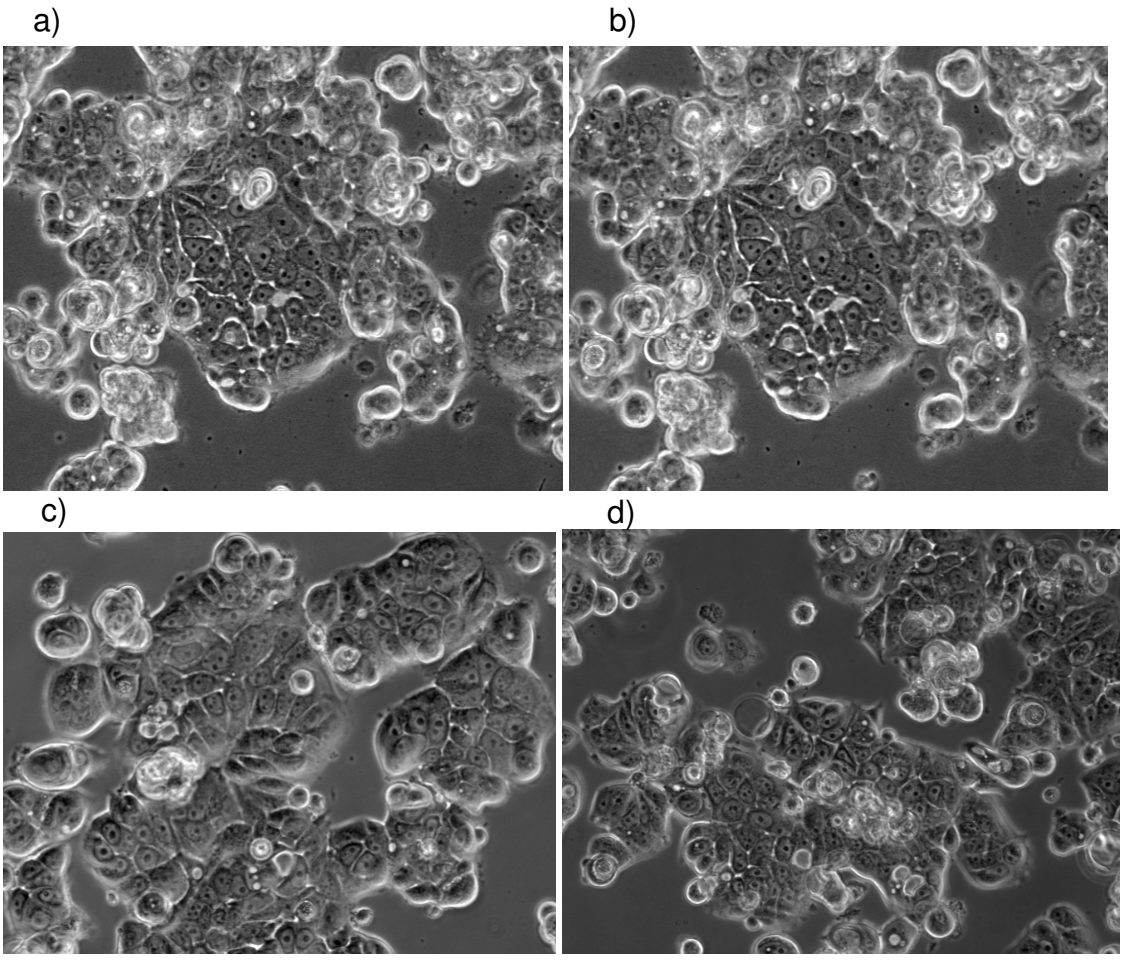

Figure 42: Brightfield Microscopy Images of MCF-7 Cells after Treatment with UV and Cu^{2+}

Brightfield microscopy images of MCF-7 cells before a) and after b) UV irradiation for 4 minutes using the DAPI filter on the microscope; c) after 4 min of UV exposure in the Rayonet photoreactor; d) after 20 min incubation with 250 µM $CuCl_2$. Images show that the level of cell viability is maintained after UV and Cu^{2+} exposure during the timeframe of the experiment.

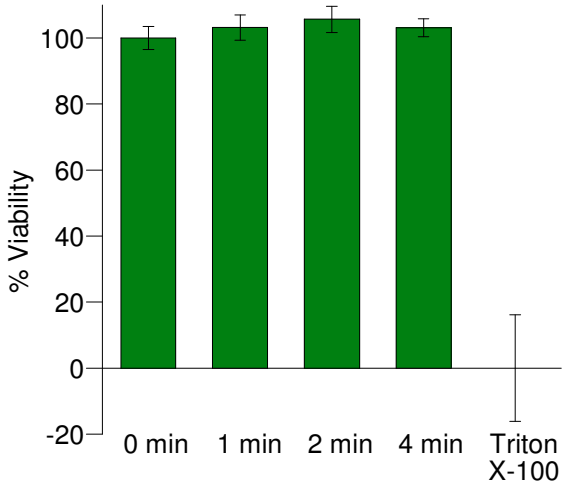

Figure 43: Results of MCF-7 Cell Viability Assay

MCF-7 cells were irradiated with UV light in the Rayonet Photoreactor at varying time intervals and then incubated for 24 h prior to assessing cytotoxicity by an LDH assay, which measures the amount of lactate dehydrogenase released by damaged or dead cells. The results show that 4 min of irradiation in the Rayonet Photoreactor does not cause a decrease in cell viability.

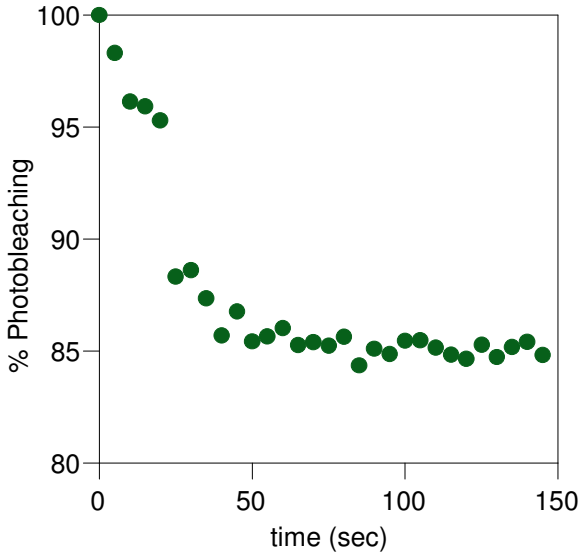

Figure 44: Results of Coucage Photobleaching Experiment

Cells were treated with 5 µM coucage and washed before imaging. The CFP filter set was used to continuously excite the sample at 436 nm and collect the emission intensity at 480 nm every 5 seconds. With this filter set, direct photocleavage of coucage is negligible, so any loss in intensity can be attributed to photobleaching. Data were collected for a total of 145 sec and normalized to 100% to show that the emission signal only decreases by 15% after 40 seconds.

4.4 Discussion

4.4.1 Spectral Properties

Coucage displays an absorbance band at 432 nm that gives a corresponding fluorescence emission maximum at 479 nm with a quantum yield of 0.054. Figure 30 shows that its fluorescence at pH 7.4 is quenched by 75% when saturated with Cu^{2+}, giving a quantum yield of 0.016 and a conditional dissociation constant, K_d, of 7.3 ± 0.9 μM. The 1:1 coucage:Cu^{2+} ratio for complex formation was confirmed by the method of continuous variation (Figure 35).

The depressed fluorescence of solutions containing coucage and Cu^{2+} can be restored to nearly half the original intensity by irradiation at 350 nm, as shown by the thick spectral trace in Figure 30. The emission maximum of photolyzed samples shifts slightly to 475 nm, with a quantum yield of 0.023. The fluorescence of the photolyzed products does not return to initial levels for at least two reasons, the first being that the quantum yield of photolyzed coucage itself (0.036) is lower than the parent compound. The second is that Cu^{2+} retains some quenching effect on the photoproducts, although to a much lesser extent than on intact coucage (see Figure 33).

4.4.2 Metal Specificity of Coucage

Unlike the response observed with Cu^{2+}, no significant fluorescence changes are observed for coucage in the presence of other metal cations, as shown in Figure 36 for Na^{+}, K^{+}, Mg^{2+}, Ca^{2+}, Mn^{2+}, Fe^{2+}, Co^{2+}, Ni^{2+}, Cu^{+}, and Zn^{2+}. When $Cu^{2+}$is added back to

these solutions, the fluorescence decreases by 70% (Figure 36, purple bars), confirming coucage's high selectivity for Cu^{2+} over other biologically important metal ions. The fluorescence can again be partially restored upon irradiation, as shown by the black bars in Figure 36.

4.4.3 Photolysis of Coucage and [Cu(coucage)]

The increase in fluorescence upon irradiation of [Cu(coucage)] is apparent immediately, and cleavage of the ligand backbone is complete in approximately 3 min. The quantum yield of photolysis for coucage and coucage in the presence of Cu^{2+} is 0.51 and 0.68 respectively, indicating that coordination by Cu^{2+} does not decrease photolysis efficiency, as previously observed for [Cu(cage)].[26] Analysis of the reaction mixture by liquid chromatography mass spectrometry (LC-MS) revealed **1** and **2** as photoproducts (Figure 28).

4.4.4 pH Dependence of Fluorescence Quenching

In order for coucage to bind tightly to Cu^{2+}, all three amide protons must be deprotonated. The fact that only 75% fluorescence quenching is achieved at pH 7.4 suggests that the amide proton closest to the coumarin is not fully deprotonated at this pH, setting up a H^+/Cu^{2+} competition that precludes maximum fluorescence quenching. Indeed, increasing the pH of coucage/Cu^{2+} solutions above 8 dramatically decreases fluorescence, leaving only a residual 10% signal by pH 9 (Figure 32). Although the

greatest fluorescence quenching is observed at high pH, coucage remains biologically applicable since a Cu^{2+} turn-off response is observed at pH 7.4.

4.4.5 Fluorescence Microscopy Imaging in MCF-7 Cells

To test coucage in living cells, we treated human breast carcinoma MCF-7 cells with coucage and Cu^{2+} and observed the intracellular fluorescence of irradiated vs. non-irradiated cells using scanning confocal microscopy. MCF-7 cells incubated with coucage alone initially show a high fluorescence response, as shown in Figure 40a. After addition of excess Cu^{2+} to the cell culture media and incubation for 20 min, the intracellular fluorescence signal decreases by 70%, indicating that Cu^{2+} has coordinated to coucage inside the cells (Figure 40b). Cu^{2+}-treated cells exposed to UV light from a Rayonet photoreactor for 4 min exhibit bulk fluorescence restoration up to 67% of the original intensity, as seen in Figure 40c. Cells were also irradiated directly on the microscope (Figure 41). Although this method provides a less distinct fluorescence increase, it demonstrates the possibility of observing the turn-on response within one field of view. Control experiments in the absence of fluorophore show no background fluorescence and photobleaching of coucage results in less than 2% intensity loss during the 3 s excitation times used to collect images (Figure 44). Brightfield images after coucage, Cu^{2+}, and UV exposure show that cells remain viable throughout the imaging experiment (Figure 42).

4.5 Summary and Conclusion

In conclusion, we have presented a new strategy for achieving a fluorescence turn-on response to detect Cu^{2+} in living cells. The sensor relies on a coumarin-tagged ligand that selectively binds Cu^{2+} over other biometals to induce fluorescence quenching, which is subsequently relieved upon UV irradiation to provide the turn-on response. In essence, the strategy reports on the memory of where Cu^{2+} had been available for chelation by the 7 μM binder. Because the probe is destroyed during the readout, this strategy inherently cannot provide real-time monitoring of cellular Cu^{2+} fluctuations. Experiments in live MCF-7 cells demonstrate that coucage is cell permeable and can detect an increase of intracellular Cu^{2+} under conditions of excess exogenous copper. Copper is imported in its reduced Cu^{+} oxidation state, and intracellularly is believed mostly to remain in its reduced form. However, subcellular microenvironments may support Cu^{2+}, and the coucage strategy introduced here might find utility in providing snapshots of such Cu^{2+}, provided that improvements can be made to the ligand to make it more sensitive. Future investigations are therefore aimed at improving the quenching efficiency of the copper complex at physiological pH and increasing the binding affinity in order to create a more sensitive probe, as well as applying photoactive fluorescent ligands to other biologically interesting metal ions.

5. Development of Next-Generation Photolabile Copper Cages with Improved Copper Binding Properties[1]

5.1 Background and Significance

Copper is an essential element for life and plays an important role in many physiological processes. Its redox activity makes it an essential cofactor in enzymes such as Cu, Zn superoxide dismutase, cytochrome oxidase, ceruloplasmin, tyrosinase, peptidyl-glycyl α-amidating monooxidase, and many others.[91] The same property that makes copper essential renders it potentially toxic when there is an imbalance in its cellular homeostasis, which can lead to the formation of toxic reactive oxygen species (ROS).[126] Metal-induced oxidative stress is associated with several neurodegenerative diseases including Menkes and Wilson diseases, Alzheimer's disease, familial amyotropic lateral sclerosis and prion disease.[90,93,127,149] Due to the potentially toxic nature of copper, cells tightly regulate its intracellular distribution.[150-154] Understanding how cells traffic and utilize copper while suppressing its toxicity has important ramifications for health and disease.[92,93,150-154]

It has been shown that copper levels are elevated in numerous malignancies and directly correlate to cancer progression.[155] In addition, cancer cells are known to have elevated levels of oxidative stress due to an increase generation of ROS,[155,156] which

---

[1] Reproduced in part with permission from Ciesienski, K. L. and Franz, K. J **2010**, *Manuscript in Preparation*. Copyright 2010.

results in cells trying to adapt mechanisms to neutralize oxidative stress and in turn they may exhaust their cellular ROS-buffering capabilities.[157,158] Therefore, copper's pro-oxidant ability is medicinally promising if it can be used to selectively induce oxidative stress as a cancer chemotherapy strategy. New methods for controlling the spatial and temporal release of copper intracellularly would be useful for both the targeted delivery of copper as a pro-oxidant to induce cell death and for uncovering its complex involvement in healthy vs. disease states. Toward these goals, we have developed photoactive caged copper complexes by incorporating a nitrophenyl group into the backbone of copper-binding ligands. Our previously reported first-generation chelator, nicknamed **H_2cage**, cages Cu^{2+} in a tetradentate binding site until exposure to UV light cleaves the ligand backbone to release photoproducts with diminished affinity for Cu^{2+}.[26] In addition to the change in binding affinity, photolysis also causes a change in reactivity of caged vs. uncaged copper, as we have shown by the 160% increase in the ability of copper to generate hydroxyl radicals under Fenton-like conditions following light-induced uncaging. While these are promising steps towards using light-activated compounds to increase oxidative stress in a targeted manner, H_2cage is not without its limitations. One of its drawbacks is that it does not completely suppress hydroxyl radical formation pre-photolysis. Furthermore, its effective dissociation constant, K_d', at pH 7.4 of 16 pM is not strong enough to keep copper sequestered in the presence of endogenous copper-binding proteins. For example, copper circulates in serum predominantly bound to human serum albumin, which has a K_d' of 1 pM for Cu^{2+} at physiological pH.[159]

To address these problems, we synthesized and characterized seven new photolabile analogs of H_2cage, the structures of which are shown in Figure 45. Our primary goals in this study were to investigate the effects of changes in the ligand backbone of H_2cage on Cu^{2+} chelation and reactivity. Studies on several of the second-generation analogs revealed that replacement of at least one amide nitrogen in H_2cage with a secondary amine improves the ligand's affinity for Cu^{2+}. This information led to the design of our best copper cage to date, the 3rd generation chelator nicknamed **3Gcage**. As shown in Scheme 16, 3Gcage chelates copper with two pyridyl nitrogens, an amide, and a secondary amine. Exposure to UV light cleaves the ligand backbone to release the expected picolinamide (**pic**) and nitroso-containing (**nitroso**) fragments with weaker copper affinity. 3Gcage not only has a significantly improved Cu^{2+} binding affinity, it also retains a high quantum efficiency of photolysis and provides greater protection against copper-promoted hydroxyl radical formation pre-photolysis, while maintaining the increased reactivity post-photolysis.

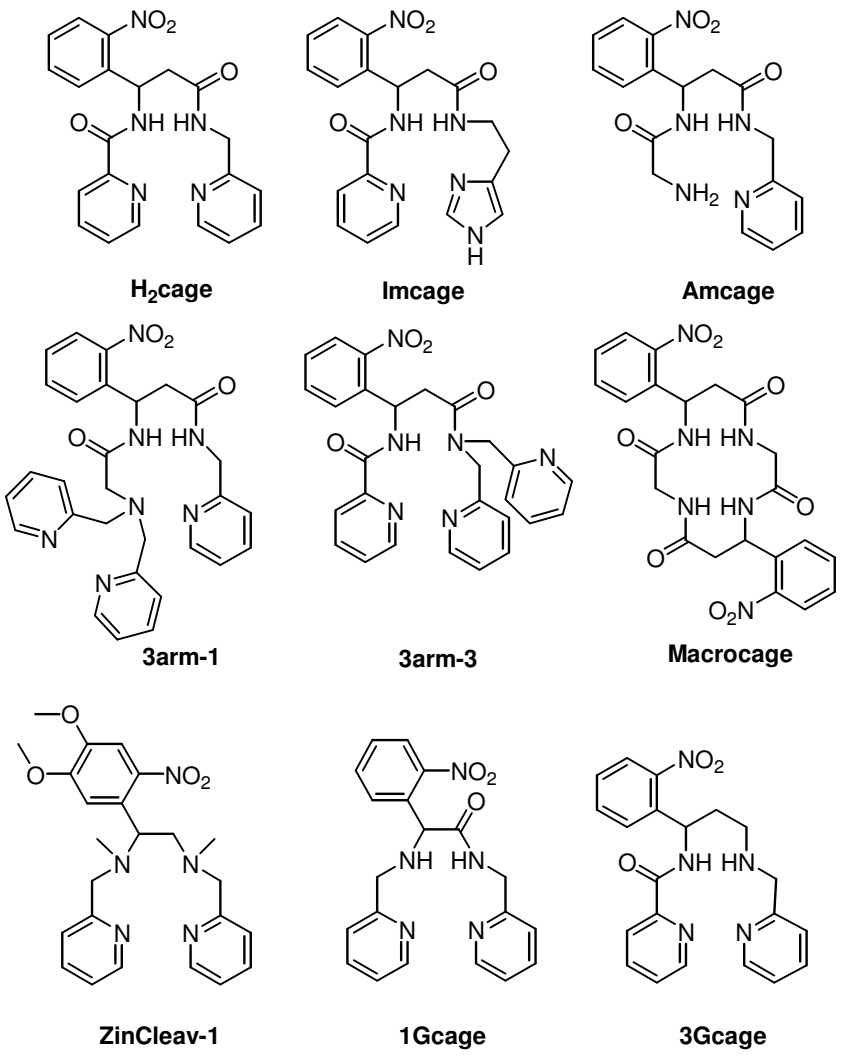

Figure 45: H_2cage and Derivatives

Scheme 16: Synthesis and Photolysis of [Cu(3Gcage)]$^{+}$

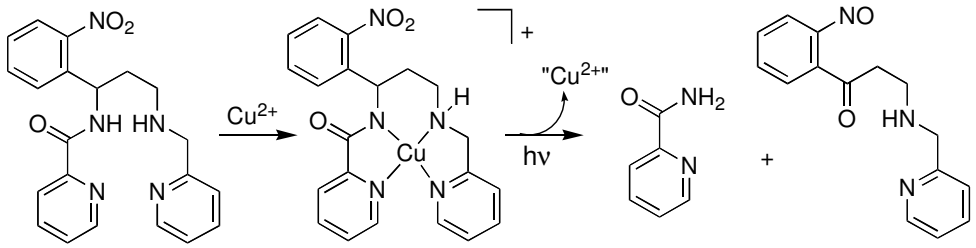

3Gcage **[Cu(3Gcage)]$^{+}$** **pic** **nitroso**

5.2 Materials and Methods

5.2.1 Materials and Instrumentation

Unless otherwise noted, chemicals were purchased commercially and used without further purification. ZinCleav-1 was kindly provided by S. Burdette.[36] All reactions were carried out in the dark and glassware was covered with foil. The ligand H_2cage[26] was synthesized and purified as described previously. Spectra for ^{1}H NMR were collected on a Varian Inova 400 spectrometer with chemical shifts reported in ppm and J values in Hz. High-resolution, fast-atom bombardment (HR-FABMS) mass spectra were recorded on JEOL JMS-SX-102 instrument. Liquid chromatography/mass spectrometry (LC/MS) was performed on an Agilent 1100 Series apparatus with an LC/MSD trap and a Daly conversion dynode detector. A Varian Polaris C18 (150 × 1.0 mm) column was used and peaks were detected by UV absorption at 280 nm. A linear gradient from 10% A in B to 60% A in B was run from 2 to 32 min with a total run time of 42 min, where A is MeCN / 4% 10 mM pH 7 ammonium acetate buffer and B is 10 mM pH 7 ammonium acetate buffer / 2% MeCN. UV-vis spectra were recorded on either a Cary 50 UV-vis spectrophotometer or an SI Photonics (Tucson, AZ) model 420 fiber optic CCD array UV-vis spectrophotometer in a 1-cm pathlength quartz cell. Photolysis experiments were performed using a screwtop quartz cuvette illuminated in a Rayonet RPR-100 Photochemical Reactor containing 16 bulbs, each 3500 Å. Reaction mixtures were purified by preparative reverse-phase HPLC on a YMC C18 column (250 × 200 mm I.D.) with a linear 40-min gradient from 7–70% acetonitrile in water.

5.2.2 Synthesis

Scheme 17: Amcage synthesis

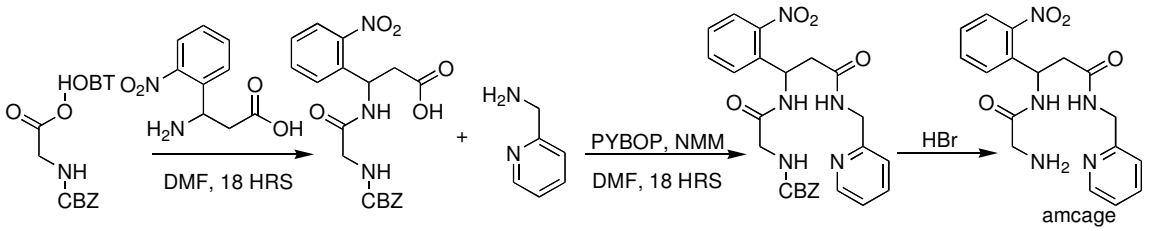

5.2.2.1 3-(2-Amino-acetylamino)-3-(2-nitro-phenyl)-N-pyridin-2-ylmethyl-propionamide (Amcage)

Carbobenzyloxyglycine (0.400 g, 1.912 mmol) and NMM (0.420 mL, 3.824 mmol) in CH_2Cl_2 (6 mL) were added to a 150-mL round-bottom flask equipped with a stir bar. Then PYBOP (0.996 g, 1.912 mmol) in CH_2Cl_2 (4 mL) was added and the reaction mixture was allowed to stir for 18 h at room temperature. After 18h, one equivalent of 3-amino-3-(2-nitrophenyl)propionic acid (0.400 g, 1.912 mmol) dissolved in hot DMF (30 mL) was added and the reaction mixture was stirred for an additional 18 h. NMM (0.420 mL, 3.824 mmol) and 2-(aminomethyl)pyridine (0.196 mL, 1.912 mmol), both in CH_2Cl_2 (6 mL) were added to the reaction mixture. PYBOP (0.996 g, 1.912 mmol) in CH_2Cl_2 (4 mL) was then added, and the reaction mixture stirred for 18 h at room temperature. The solvent was removed and the resulting oil was taken up in CH_2Cl_2 (25 mL), filtered, and washed with 1N HCl (3×10 mL). The aqueous layer was then adjusted to pH 12 and washed with CH_2Cl_2 (4×10 mL). The organic layers were combined, dried over $MgSO_4$, filtered, and solvent removal gave an oil that was purified

by preparative reverse-phase HPLC on a YMC C18 column (250 × 200 mm I.D.) with a linear 40-min gradient from 7–70% acetonitrile in water, to give a white solid after solvent evaporation. The white solid was then dissolved in CH_2Cl_2 (15 mL) and hydrobromic acid ($\geq$ 33% in glacial acetic acid) (15 mL) was added and the reaction mixture was allowed to stir for 2 h at room temperature. After 2 h, the reaction mixture was washed with H_2O (4 × 10 mL). The aqueous layer was then adjusted to pH 12 and washed with CH_2Cl_2 (4 × 10 mL). The organic layers were combined, dried over $MgSO_4$, filtered, and solvent removal gave a white solid (0.2164 g, 31.7 %). ^{1}H NMR ($(CD_3)_2CO$): δ 8.45 (1H, d, J = 3.97), 7.97 (1H, d, *J* = 8.02), 7.72 (1H, d, *J* = 7.62), 7.64 (2H, m), 7.53 (1H, t, *J* = 7.62, *J* = 7.62), 7.21 (1H, d, *J* = 7.64), 5.91 (1H, t, *J* = 5.37, *J* = 5.37), 4.43 (2H, dd, *J* = 15.98, *J* = 40.76), 3.74 (2H, m), 3.06 (1H, dd, *J* = 6.62, *J* = 14.52), 2.94 (1H, dd, *J* = 4.79, *J* = 14.76). ^{13}C NMR ($(CD_3)_2CO$): δ 169.86, 169.75, 158.24, 148.83, 148.59, 137.67, 136.41, 133.29, 129.20, 128.18, 124.31, 121.90, 120.97, 54.00, 46.47, 44.25, 39.94; LC-MS: m/z 358.1 $[M+H]^+$, M = $C_{17}H_{19}N_5O_4$.

Scheme 18: Imcage Synthesis

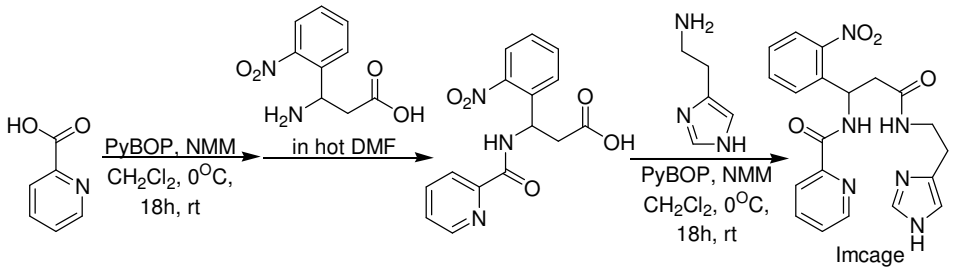

5.2.2.2 2-Methyleneamino-but-2-enoic acid [2-[2-(1H-imidazol-4-yl)-ethylcarbamoyl]-1-(2-nitro-phenyl)-ethyl]-amide (Imcage)

Equimolar quantities of picolinic acid (0.100 g, 0.813 mmol) and NMM (N-methylmorpholine) (0.089 mL, 0.813 mmol) in CH_2Cl_2 (3 mL) were added to a 50-mL round-bottom flask equipped with a stir bar. Then PyBOP (benzotriazol-1-yl-oxytripyrrolidinophosphonium hexafluorophosphate) (0.423 g, 0.813 mmol) in CH_2Cl_2 (2 mL) was added and the reaction mixture was allowed to stir for 18 h at room temperature. After 18 h, one equivalent of 3-amino-3-(2-nitrophenyl)propionic acid (0.171 g, 0.813 mmol) dissolved in hot DMF (15 mL) was added and the reaction mixture was stirred for an additional 18 h. NMM (0.089 mL, 0.813 mmol) and histamine (0.091 g, 0.815 mmol), both in CH_2Cl_2 (3 mL) were added to the reaction mixture. PyBOP (0.423 g, 0.815 mmol) in CH_2Cl_2 (2 mL) was then added, and the reaction mixture stirred for 18 h at room temperature. The solvent was removed and the resulting oil was purified by HPLC, giving a yellow oil (0.053 g, 16%). ^{1}H NMR ($(CD_3)_2CO$): δ 9.86 (1H, d, J = 7.49), 8.73 (1H, s), 8.67 (1H, d, J = 4.33), 8.00 (1H, d, J = 7.58), 7.95 (2H, d, J = 7.42), 7.78 (1H, d, J = 7.86), 7.65 (1H, t, J = 7.60, J = 7.60), 7.57 (1H, m), 7.50 (1H, t, J = 7.74, J = 7.74),

7.32 (1H, s), 5.96 (1H, m), 3.52 (2H, t, J = 6.41, J = 6.41), 3.06 (1H, dd, J = 6.88, J = 14.87), 2.93 (3H, m). ^{13}C NMR ($(CD_3)_2CO$): δ: 170.40, 163.59, 149.82, 148.62, 137.55, 137.47, 133.58, 133.43, 131.78, 128.93, 128.43, 126.62, 124.35, 121.97, 116.36, 46.89, 39.89, 37.99, 24.52; LC-MS: 409.2 m/z $[M+H]^+$, M = $C_{20}H_{20}N_6O_4$.

Scheme 19: Macrocage Synthesis

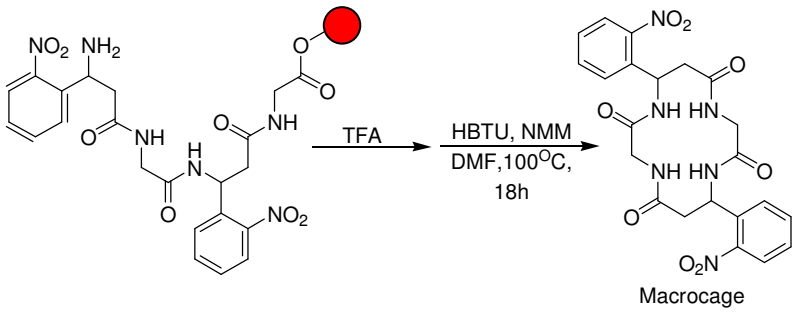

5.2.2.3 7,14-Bis-(2-nitro-phenyl)-1,4,8,11tetraaza-cyclotetradecane-2,5,9,12-tetraone (Macrocage)

Macrocage was synthesized on a Protein Technologies PS3 automated peptide synthesizer using Fmoc-Gly-Wang resin (Advanced ChemTech) (0.048 g, 0.033 mmol). Fmoc was removed using 20% piperdine in DMF. Couplings of Fmoc-3-amino-3-(2-nitrophenyl)propionic acid (0.028 g, 0.066 mmol) and Fmoc-Gly (0.029 g, 0.099 mmol) were carried out using O-benzotriazole-N,N,N',N'-tetramethyl-uronium-hexafluoro-phosphate (HBTU) (0.038 g, 0.099 mmol) and NMM (5 mL, 0.045 mmol) in DMF (10 mL) for 30 min. The uncyclized peptide was obtained by treating the resin-bound molecule with a 95% trifluoroacetic acid (TFA) solution for 2 hours. TFA was removed and the resulting oil was washed (3 × 5 mL) with diethyl ether. The resulting oil and

NMM (5 mL, 0.045 mmol) in DMF (200 mL) were added to a 500-mL round-bottom flask equipped with a stir bar. Then HBTU (0.038 g, 0.099 mmol) in DMF (5 mL) was added and the reaction mixture was allowed to stir for 18 h at 100 ^{o}C. Solvent removal gave an oil that was purified by HPLC, giving a white solid (0.003 g, 16.4%). Analysis by LC-MS and HR-FAB showed > 98% purity. HR-FAB: m/z 499.1578 $[M+H]^+$; exact composition: $C_{22}H_{23}N_6O_8$ $[M+H]^+$.

Scheme 20: 3arm-3 Synthesis

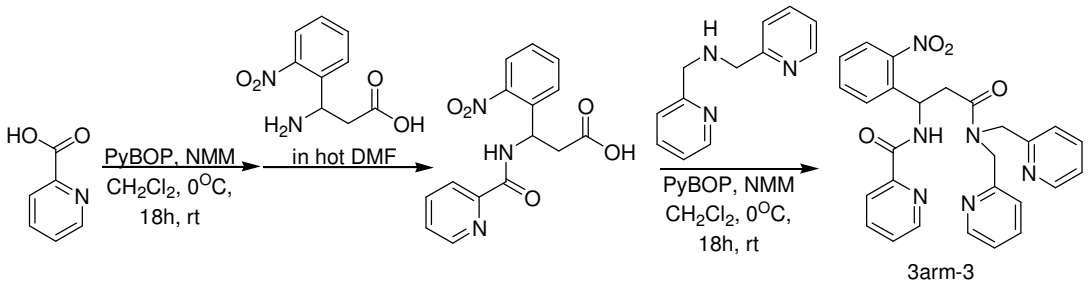

5.2.2.4 Pyridine-2-carboxylic acid [2-(bis-pyridin-2-ylmethyl-carbamoyl)-1-(2-nitro-phenyl)-ethyl]-amide (3arm-3)

Equimolar quantities of picolinic acid (0.010 g, 0.081 mmol) and NMM (0.009 mL, 0.081 mmol) in CH_2Cl_2 (3 mL) were added to a 50-mL round-bottom flask equipped with a stir bar. Then PyBOP (0.042 g, 0.0813 mmol) in CH_2Cl_2 (2 mL) was added and the reaction mixture was allowed to stir for 18 h at room temperature. After 18 h, one equivalent of 3-amino-3-(2-nitrophenyl)propionic acid (0.017 g, 0.081 mmol) dissolved in hot DMF (15 mL) was added and the reaction mixture was stirred for an additional 18 h. NMM (0.089 mL, 0.813 mmol) and di-(2-picolyl)amine (0.015 mL, 0.081 mmol),

both in CH_2Cl_2 (3 mL) were added to the reaction mixture. PyBOP (0.042 g, 0.081 mmol) in CH_2Cl_2 (2 mL) was then added, and the reaction mixture stirred for 18 h at room temperature. The solvent was removed and resulting oil was purified by HPLC, giving a yellow oil (0.036 g, 44%). ^{1}H NMR (CD_3OD): δ 8.76 (dd, *J* = 10.9, *J* = 5.2, 2H), 8.66 (d, *J* = 4.5, 1H), 8.37 (dd, *J* = 11.1, *J* = 4.6, 1H), 8.07 - 7.88 (m, 5H), 7.81 (dd, *J* = 13.8, *J* = 7.3 , 1H), 7.62 - 7.53 (m, 5H), 7.53 - 7.47 (m, 1H), 5.92 (dd, *J* = 7.8, *J* = 4.5, 1H), 5.17 (dd, *J* = 55.6, *J* = 18.2, 2H), 5.06 - 4.96 (m, 2H), 3.39 - 3.36 (m, 1H), 3.14 - 3.08 (m, 1H). ^{13}C NMR (CD_3OD): δ 172.33, 164.49, 155.59, 154.92, 148.41, 147.69, 145.05, 141.74, 139.79, 137.57, 136.48, 133.32, 128.61, 128.43, 126.74, 125.61, 124.87, 124.47, 123.86, 123.02, 121.87, 53.23, 51.14, 37.34; LC-MS: 497.1 m/z $[M+H]^+$, M = $C_{27}H_{24}N_6O_4$.

Scheme 21: 3arm-1 Synthesis

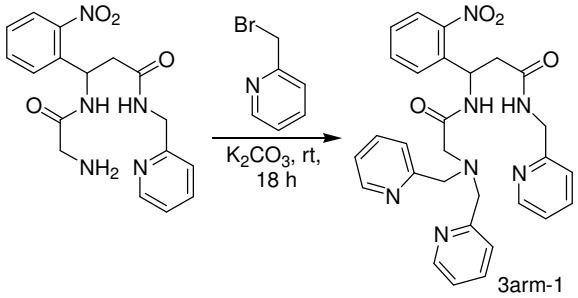

5.2.2.5 3-[2-(Bis-pyridin-2-ylmethyl-amino)-acetylamino]-3-(2-nitro-phenyl)-N-pyridin-2-ylmethyl-propionamide (3arm-1)

Amcage (0.029 g, 0.081 mmol), bromoacetic acid (0.013 mL, 0.178 mmol) and K_2CO_3 (0.045 g, 0.324 mmol) in DMF (10 mL) were combined in a 50-mL round-bottom

flask equipped with a stir bar and the reaction mixture was allowed to stir for 18 h at room temperature. The solvent was removed and the resulting oil was taken up in CH_2Cl_2 (20 mL) and washed with H_2O (4 × 10 mL). The organic layers were combined, the solvent was removed and the resulting oil was purified by HPLC, giving a yellow oil (0.022 g, 49.6 %). Analysis by LC-MS and ^{1}H NMR showed ≥ 98% purity. ^{1}H NMR ((CD$_3$OD): δ 8.76 - 8.71 (m, 3H), 8.67 - 8.65 (m, 1H), 8.59 - 8.54 (m, 1H), 8.26 - 8.22 (m, 1H), 8.18 (td, *J* = 7.8, *J*= 1.6, 2H), 8.12 - 8.07 (m, 1H), 8.02 (d, *J* = 8.0, 1H), 7.95 (dd, *J* = 9.0, *J* = 7.7, 2H), 7.73 - 7.60 (m, 8H), 7.53 (ddd, *J* = 15.5, *J* = 7.1, *J* = 1.4, 2H), 5.82 (t, *J* = 6.8, 1H), 5.03 (s, 2H), 4.60 (d, *J* = 5.9, 2H), 4.27 (s, 2H), 3.60 (d, *J* = 7.3, 2H), 2.96 (d, *J* = 6.9, 2H). LC-MS: 540.1 m/z $[M+H]^+$, M = $C_{29}H_{29}N_7O_4$. Analysis by LC-MS and ^{1}H NMR showed > 98% purity. HR-FAB: m/z 540.2355 $[M+H]^+$; exact composition: $C_{29}H_{30}N_7O_4$ $[M+H]^+$.

Scheme 22: 3Gcage Synthesis

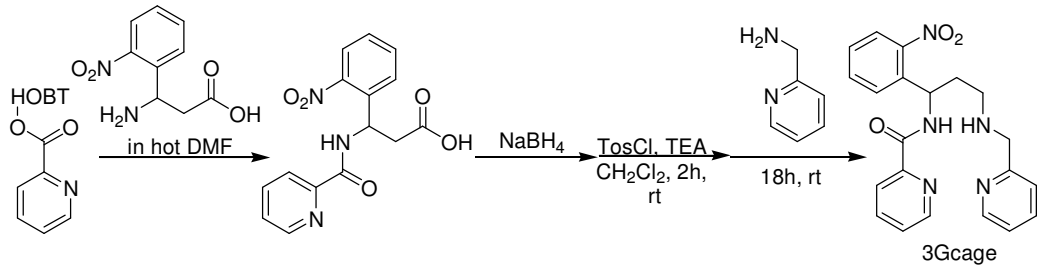

5.2.2.6 Pyridine-2-carboxylic acid {1-(2-nitro-phenyl)-3-[(pyridin-2-ylmethyl)-amino]-propyl}-amide (3Gcage)

Equimolar quantities of picolinic acid (0.05 g, 0.40 mmol) and NMM (0.04 mL,

0.40 mmol) in CH_2Cl_2 (2 mL) were added to a 25-mL round-bottom flask equipped with a stir bar. The reaction mixture was cooled over an ice bath for ten min then PyBOP (0.21 g, 0.40 mmol) in CH_2Cl_2 (2 mL) was added. The reaction mixture was allowed to warm to room temperature with stirring for 18 h. After 18 h, one equivalent of 3-amino-3-(2-nitrophenyl)propionic acid (0.08 g, 0.40 mmol) dissolved in hot DMF (5 mL) was added and the reaction mixture was stirred for an additional 18 h. NMM (0.04 mL, 0.40 mmol) and PyBOP (0.21 g, 0.40 mmol), both in CH_2Cl_2 (2 mL) were added to the reaction mixture. The resulting solution was cooled over an ice bath for ten min then the reaction mixture stirred for 18 h at room temperature. The reaction mixture was again cooled over an ice bath for 30 min then $NaBH_4$ (1.51 g, 4.0 mmol) was added. The reaction mixture was allowed to warm to room temperature and continued stirring for 10 min. The solvent was removed and the resulting oil was taken up in CH_2Cl_2 (15 mL) and washed with saturated sodium bicarbonate (3 × 10 mL). The organic layers were combined, dried over $MgSO_4$, filtered, and solvent removal gave a yellow oil. To the resulting oil equimolar quantities of p-toluenesulfonyl chloride (0.076 g, 0.40 mmol) and triethylamine (0.056 mL, 0.40 mmol) in CH_2Cl_2 (2 mL) were added with stirring for 2 h. After 2 h, 2-(aminomethyl)pyridine (0.04 mL, 0.40 mmol) was added and reaction mixture stirred for 18 h at room temperature. The solvent was removed and the resulting oil was taken up in CH_2Cl_2 (15 mL) and washed with 1N HCl (3 × 5 mL). 1 N NaOH (20 mL) was added to the aqueous layer and washed with CH_2Cl_2 (4 × 10 mL). The organic layers were combined, dried over $MgSO_4$, filtered, and solvent removal gave an oil that was purified

by HPLC, giving a white solid (0.04 g, 25 %). Analysis by LC-MS and HR-FAB showed > 98% purity. HR-FAB: m/z 392.1726 $[M+H]^+$; exact composition: $C_{21}H_{22}N_5O_3$ $[M+H]^+$.

Scheme 23: 1Gcage Synthesis

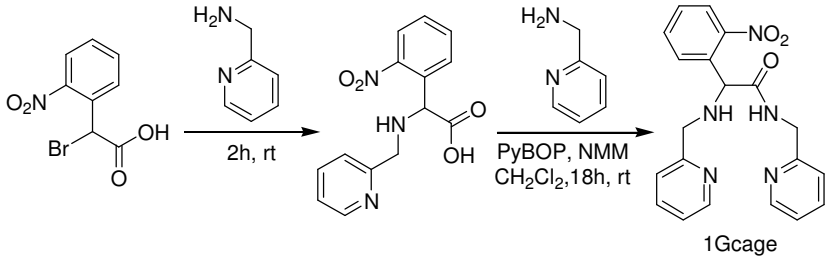

5.2.2.7 2-(2-Nitro-phenyl)-N-pyridin-2-ylmethyl-2-[(pyridin-2-ylmethyl)-amino]-acetamide (1Gcage)

2-bromo-2-(2-nitrophenyl)acetic acid (BNPA) was synthesized using a procedure from Bayley et al.[160] Equimolar quantities of BNPA (0.100 g, 0.385 mmol) and 2-(aminomethyl)pyridine (0.04 mL, 0.385 mmol) in CH_2Cl_2 (3 mL) were added to a 50-mL round-bottom flask equipped with a stir bar and the reaction mixture was allowed to stir for 2 h at room temperature. After 2 h, NMM (0.085 mL, 0.770 mmol) and 2-(aminomethyl)pyridine (0.04 mL, 0.385 mmol), both in CH_2Cl_2 (6 mL) were added to the reaction mixture. PYBOP (0.200 g, 0.385 mmol) in CH_2Cl_2 (4 mL) was then added, and the reaction mixture stirred for 18 h at room temperature. The solvent was removed and the resulting oil was taken up in CH_2Cl_2 (25 mL), filtered, and washed with saturated aqueous NaCl solution (3 × 10 mL). The organic layers were combined, dried over $MgSO_4$, filtered, and solvent removal gave an oil that was purified by chromatography

(silica, EtOAc:hexanes, 3:1 with 1% triethylamine, Rf = 0.30), giving a white crystalline solid (0.06 g, 42%). ^{1}H NMR (CD_3OD): δ 8.51 (1H, m), 8.45 (1H, m), 7.96 (1H, dd, *J* = 1.27, *J* = 8.16), 7.58 (4H, m), 7.42 (1H, ddd, *J* = 1.68, *J* = 7.26, *J* = 8.20), 7.33 (1H, d, *J* = 7.83), 7.26 (1H, d, *J* = 7.85), 7.14 (2H, m), 4.72 (1H, s), 4.58 (2H, dq, *J* = 5.45, *J* = 15.95, *J* = 15.97, *J* = 15.97), 3.92 (2H, q, *J* = 14.01). ^{13}C NMR: δ 170.67, 158.63, 156.89, 149.18, 149.03, 148.88, 136.78, 136.64, 133.83, 133.43, 132.02, 128.79, 125.31, 122.36, 122.30, 122.25, 122.00, 63.54, 53.27, 44.67; LC-MS: 378.1 m/z $[M+H]^+$, M = $C_{20}H_{19}N_5O_3$.

5.2.3 Quantum Yield of Photolysis

The quantum yields of photolysis for 3Gcage and its Cu(II) complex were determined by comparison to the quantum yield of 1-(o-nitrophenyl)ethyl phosphate (caged Pi) as previously reported by Ellis-Davis and Kaplan.[99] Samples of 3Gcage (500 μM) with and without one equivalent of $CuClO_4$, or caged Pi (1 mM) in NaH_2PO_4 buffered to pH 7.4 were irradiated in a Rayonet RPR-100 Photochemical Reactor at 350 nm for 15 s. Photodegradation of the caged compounds was monitored by LC-MS analysis. Aliquots of 3.0 μL of each sample before and after photolysis were injected by autoinjector and run in triplicate. The experiment was repeated to ensure reproducibility. The quantum yield for each sample (Φsample) was calculated by using the following equation (Equation 11):

$$\Phi_{sample} = \Phi_{cp} \times \frac{\%\Delta sample}{\%\Delta cp} \times \frac{A_{350}cp}{A_{350}sample} \quad (11)$$

where Φcp is 0.54, the reference quantum yield of photolysis for caged Pi, %Δsample and %Δcp are the percent change in integrated peak area after photolysis for the sample and caged Pi, respectively, and A_{350} is the absorbance at 350 nm in a 1-mm cuvette for caged Pi (cp) and for the sample.

5.2.4 Deoxyribose Assay

The 2-deoxyribose assay was used to measure hydroxyl radical formation.[98] A mixture of copper, ascorbic acid, and hydrogen peroxide generates hydroxyl radicals by Fenton-like chemistry. Hydroxyl radicals attack 2-deoxyribose to form malondialdehyde (MDA), which upon heating with TBA under acidic conditions produces a pink chromophore. Chelators that prevent copper from reacting with ascorbic acid and hydrogen peroxide result in less chromophore formation. Assays were performed in a 96-well plate using 20 mM NaH_2PO_4 buffered to pH 7.4. The following reagents were added sequentially to obtain a 100 μL buffered solution with these final concentrations: chelator (10 μM), $CuSO_4$ (10 μM), 2-deoxyribose (15 mM), H_2O_2 (100 μM), and ascorbic acid (2 mM). For photolyzed samples, 100 μM solutions of $[Cu(OH_2)(cage)]$ or $[Cu(3Gcage)]^+$ in 20 mM pH 7.4 NaH_2PO_4 buffer were photolyzed in screwtop quartz cuvettes for 4 min in the photoreactor, then immediately diluted into the deoxyribose reaction mixtures to

obtain final concentrations of 10 μM in Cu. Stock solutions of $CuSO_4$, ascorbic acid, and H_2O_2 were prepared fresh daily, other solutions were prepared weekly. The reaction mixtures were shaken in a plate reader at 37 °C for 1 h, then 100 μL of TBA (1 % w/v in 50 mM NaOH) and 100 μL of TCA (trichloroacetic acid) (2.8 % w/v in water) were added. The 96-well plate was placed over a 100 °C water bath for 20 min, then cooled to room temperature and the absorbance at 490 nm was recorded. Values are reported as A/A_0 where A_0 is the absorbance without chelator present and A is the absorbance with chelator added. The value for $CuSO_4$ alone is $A/A_0 = 1$. Error bars represent standard deviations from measurements done in at least triplicate.

5.2.5 General Spectroscopic Methods for Determining Apparent Binding Constants

Solutions were prepared in 10 mM HEPES (N-(2-hydroxyethyl)-piperazine-N'-2-ethanesulfonic acid) buffered to either pH 7 or 7.4. The reaction vessel was a 3-mL quartz cuvette and initial solution volumes were 1 mL. All titrations were carried out at 25 ^{o}C. Aliquots were pipetted into the reaction mixture and monitored spectrophotometrically. After each addition, solutions were manually mixed and equilibrated for 10 min before data were collected. Titrations were repeated in at least triplicate to ensure reproducibility. Association constants of copper or zinc ion with Cage compounds (Cage) were calculated assuming 1:1 binding of Cage and metal, M, in the presence of a competitive chelator, L.

The apparent Cu^{2+} and Zn^{2+} binding constants of Cage compounds were determined from competition experiments between each Cage ligand and a ligand (L) of known affinity for either Cu^{2+} or Zn^{2+} at a selected pH. The equilibrium expressions for the chelation of M by either Cage or L, shown in Equations 12 and 13 give rise to the formation constants for each ligand (Equation 14 and Equation 15). An equilibrium constant for the exchange reaction (K_{ex}, Equation 16) of metal between Cage and L can be calculated based on the known concentrations of total M, Cage, and L added to solution and from the concentration of metal cage complex, [M(Cage)], and competitive ligand metal complex, [M(L)], determined from the absorbance spectra. The apparent binding constant is then obtained by solving eq. 17 for $K'_{[M(Cage)]}$, where $K'_{[M(L)n]}$ is the known conditional binding constant of L at the selected pH.

$$M + L \leftrightarrows [M(L)_n] \tag{12}$$

$$M + Cage \leftrightarrows [M(Cage)] \tag{13}$$

$$K_{[M(L)n]} = \frac{[M(L)_n]}{[M][L]^n} \tag{14}$$

$$K_{[M(Cage)]} = \frac{[M(Cage)]}{[M][Cage]} \tag{15}$$

$$[M(Cage)] + nL \leftrightarrows [M(L)_n] + Cage \tag{16}$$

$$K_{ex} = \frac{[M(L)_n][Cage]}{[L]^n\,[M(Cage)]} = \frac{K'_{[M(L)n]}}{K'_{[M(Cage)]}} \tag{17}$$

5.2.6 Competition Study of Nitrilotriacetic Acid (NTA) vs. Caged Compounds for Cu^{2+}

Kathryn Haas, a graduate student in the Franz laboratory, performed the NTA competition study described below for all cage analogs except 3arm-1 and 3Gcage. Titrations to determine the apparent Cage copper affinity, $K'_{[Cu(Cage)]}$, were performed with NTA ($\log K_{[Cu(NTA)]} = 10.68$ at pH 7.4) as a competitive chelator for Cu^{2+}. Solutions of 0.5-1 mM [Cu(Cage)] were titrated with at least two equivalents of NTA using a 100 mM NTA stock solution.

5.2.7 Competition Study of Ethylenediaminetetraacetic Acid (EDTA) vs. 3Gcage for Cu^{2+}

Solutions of $[Cu(3Gcage)]^+$ with an initial concentration of 0.2 mM were prepared in 10 mM HEPES buffered to pH 7.4. Aliquots of 4 μL of the competitive chelator EDTA (5 mM) were pipetted into $[Cu(3Gcage)]^+$ solutions and monitored spectrophotometrically. The apparent copper binding affinity for 3Gcage, $K'_{[Cu(3Gcage)]}$, was calculated using Equations 12–17 and a $\log K'_{[Cu(EDTA)]} = 15.81$ at pH 7.40.

5.2.8 Competition Study of 4-(2-pyridylazo)resorcinol (PAR) vs. Cage for Zn^{2+}

The Zn^{2+} apparent binding constants of Cage ligands was determined by competition with PAR.[36] All titrations were performed in 10 mM HEPES at pH 7. The spectrum of PAR was recorded as the background. Upon the addition of Zn^{2+} a new

peaks forms at 500 nm due to the formation of the [$Zn(PAR)_2$] complex. To ensure that the 2:1 PAR:Zn^{2+} complex is formed over the 1:1 complex an excess (>20 equivalents) of PAR was used. Cage ligands were then titrated into solution and the absorbance spectra were recorded after each addition. The apparent binding constant was obtained by solving Equation 17 for $K'_{[Zn(Cage)]}$ where $\log K_{[Zn(PAR)2]} = 12.34$.

5.3 Results

5.3.1 Binding Studies

Out of the derivatives synthesized only 3Gcage ($K_d' = 0.18 \pm 0.03$ fM) binds Cu^{2+} more tightly than H_2cage at physiological pH. As shown in Table 8, binding constants were only calculated for ligands that could at least compete with NTA for Cu^{2+}, which at pH 7.4 has a K_d of 23 pM. A typical titration is shown in Figure 46.

Cage analogs were also screened for their ability to coordinate Zn^{2+} and apparent binding constants were calculated (Table 8) using PAR as a competitive chelator. 3arm-1 has the highest binding affinity among the analogs with a K_d' of 0.92 ± 0.16 nM.

Table 8: Apparent Binding Constants and Photolysis Quantum Yields for H_2cage Analogs

Apparent binding constants (K_d') for Cu^{2+} and Zn^{2+} and photolysis quantum yields for apo ligands (Φ_{cage}) and their metal complexes ($\Phi_{[M(cage)]}$) of H_2cage analogs, where M = Cu^{2+} for H_2cage and 3Gcage and M = Zn^{2+} for ZinCleav-1. Values that are not available are labeled "na".

	K_d' for Cu^{2+} at pH 7.4 fM	K_d' for Zn^{2+} at pH 7 nM	Φ_{cage}	$\Phi_{[M(cage)]}$
H_2cage[26]	1.60×10^4	20.93 $\pm$ 1.76	0.73	0.32
Imcage	na	13.69 $\pm$ 1.58	na	na
Amcage	2.00×10^5	21.57 $\pm$ 2.02	na	na
3arm-3	na	12.55 $\pm$ 0.81	na	na
3arm-1	na	0.92 $\pm$ 0.16	na	na
3Gcage	0.18 ± 0.03	na	0.66	0.43
ZinCleav-1[36]	0.05	0.0015	0.024	0.0055

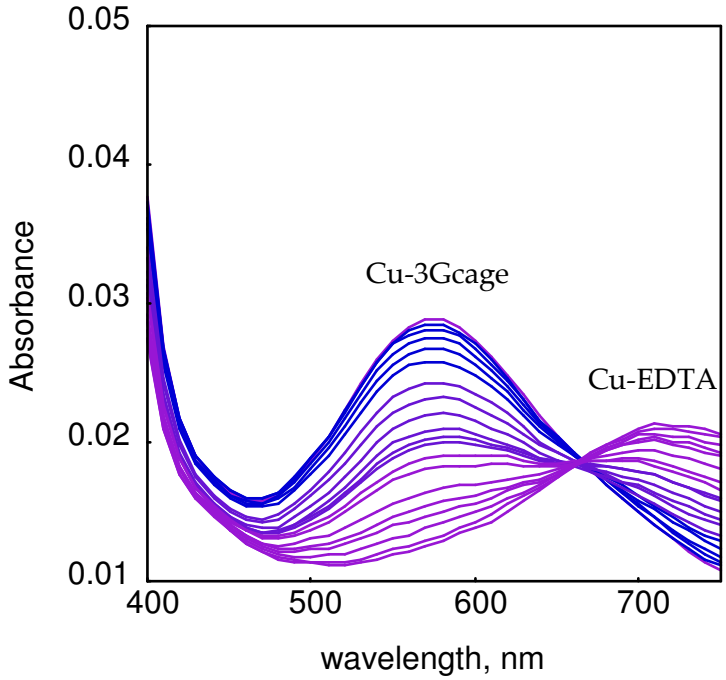

Figure 46: UV Spectra of EDTA Titrated into [Cu(3Gcage)]$^{+}$

Titration of 4 µL aliquots of 5 mM EDTA into 0.200 mM solution of [Cu(3Gcage)]$^{+}$ in HEPES buffer, pH 7.4.

5.3.2 Photolysis of Cage Compounds

Photolysis was only monitored for 3Gcage as it is the only compounds with a Cu^{2+} binding affinity greater than H_2cage at physiological pH.

To analyze the photolysis of our 3rd generation cage a 100 μM $[Cu(3Gcage)]^+$ solution in pH 7.4 phosphate buffer was irradiated with UV light centered at 350 nm. As shown in Figure 47, changes in the UV-vis spectra are apparent within seconds as a shift in the d-d band centered at 570 nm indicates a reorganization of the coordination sphere. Cleavage of the ligand backbone is complete within 3 min, as confirmed by LC-MS analysis (data not shown). The chromatographic peak for the intact Cu complex disappears and is replaced by peaks corresponding to the expected photoproducts and their copper-bound forms, as confirmed by their mass spectra.

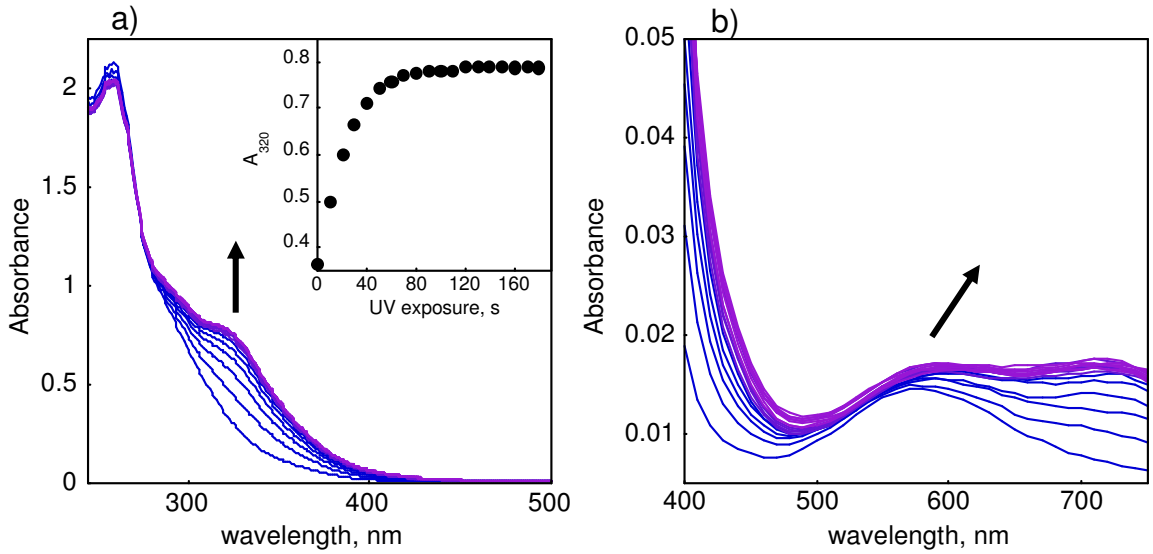

Figure 47: UV-vis Spectra of the Photolysis of [Cu(3Gcage)]$^+$

UV-vis spectra of 100 µM [Cu(3Gcage)]$^+$ irradiated with UV light in 10 second intervals for a total of 180 seconds. a) An increase in absorbance at 320 nm is consistent with the formation of a nitroso photoproduct. Inset: A plot of the absorbance at 320 nm vs. UV exposure indicates that the photolysis of [Cu(3Gcage)]$^+$ is complete in approximately 60 seconds. b) Changes in the d-d band centered at 570 nm indicate a change in the copper coordination sphere upon UV exposure.

5.3.3 Quantum Yield

As shown in Table 8, photolysis efficiency was only calculated for 3Gcage as it is the only compound with a Cu^{2+} binding affinity greater than H_2cage at physiological pH.

Comparison of the integrated peak areas indicated that after 15 s of UV exposure, 43.3% of the caged Pi, 37.9% of 3Gcage, and 43.3% of $[Cu(3Gcage)]^+$ had been photolyzed. The calculated quantum yields of photolysis for 3Gcage and $[Cu(3Gcage)]^+$ are 0.66 and 0.43, respectively.

5.3.4 Effects of [Cu(3Gcage)] in the Deoxyribose Assay

In order to show that photolysis of [Cu(3Gcage)] causes a change in the reactivity of the caged vs. uncaged copper, we monitored the ability of the compounds pre- and post- photolysis to generate $OH^{\bullet}$ radicals by subjecting them to the deoxyribose assay. Hydroxyl radicals, which are generated in this assay by Fenton-like conditions of copper, ascorbic acid, and H_2O_2, degrade deoxyribose to give thiobarbituric acid (TBA)-reactive products with absorbance centered at 532 nm. Values of A/A_0 above 1 indicate the promotion of $OH^{\bullet}$ formation, whereas values below 1 indicate an inhibition of $OH^{\bullet}$ formation.

In order to show that 3Gcage effect the amount of TBA-reactive species by altering the coordination environment around copper, we tested [Cu(3Gcage)] both pre- and post- photolysis (Figure 48). As expected, $[Cu(OH_2)(cage)]$ has an inhibitatory effect on $OH^{\bullet}$ formation, as shown by an A/A_0 value less than 1. The photo-products, on the

other hand, increase the amount of $OH^{\bullet}$ produced.

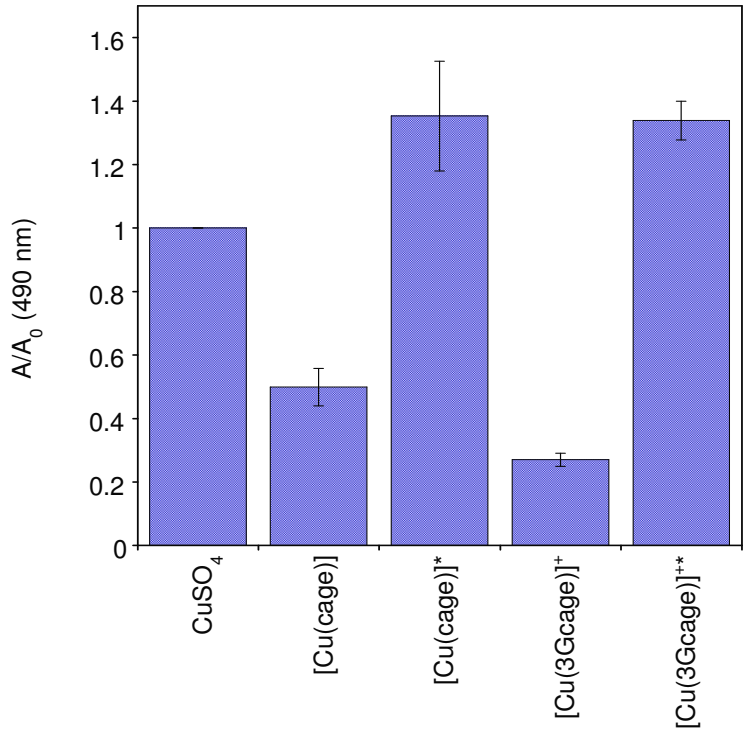

Figure 48: Deoxyribose Assay for $[Cu(3Gcage)]^{+}$

Results of the deoxyribose assay for $OH^{\bullet}$ production, where A and A_0 are the absorbance with and without ligand, so $A/A_0 = 1$ for $CuSO_4$ alone; lower values indicate an inhibitory effect and higher values indicate a promotional effect of the ligand with respect to copper's reactivity for $OH^{\bullet}$ production. Prior to photolysis, $[Cu(3Gcage)]^{+}$ inhibits $OH^{\bullet}$ production better than [Cu(cage)], whereas both compounds promote $OH^{\bullet}$ production at similar levels after 4 min of UV photolysis (indicated by *).

5.4 Discussion

5.4.1 Cu^{2+} Binding Studies

A limitation of H_2cage, our first generation copper cage, is its 16 pM dissociation constant for Cu^{2+} at physiological pH, which is likely not tight enough to keep copper sequestered in the presence of endogenous copper binding proteins. One of the primary goals of the current study was therefore to develop a higher affinity compound while maintaining all of the beneficial properties of H_2cage, like its high quantum efficiency and post-photolysis reactivity. The copper complex of H_2cage, [Cu(OH_2)(cage)], has a distorted trigonal bipyramidal geometry. This distortion in geometry is attributed to a steric interaction between the α hydrogens on the pyridyl rings. We hypothesized that alleviating this steric clash to allow a favorable square planar arrangement might improve the binding affinity for Cu^{2+}. Therefore, one of the pyridyl rings (labeled 1 and 4 in Figure 49) was replaced with either a primary amine to give **Amcage** or an imidazole to give **Imcage**.

To investigate the binding affinity of the cage analogs, a competition experiment was performed between the cage ligand and the common chelator nitrilotriacetic acid (NTA), which at pH 7.4 has a K_d of 23 pM. Since our goal was to identify compounds with better affinity than H_2cage, binding constants were only calculated for ligands that could at least compete with NTA for Cu^{2+}. Imcage falls into the category of ligands unable to compete with NTA for Cu^{2+}. On the other hand, Amcage is able to compete with NTA for copper, but has a Kd of 200 pM that is still weaker than H_2cage.

The lackluster binding of Amcage and Imcage is likely due to both electronic and steric effects. The conversion of nitrogen 1 to a primary amine may alleviate the steric hindrance between the α hydrogens on the pyridyl rings of H_2cage. However, a pyridyl nitrogen is a better electron donor than a primary amine, therefore this conversion may contribute to Amcage's decreased binding affinity as compared to H_2cage. In H_2cage, nitrogens 1 and 2 form a 5 membered ring, 2 and 3 form a 6 membered ring, and 3 and 4 form a 5 membered ring with copper. This 5-6-5 ring system has been shown to favor Cu^{2+} binding.[161,162] Imcage has a 5-6-6 ring system that is less favorable than the 5-6-5 ring system for Cu^{2+} binding.[161,162]

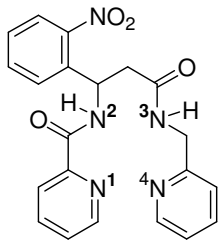

Figure 49: Nitrogen Numbering Scheme for H_2cage

Manipulations of the pyridyl nitrogens to form Imcage and Amcage were found to be unfavorable for Cu^{2+} binding. Since [Cu(OH_2)(cage)] has a water molecule as the fifth donor atom, the incorporation of additional donor atoms to the ligand backbone may be beneficial for copper binding. Therefore, we decided to investigate the effect of

adding additional pyridyl rings to the ligand backbone. A methyl-pyridine was added to nitrogen 3 (Figure 49) to form **3arm-3** and two methyl-pyridines were added to the primary amine on Amcage to give **3arm-1**. In H_2cage, deprotonation of amide 3 is needed to stabilize copper in its tetradentate binding pocket. Substitution at this site occupies the electrons that were once donated to copper. As a result, 3arm-3 is unable to compete with NTA for copper, establishing that substitution at this site is not favorable for copper binding. The incorporation of two methyl-pyridines to Amcage produces a ligand with six donor atoms: three pyridyl nitrogens, two amides, and a tertiary amine. Unfortunately, 3arm-1 was also found to be a weaker copper chelator than NTA. Therefore, we determined that all of the modifications we made to our ring system hinder copper binding more than the steric interaction of the α hydrogens on the pyridyl rings of H_2cage.

Due to the fact that macrocyclic ligands are known to be more stable than their linear counterparts, we synthesized **macrocage** in an attempt at improving the Cu^{2+} binding affinity of the ligand backbone. Macrocage and its copper complex are unfortunately only soluble in DMF; very minimal amounts of water can be added before precipitation occurs. For this reason, competition experiments with NTA were not performed. A similar compound to macrocage that lacks the nitrophenyl groups has been reported by Margerum and coworkers.[163] A pH higher than 13 is needed to form the macrocyclic copper complex, but EPR analysis showed that copper coordinates to four deprotonated amides and is stable down to pH 8. However, at physiological pH this same

coordination is not observed, causing a decrease in binding affinity and a higher probability of ligand exchange reactions. Due to the lack of water solubility and incompatibility with physiological pH, macrocage will not be an affective copper chelator for our purposes.

The most well-known ligands for photocaging metal ions are those used to cage calcium; however, these chelating structures are based on carboxylate-rich binding domains that are not ideal for our system since copper in this coordination environment can act as a pro-oxidant and photolysis releases CO_2 and carbon centered radicals.[97] While there are few examples of photocaged d-metal complexes, Burdette and coworkers recently published **ZinCleav-1** as a photolabile Zn^{2+} chelator.[36] This tetradentate ligand contains two tertiary amines and two pyridyl amines, as shown in Figure 45. We found that ZinCleav-1 binds copper rather tightly since NTA could not compete with ZinCleav-1 for copper. ZinCleav-1 is built on the framework of EBAP (ethylene-bis-α,α'-(2-aminomethyl)pyridine), which has a reported K_d for Cu^{2+} of 3.1 pM.[164] These examples suggest that replacing the amides in H_2cage with amines could improve copper binding. Any improvement in copper binding, however, needs to be evaluated along with other implications these modifications have on other properties of the complex. For example, the copper complex of ZinCleav-1, which only contains neutral donor atoms, has a 2+ charge overall that may limit its ability to diffuse across cell membranes. The photolytic efficiency, as discussed further below, is another important parameter that may be altered by ligand modification.

5.4.2 Zn^{2+} Binding Studies

While most of the cage analogs show feeble binding properties for Cu^{2+}, they were also screened for their ability to coordinate Zn^{2+}. The Zn^{2+} apparent binding constants were measured by titrating solutions of $[Zn(PAR)_2]$, where PAR is 4-(2-pyridylazo)resorcinol, with various cage derivatives. The Zn^{2+} complexes of the cages lack a spectroscopic signal, therefore by monitoring the decrease at 500 nm of the $[Zn(PAR)_2]$ complex upon the addition of the cage chelators, apparent binding constants can be obtained.

Table 8 shows the apparent binding constants calculated using the PAR titration data. While none of our derivates bind zinc as strongly as ZinCleav-1, which has a K_d' of 1.5 pM,[36] 3arm-1 has the highest affinity among the series for Zn^{2+} with a K_d' of 0.92 nM. However, to keep zinc sequestered in a biological system, a binding constant of at least pM is required.[165]

5.4.3 Photochemistry

Ortho-nitrophenyl groups have been used in countless examples for caging biological molecules by covalent modification of a key functional group required for biological activity. The caged molecule is thereby biologically inactive, but exposure to UV light releases the photolabile protecting group to restore biological activity. Like Ca^{2+} cages, our Cu^{2+} cages are designed so that a nitrophenyl group is incorporated into the ligand backbone of a high affinity copper chelator such that bond cleavage induced by

UV light releases bidentate compounds with a low affinity for copper, as shown in Scheme 16. In this case the nitrophenyl group is incorporated to control the spatial and temporal release of the metal cargo.

An important quality of a photolabile group is its quantum efficiency. Because nitrophenyl groups are activated by near-UV light (350 nm), it is important to have high quantum efficiency to keep exposure times short and minimize cellular damage. One way found to improve quantum efficiency in calcium cages is to increase the extinction coefficient at 350 nm by incorporating methoxy substitutes at the four and five position of the ortho-nitrophenyl group.[20] Increasing the photons absorbed at the photolysis wavelength maximizes photolytic efficiency, meaning less light is needed to photolyze an equivalent amount of compound.

Our findings above show that the replacing the amides with amines may be beneficial with respect to Cu(II) affinity. However, a comparison of the quantum efficiencies of H_2cage (0.73 and 0.32 for apo and Cu-bound, respectively) vs. ZinCleav-1 (0.024 and 0.0055 for apo and Zn-bound, respectively) suggests that such an alteration has a negative impact on photolysis efficiency. H_2cage is thirty times more efficient than ZinCleav-1 in the absence of metal, and nearly sixty times more efficient in the metal-bound form, even though ZinCleav-1 has the more favorable dimethoxy-substituted ortho-nitrophenyl group (Figure 45). This difference in efficiency may be due to the fact that the amide at position 2 in H_2cage (see Figure 48) is a better leaving group than the secondary amine of ZinCleav-1. To test this hypothesis, we used 1Gcage, a ligand

similar to H_2cage, but with a primary amine as the leaving group at position 2 instead of an amide. We found that bond cleavage does not occur with 1Gcage even after hours of UV exposure whereas H_2cage is completely photolyzed in 4 min (data not shown). This result further supports our hypothesis that the leaving group plays a major role in the cleavage efficiency of the ligand and indicates that converting both amide nitrogens to amines is not an ideal strategy for improving copper cages.

5.4.4 Design of 3rd Generation Cage

While it seems unfortunate that none of the derivates described above bind copper more tightly than the parent H_2cage at physiological pH, several key results were obtained: replacing one of the pyridyl nitrogens, altering the 5-6-5 chelate ring system, or substituting at nitrogen 3 (Figure 49) are all negative design factors with respect to copper binding. The most significant improvement for Cu^{2+} binding is to replace the amides for amines, but this change dramatically decreases photolysis efficiency. In order to improve copper binding while maintaining photolysis efficiency, we therefore designed the third-generation chelator, **3Gcage**, with an amide as the photolysis leaving group at position 2 and a secondary amine at position 3.

Initial assessment of Cu^{2+} binding by 3Gcage with NTA indicated that NTA was too weak of a competitive inhibitor; therefore, the apparent binding constant was obtained by titration with EDTA. Analysis of the spectral changes shown in Figure 46 as EDTA is titrated into a solution of $[Cu(3Gcage)]^+$ provides a K_d' for 3Gcage of 0.18 ±

0.03 fM at pH 7.4, an improvement over H_2cage's K_d' of 16 pM by more than 4 orders of magnitude. In addition, 3Gcage shows a selectivity for Cu^{2+} over Zn^{2+} as a 10-fold excess of Zn^{2+} cannot displace Cu^{2+} from $[Cu(3Gcage)]^+$.

5.4.5 Efficiency of Photolysis

Figure 47 shows that within seconds of UV exposure the coordination environment around caged copper changes. Cleavage of the ligand backbone is complete within 3 min, as confirmed by LC-MS analysis (data not shown). The quantum yield of photolysis for 3Gcage and its copper complex, 0.66 and 0.43 respectively, is similar to that of H_2cage (0.73) and $[Cu(OH_2)(cage)]$ (0.32). Combined, these results confirm that changing the amide that is not involved in the photolysis mechanism (position 3 in Figure 49) to a secondary amine does not hinder photolysis efficiency but does significantly improve copper binding.

5.4.6 Hydroxyl Radical Formation

In order to assess how the reactivity of $[Cu(3Gcage)]^+$ is affected, we used the deoxyribose assay to monitor the ability of the complex pre- and post-photolysis to generate hydroxyl radicals in the presence of H_2O_2 and a reductant. Fenton-like conditions propagate hydroxyl radical formation when Cu^{2+} is reduced by ascorbic acid and reacts with H_2O_2 to degrade deoxyribose. The degraded deoxyribose then reacts with thiobarbituric acid to afford a pink chromophore that is measured spectrophotometrically.

Ligands added to the reaction mixture that prevent the reduction of Cu^{2+} attenuate the formation of hydroxyl radicals and in turn chromophore formation. As shown in Figure 48, 3Gcage provides 70% protection of hydroxyl radical formation as compared to Cu^{2+} alone. This outcome is an improvement over H_2cage, which only provides 50% protection. The photoproducts of 3Gcage, on the other hand, increase hydroxyl radical formation above the level observed for Cu^{2+} alone. The reactivity of the photoproducts of $[Cu(3Gcage)]^+$ matches that of photolyzed $[Cu(OH_2)(cage)]$, indicating that the bidentate chelators produced post-photolysis improve the catalytic properties of the metal with respect to Fenton-like chemistry.

5.5 Summary and Conclusion

In conclusion, an analysis of seven new analogs of nitrophenyl-containing ligands reveals that 3Gcage is the most promising photoactive ligand for Cu^{2+} to date. 3Gcage coordinates copper in a tetradentate binding site that includes two pyridyl nitrogens, one amide nitrogen, and one amine. The placement of the amide as the leaving group for nitrophenyl photoactivation was found to be a key feature for achieving a high quantum efficiency for photolytic activity. The ability of copper to participate in Fenton-like chemistry and catalyze the production of hydroxyl radicals from H_2O_2 and ascorbic acid was analyzed by using the deoxyribose assay. In the dark, 3Gcage inhibits hydroxyl radical formation, on the other hand, after exposure to UV light hydroxyl radical formation increases by more than 300%. The 0.18 fM copper binding affinity of our 3rd generation chelator is a great improvement from our first-generation H_2cage chelator and should be strong enough to keep copper sequestered in the presence of endogenous copper binding proteins. Our new caged copper complex has a low charge (+1) and a molecular weight less than 500 g/mol, which may be useful for cellular application and cell permeability. This is a promising step toward developing photolabile compounds that can deliver metal ions in a spatial and temporal manner to induce oxidative stress as a chemotherapy strategy or to study metal trafficking pathways. Future work will be aimed at expanding our 3rd generation chelator library as well as investigating the biological application of these compounds.

Appendix A. Mechanism of Photochemical Bond Cleavage

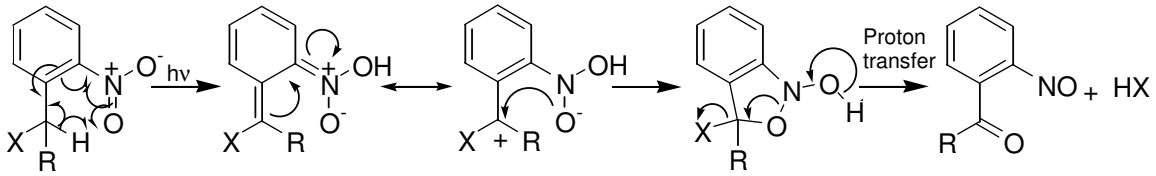

X = leaving group
R = non-leaving group

Appendix B. Suggested Mechanism for the Photolysis of [Pt(cage)]

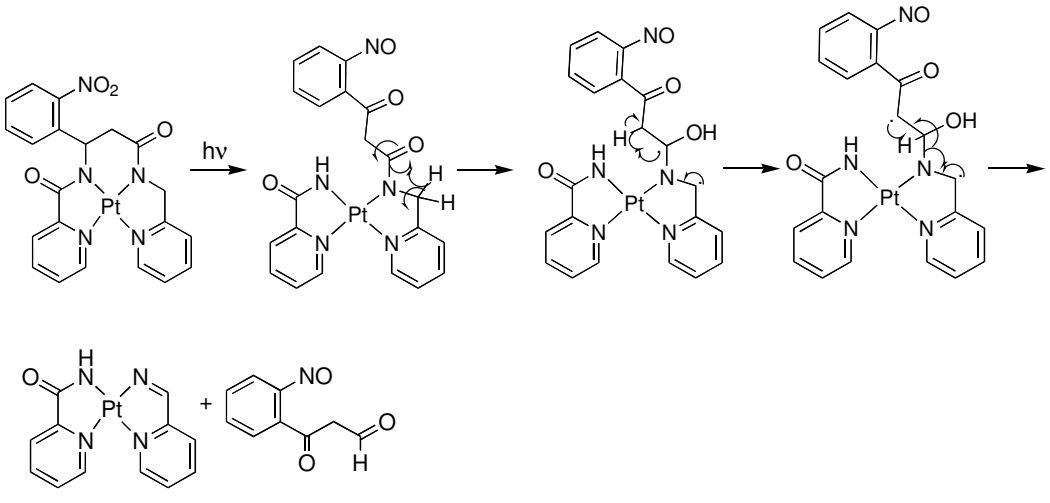

3

References

(1) Kaplan, J. H.; Forbush, B.; Hoffman, J. F. *Biochemistry* **1978**, *17*, 1929-1935.

(2) Deiters, A. *ChemBioChem*, *11*, 47-53.

(3) Lee, H.-M.; Larson, D. R.; Lawrence, D. S. *ACS Chemical Biology* **2009**, *4*, 409-427.

(4) Rothman, D. M.; Shults, M. D.; Imperiali, B. *Trends in Cell Biology* **2005**, *15*, 502-510.

(5) Voloshin, Y. Z.; Kostromina, N. A.; Kramer, R. *Clathrochelates: Synthesis, Structure and Properties*; Elsevier: Amsterdam, 2002.

(6) Buschmann, H. J. *Inorganica Chimica Acta* **1987**, *134*, 225-228.

(7) Kauffmann, E.; Lehn, J. M.; Sauvage, J. P. *Helvetica Chimica Acta* **1976**, *59*, 1099-1111.

(8) Busch, D. H. *Chemical Reviews* **1993**, *93*, 847-860.

(9) Sarkar, B.; Mukhopadhyay, P.; Bharadwaj, P. K. *Coordination Chemistry Reviews* **2003**, *236*, 1-13.

(10) Sargeson, A. M. *Coordination Chemistry Reviews* **1996**, *151*, 89-114.

(11) Voloshin, Y. Z.; Varzatskii, O. A.; Bubnov, Y. N. *Russian Chemical Bulletin* **2007**, *56*, 577-605.

(12) Adams, S. R.; Kao, J. P. Y.; Grynkiewicz, G.; Minta, A.; Tsien, R. Y. *J. Am. Chem. Soc.* **1988**, *110*, 3212-3220.

(13) Kaplan, J. H.; Ellis-Davies, G. C. R. *Proceedings of the National Academy of Sciences of the United States of America* **1988**, *85*, 6571-6575.

(14) Tsien, R. Y.; Zucker, R. S. *Biophysical Journal* **1986**, *50*, 843-853.

(15) Ellis-Davies, G. C. R. *Chem. Rev.* **2008**, *108*, 1603-1613.

(16) Adams, S. R.; Tsien, R. Y. *Ann. Rev. Physiol.* **1993**, *55*, 755-784.

(17) McCray, J. A.; Trentham, D. R. *Annual Review of Biophysics and Biophysical Chemistry* **1989**, *18*, 239-270.

(18) Koch-Paiz, C. A.; Amundson, S. A.; Bittner, M. L.; Meltzer, P. S.; Fornace, A. J. *Mutation Research-Fundamental and Molecular Mechanisms of*

Mutagenesis **2004**, *549*, 65-78.

(19) Kozmin, S.; Slezak, G.; Reynaud-Angelin, A.; Elie, C.; de Rycke, Y.; Boiteux, S.; Sage, E. *Proceedings of the National Academy of Sciences of the United States of America* **2005**, *102*, 13538-13543.

(20) Ellis-Davies, G. C. R.; Barsotti, R. J. *Cell Calcium* **2006**, *39*, 75-83.

(21) Adams, S. R.; Lev-Ram, V.; Tsien, R. Y. *Chem. Biol.* **1997**, *4*, 867-878.

(22) Momotake, A.; Lindegger, N.; Niggli, E.; Barsotti, R. J.; Ellis-Davies, G. C. R. *Nat Meth* **2006**, *3*, 35-40.

(23) Grell, E.; Warmuth, R. *Pure and Applied Chemistry* **1993**, *65*, 373-379.

(24) Kishimoto, T.; Liu, T.-T.; Ninomiya, Y.; Takagi, H.; Yoshioka, T.; Ellis-Davies, G. C. R.; Miyashita, Y.; Kasai, H. *J Physiol* **2001**, *533*, 627-637.

(25) Plaza, P.; Leray, I.; Changenet-Barret, P.; Martin, M. M.; Valeur, B. *ChemPhysChem* **2002**, *3*, 668-674.

(26) Ciesienski, K. L.; Haas, K. L.; Dickens, M. G.; Tesema, Y. T.; Franz, K. J. *Journal of the American Chemical Society* **2008**, *130*, 12246-12247.

(27) Ciesienski, K. L.; Franz, K. J. **2010**, *Manuscript In Preparation*.

(28) Tsien, R. W.; Tsien, R. Y. *Annual Review of Cell Biology* **1990**, *6*, 715-760.

(29) Kikuchi, K.; Komatsu, K.; Nagano, T. *Current Opinion in Chemical Biology* **2004**, *8*, 182-191.

(30) Nolan, E. M.; Lippard, S. J. *Accounts of Chemical Research* **2009**, *42*, 193-203.

(31) Miller, E. W.; Zeng, L.; Domaille, D. W.; Chang, C. J. *Nature Protocols* **2006**, *1*, 824-827.

(32) Yang, L. C.; McRae, R.; Henary, M. M.; Patel, R.; Lai, B.; Vogt, S.; Fahrni, C. J. *Proceedings of the National Academy of Sciences of the United States of America* **2005**, *102*, 11179-11184.

(33) Ciesienski, K. L.; Hyman, L. M.; Derisavifard, S.; Franz, K. J. *Inorg. Chem.* **2010**, *Manuscript Submitted*.

(34) Kennedy, D. P.; Gwizdala, C.; Burdette, S. C. *Organic Letters* **2009**, *11*, 2587-2590.

(35) Gwizdala, C.; Kennedy, D. P.; Burdette, S. C. *Chemical Communications*

2009, 6967-6969.

(36) Bandara, H. M. D.; Kennedy, D. P.; Akin, E.; Incarvito, C. D.; Burdette, S. C. *Inorganic Chemistry* **2009**, *48*, 8445-8455.

(37) Zhang, X.; Chen, Y. *ChemPhysChem* **2009**, *10*, 1993-1995.

(38) Granger, J.; Price, N. M. *Limnology and Oceanography* **1999**, *44*, 541-555.

(39) Trick, C. G. *Current Microbiology* **1989**, *18*, 375-378.

(40) Wilhelm, S. W.; Trick, C. G. *Limnology and Oceanography* **1994**, *39*, 1979-1984.

(41) Barbeau, K.; Rue, E. L.; Bruland, K. W.; Butler, A. *Nature* **2001**, *413*, 409-413.

(42) Martinez, J. S.; Zhang, G. P.; Holt, P. D.; Jung, H. T.; Carrano, C. J.; Haygood, M. G.; Butler, A. *Science* **2000**, *287*, 1245-1247.

(43) Haygood, M. G.; Holt, P. D.; Butler, A. *Limnology and Oceanography* **1993**, *38*, 1091-1097.

(44) Hickford, S. J. H.; Kupper, F. C.; Zhang, G. P.; Carrano, C. J.; Blunt, J. W.; Butler, A. *Journal of Natural Products* **2004**, *67*, 1897-1899.

(45) Ito, Y.; Butler, A. *Limnology and Oceanography* **2005**, *50*, 1918-1923.

(46) Kupper, F. C.; Carrano, C. J.; Kuhn, J. U.; Butler, A. *Inorganic Chemistry* **2006**, *45*, 6028-6033.

(47) Martin, J. D.; Ito, Y.; Homann, V. V.; Haygood, M. G.; Butler, A. *Journal of Biological Inorganic Chemistry* **2006**, *11*, 633-641.

(48) Kennedy, D. P.; Incarvilo, C. D.; Burdette, S. C. *Inorganic Chemistry*, *49*, 916-923.

(49) Rosenberg, B.; Vancamp, L.; Krigas, T. *Nature* **1965**, *205*, 698-699.

(50) Harris, A. L. *Nature Reviews Cancer* **2002**, *2*, 38-47.

(51) Kratochwil, N. A.; Bednarski, P. J.; Mrozek, H.; Vogler, A.; Nagle, J. K. *Anti-Cancer Drug Design* **1996**, *11*, 155-171.

(52) Hall, M. D.; Hambley, T. W. *Coordination Chemistry Reviews* **2002**, *232*, 49-67.

(53) Wong, E.; Giandomenico, C. M. *Chemical Reviews* **1999**, *99*, 2451-2466.

(54) Kratochwil, N. A.; Zabel, M.; Range, K. J.; Bednarski, P. J. *Journal of Medicinal Chemistry* **1996**, *39*, 2499-2507.

(55) Bednarski, P. J.; Mackay, F. S.; Sadler, P. J. *Anti-Cancer Agents in Medicinal Chemistry* **2007**, *7*, 75-93.

(56) Vogler, A.; Kern, A.; Huttermann, J. *Angewandte Chemie-International Edition in English* **1978**, *17*, 524-525.

(57) Muller, P.; Schroder, B.; Parkinson, J. A.; Kratochwil, N. A.; Coxall, R. A.; Parkin, A.; Parsons, S.; Sadler, P. J. *Angewandte Chemie-International Edition* **2003**, *42*, 335-339.

(58) Bednarski, P. J.; Gr¸nert, R.; Zielzki, M.; Wellner, A.; Mackay, F. S.; Sadler, P. J. *Chemistry & Biology* **2006**, *13*, 61-67.

(59) Farrer, N. J.; Woods, J. A.; Munk, V. P.; Mackay, F. S.; Sadler, P. J. *Chemical Research in Toxicology*, *23*, 413-421.

(60) Bierbach, U.; Qu, Y.; Hambley, T. W.; Peroutka, J.; Nguyen, H. L.; Doedee, M.; Farrell, N. *Inorganic Chemistry* **1999**, *38*, 3535-3542.

(61) Leng, M.; Locker, D.; Giraud-Panis, M. J.; Schwartz, A.; Intini, F. P.; Natile, G.; Pisano, C.; Boccarelli, A.; Giordano, D.; Coluccia, M. *Molecular Pharmacology* **2000**, *58*, 1525-1535.

(62) Natile, G.; Coluccia, M. *Coordination Chemistry Reviews* **2001**, *216*, 383-410.

(63) Mackay, F. S.; Woods, J. A.; Moseley, H.; Ferguson, J.; Dawson, A.; Parsons, S.; Sadler, P. J. *Chemistry-a European Journal* **2006**, *12*, 3155-3161.

(64) Mackay, F. S.; Woods, J. A.; Heringova, P.; Kasparkova, J.; Pizarro, A. M.; Moggach, S. A.; Parsons, S.; Brabec, V.; Sadler, P. J. *Proceedings of the National Academy of Sciences of the United States of America* **2007**, *104*, 20743-20748.

(65) Ciesienski, K. L.; Hyman, L. M.; Yang, D. T.; Haas, K. L.; Dickens, M. G.; Holbrook, R. J.; Franz, K. J. *Eur. J. Inorg. Chem.* **2010**, *In Press*.

(66) Barton, J. K.; Lolis, E. *Journal of the American Chemical Society* **1985**, *107*, 708-709.

(67) Grover, N.; Gupta, N.; Thorp, H. H. *Journal of the American Chemical Society* **1992**, *114*, 3390-3393.

(68) Grover, N.; Welch, T. W.; Fairley, T. A.; Cory, M.; Thorp, H. H. *Inorganic Chemistry* **1994**, *33*, 3544-3548.

(69) Zhao, M.; Clarke, M. J. *Journal of Biological Inorganic Chemistry* **1999**,

4, 325-340.

(70) Singh, T. N.; Turro, C. *Inorganic Chemistry* **2004**, *43*, 7260-7262.

(71) Loganathan, D.; Morrison, H. *Current Opinion in Drug Discovery & Development* **2005**, *8*, 478-486.

(72) Menon, E. L.; Perera, R.; Navarro, M.; Kuhn, R. J.; Morrison, H. *Inorganic Chemistry* **2004**, *43*, 5373-5381.

(73) Zayat, L.; Salierno, M.; Etchenique, R. *Inorganic Chemistry* **2006**, *45*, 1728-1731.

(74) Zayat, L.; Calero, C.; Albores, P.; Baraldo, L.; Etchenique, R. *Journal of the American Chemical Society* **2003**, *125*, 882-883.

(75) Zayat, L.; Noval, M. G.; Campi, J.; Calero, C. I.; Calvo, D. J.; Etchenique, R. *ChemBioChem* **2007**, *8*, 2035-2038.

(76) Salierno, M.; Fameli, C.; Etchenique, R. *European Journal of Inorganic Chemistry* **2008**, 1125-1128.

(77) Ignarro, L. J. *Nitric Oxide: Biology and Pathobiology*; Academic Press: San Diego, CA, 2000.

(78) Friederich, J. A.; Butterworth, J. F. *Anesthesia and Analgesia* **1995**, *81*, 152-162.

(79) Napoli, C.; Ignarro, L. J. *Annual Review of Pharmacology and Toxicology* **2003**, *43*, 97-123.

(80) Patra, A. K.; Mascharak, P. K. *Inorganic Chemistry* **2003**, *42*, 7363-7365.

(81) Ghosh, K.; Eroy-Reveles, A. A.; Avila, B.; Holman, T. R.; Olmstead, M. M.; Mascharak, P. K. *Inorganic Chemistry* **2004**, *43*, 2988-2997.

(82) Madhani, M.; Patra, A. K.; Miller, T. W.; Eroy-Reveles, A. A.; Hobbs, A. J.; Fukuto, J. M.; Mascharak, P. K. *Journal of Medicinal Chemistry* **2006**, *49*, 7325-7330.

(83) Wecksler, S. R.; Mikhailovsky, A.; Korystov, D.; Buller, F.; Kannan, R.; Tan, L. S.; Ford, P. C. *Inorganic Chemistry* **2007**, *46*, 395-402.

(84) Wecksler, S. R.; Hutchinson, J.; Ford, P. C. *Inorganic Chemistry* **2006**, *45*, 1192-1200.

(85) Wecksler, S. R.; Mikhailovsky, A.; Korystov, D.; Ford, P. C. *Journal of the American Chemical Society* **2006**, *128*, 3831-3837.

(86) Wecksler, S.; Mikhailovsky, A.; Ford, P. C. *Journal of the American*

Chemical Society **2004**, *126*, 13566-13567.

(87) Rose, M. J.; Mascharak, P. K. *Current Opinion in Chemical Biology* **2008**, *12*, 238-244.

(88) Ryter, S. W.; Alam, J.; Choi, A. M. K. *Physiological Reviews* **2006**, *86*, 583-650.

(89) Niesel, J.; Pinto, A.; N'Dongo, H. W. P.; Merz, K.; Ott, I.; Gust, R.; Schatzschneider, U. *Chemical Communications* **2008**, 1798-1800.

(90) Gaggelli, E.; Kozlowski, H.; Valensin, D.; Valensin, G. *Chem. Rev.* **2006**, *106*, 1995-2044.

(91) Peña, M. M. O.; Lee, J.; Thiele, D. J. *J. Nutrition* **1999**, 1251–1260.

(92) Schlief, M. L.; Gitlin, J. D. *Molecular Neurobiology* **2006**, *33*, 81-90.

(93) Madsen, E.; Gitlin, J. D. *Annual Review of Neuroscience* **2007**, *30*, 317-337.

(94) Farmer, P. J.; Brayton, D.; Moore, C.; Williams, D.; Shahandeh, B.; Cen, D.; Meyskens, F. L. In *Medicinal Inorganic Chemistry*; Sessler, J. L., Doctrow, S. R., McMurry, T. J., Lippard, S. J., Eds.; American Chemical Society: Washington, DC, 2005; Vol. ACS Symposium Series 903, p 400-413.

(95) Filomeni, G.; Cerchiaro, G.; Da Costa Ferreira, A. M.; De Martino, A.; Pedersen, J. Z.; Rotilio, G.; Ciriolo, M. R. *J. Biol. Chem.* **2007**, *282*, 12010-12021.

(96) Wang, T.; Guo, Z. J. *Current Medicinal Chemistry* **2006**, *13*, 525-537.

(97) Sun, L.; Wu, C. H.; Faust, B. C. *J. Phys. Chem. A* **1998**, *102*, 8664-8672.

(98) Halliwell, B.; Gutteridge, J. M. C.; Aruoma, O. I. *Analytical Biochemistry* **1987**, *165*, 215-219.

(99) Ellis-Davies, G. C. R.; Kaplan, J. H. *Proc. Natl. Acad. Sci. U.S.A.* **1994**, *91*, 187-191.

(100) Martell, A. E.; M., S. R. In *NIST Standard Reference Database 46*; 6.0 ed.; Motekaitis, R. J., Ed.; NIST: Gaithersburg, MD, 2001.

(101) Milburn, T.; Matsubara, N.; Billington, A. P.; Udgaonkar, J. B.; Walker, J. W.; Carpenter, B. K.; Webb, W. W.; Marque, J.; Denk, W.; Mccray, J. A.; Hess, G. P. *Biochemistry* **1989**, *28*, 49-55.

(102) Wieboldt, R.; Ramesh, D.; Jabri, E.; Karplus, P. A.; Carpenter, B. K.; Hess, G. P. *J. Org. Chem.* **2002**, *67*, 8827-8831.

(103) Kelland, L. *Nature Reviews Cancer* **2007**, *7*, 573-584.

(104) Jung, Y.; Lippard, S. J. *Chemical Reviews* **2007**, *107*, 1387-1407.

(105) Klein, A. V.; Hambley, T. W. *Chemical Reviews* **2009**, *109*, 4911-4920.

(106) Reedijk, J. *European Journal of Inorganic Chemistry* **2009**, 1303-1312.

(107) Bruijnincx, P. C. A.; Sadler, P. J. *Current Opinion in Chemical Biology* **2008**, *12*, 197-206.

(108) Mackay, F. S.; Farrer, N. J.; Salassa, L.; Tai, H.-C.; Deeth, R. J.; Moggach, S. A.; Wood, P. A.; Parsons, S.; Sadler, P. J. *Dalton Transactions* **2009**, 2315-2325.

(109) Bednarski, P. J.; Grünert, R.; Zielzki, M.; Wellner, A.; Mackay, F. S.; Sadler, P. J. *Chemistry & Biology* **2006**, *13*, 61-67.

(110) Ito, T.; Tanabe, K.; Yamada, H.; Hatta, H.; Nishimoto, S. *Molecules* **2008**, *13*, 2370-2384.

(111) Deiters, A. *ChemBioChem* **2009**, *11*, 47-53.

(112) Lee, H.-M.; Larson, D. R.; Lawrence, D. S. *ACS Chemical Biology* **2009**, *4*, 409-427.

(113) Agasti, S. S.; Chompoosor, A.; You, C.-C.; Ghosh, P.; Kim, C. K.; Rotello, V. M. *Journal of the American Chemical Society* **2009**, *131*, 5728-5729.

(114) Vivero-Escoto, J. L.; Slowing, I. I.; Wu, C.-W.; Lin, V. S. Y. *Journal of the American Chemical Society* **2009**, *131*, 3462-3463.

(115) Lin, W.; Peng, D.; Wang, B.; Long, L.; Guo, C.; Yuan, J. *European Journal of Organic Chemistry* **2008**, *2008*, 793-796.

(116) Noguchi, M.; Skwarczynski, M.; Prakash, H.; Hirota, S.; Kimura, T.; Hayashi, Y.; Kiso, Y. *Bioorganic & Medicinal Chemistry* **2008**, *16*, 5389-5397.

(117) Ciesienski, K. L.; Haas, K. L.; Dickens, M. G.; Tesema, Y. T.; Franz, K. J. *J. Am. Chem. Soc.* **2008**, *130*, 12246-12247.

(118) Salierno, M.; Fameli, C.; Etchenique, R. *European Journal of Inorganic Chemistry* **2008**, *7*, 1125-1128.

(119) Crider, S. E.; Holbrook, R. J.; Franz, K. J. *Metallomics* **2010**, *2*, 74-83.

(120) Hatchard, C. G.; Parker, C. A. *Proceedings of the Royal Society of London Series A* **1956**, *235*, 518-536.

(121) Webster, L. K.; Deacon, G. B.; Buxton, D. P.; Hillcoat, B. L.; James, A.

M.; Roos, I. A. G.; Thomson, R. J.; Wakelin, L. P. G.; Williams, T. L. *Journal of Medicinal Chemistry* **2002**, *35*, 3349-3353.

(122) Hall, M. D.; Okabe, M.; Shen, D.-W.; Liang, X.-J.; Gottesman, M. M. *Annual Review of Pharmacology and Toxicology* **2008**, *48*, 495-535.

(123) Wu, Z.; Liu, Q.; Liang, X.; Yang, X.; Wang, N.; Wang, X.; Sun, H.; Lu, Y.; Guo, Z. *Journal of Biological Inorganic Chemistry* **2009**, *14*, 1313-1323.

(124) Arnesano, F.; Scintilla, S.; Natile, G. *Angewandte Chemie International Edition* **2007**, *46*, 9062-9064.

(125) Balamurugan, K.; Schaffner, W. *Biochimica Et Biophysica Acta-Molecular Cell Research* **2006**, *1763*, 737-746.

(126) Kim, B.-E.; Nevitt, T.; Thiele, D. J. *Nat Chem Biol* **2008**, *4*, 176-185.

(127) Barnham, K. J.; Masters, C. L.; Bush, A. I. *Nat. Rev. Drug Disc.* **2004**, *3*, 205-214.

(128) Que, E. L.; Domaille, D. W.; Chang, C. J. *Chem. Rev.* **2008**, *108*, 1517-1549.

(129) Priya, C.; Sivaramapanicker, S.; Ayyappanpillai, A. *Chem. Asian J.* **2007**, *2*, 338-348.

(130) Domaille, D. W.; Zeng, L.; Chang, C. J. *J. Am. Chem. Soc.* **2010**, *132*, 1194-1195.

(131) Fabbrizzi, L.; Licchelli, M.; Pallavicini, P.; Perotti, A.; Taglietti, A.; Sacchi, D. *Chemistry-a European Journal* **1996**, *2*, 75-82.

(132) Jung, H. S.; Kwon, P. S.; Lee, J. W.; Kim, J. I.; Hong, C. S.; Kim, J. W.; Yan, S. H.; Lee, J. Y.; Lee, J. H.; Joo, T.; Kim, J. S. *Journal of the American Chemical Society* **2009**, *131*, 2008-2012.

(133) Khatua, S.; Choi, S. H.; Lee, J.; Huh, J. O.; Do, Y.; Churchill, D. G. *Inorganic Chemistry* **2009**, *48*, 1799-1801.

(134) Torrado, A.; Walkup, G. K.; Imperiali, B. *Journal of the American Chemical Society* **1998**, *120*, 609-610.

(135) Xie, J.; Menand, M.; Maisonneuve, P.; Metivier, R. *Journal of Organic Chemistry* **2007**, *72*, 5980-5985.

(136) Kim, M. H.; Jang, H. H.; Yi, S.; Chang, S.-K.; Han, M. S. *Chemical Communications* **2009**, 4838-4840.

(137) Li, G.-K.; Xu, Z.-X.; Chen, C.-F.; Huang, Z.-T. *Chemical*

Communications **2008**, 1774-1776.

(138) Lin, W.; Long, L.; Yuan, L.; Cao, Z.; Feng, J. *Analytica Chimica Acta* **2009**, *634*, 262-266.

(139) Swamy, K. M. K., Ko, S., Kwon, S. K., Lee, H. N., Mao, C., Kim, J., Lee, K., Kim, J., Shin, I., and Yoon, J. *Chem. Commun.* **2008**, *45*, 5915-5917.

(140) Wang, M. X.; Huang, S. H.; Meng, X. M.; Zhu, M. Z.; Guo, Q. X. *Chemistry Letters* **2008**, *37*, 462-463.

(141) Yu, M., Shi, M., Chen, Z., Li, F., Li, X., Gao, Y., Xu, J., Yang, H., Zhou, Z., Yi, T., and Huang, C. *Chem. Eur. J.* **2008**, *14*, 6892-6900.

(142) Shao, N.; Jin, J. Y.; Wang, H.; Zhang, Y.; Yang, R. H.; Chan, W. H. *Analytical Chemistry* **2008**, *80*, 3466-3475.

(143) Hyman, L. M.; Stephenson, C. J.; Dickens, M. G.; Shimizu, K. D.; Franz, K. J. *Dalton Transactions*, *39*, 568-576.

(144) Zhao, Y.; Zhang, X. B.; Han, Z. X.; Qiao, L.; Li, C. Y.; Jian, L. X.; Shen, G. L.; Yu, R. Q. *Analytical Chemistry* **2009**, *81*, 7022-7030.

(145) Liu, J.; Lu, Y. *Journal of the American Chemical Society* **2007**, *129*, 9838-9839.

(146) Yu, F.; Zhang, W.; Li, P.; Xing, Y.; Tong, L.; Ma, J.; Tang, B. *The Analyst* **2009**, *134*, 1826-1833.

(147) Zhou, H.; Ma, X.; Wang, J.; Zhang, L. *Organic & Biomolecular Chemistry* **2009**, *7*, 2297-2302.

(148) Berthelot, T.; Talbot, J. C.; Lain, G.; Deleris, G.; Latxague, L. *Journal of Peptide Science* **2005**, *11*, 153-160.

(149) Brown, D. R.; Kozlowski, H. *Dalton Transactions* **2004**, 1907-1917.

(150) Arnesano, F.; Banci, L.; Bertini, I.; Ciofi-Baffoni, S. *European Journal of Inorganic Chemistry* **2004**, 1583-1593.

(151) Huffman, D. L.; O'Halloran, T. V. *Annual Review of Biochemistry* **2001**, *70*, 677-701.

(152) O'Halloran, T. V.; Culotta, V. C. *Journal of Biological Chemistry* **2000**, *275*, 25057-25060.

(153) Puig, S.; Thiele, D. J. *Current Opinion in Chemical Biology* **2002**, *6*, 171-180.

(154) Rosenzweig, A. C.; O'Halloran, T. V. *Current Opinion in Chemical*

Biology **2000**, *4*, 140-147.

(155) Gupte, A.; Mumper, R. J. *Cancer Treatment Reviews* **2009**, *35*, 32-46.

(156) Devi, G. S.; Prasad, M. H.; Saraswathi, I.; Raghu, D.; Rao, D. N.; Reddy, P. P. *Clinica Chimica Acta* **2000**, *293*, 53-62.

(157) Pelicano, H.; Carney, D.; Huang, P. *Drug Resistance Updates* **2004**, *7*, 97-110.

(158) Pervaiz, S. *Current Pharmaceutical Design* **2006**, *12*, 4469-4477.

(159) Rozga, M.; Sokolowska, M.; Protas, A. M.; Bal, W. *Journal of Biological Inorganic Chemistry* **2007**, *12*, 913-918.

(160) Chang, C. Y.; Niblack, B.; Walker, B.; Bayley, H. *Chem. & Biol.* **1995**, *2*, 391-400.

(161) Martell, A. E.; Hancock, R. D.; Motekaitis, R. J. *Coordination Chemistry Reviews* **1994**, *133*, 39-65.

(162) Martell, A. E.; Hancock, R. D. *Metal Complexes in Aqueous Solution*; Plenum Press: New York, 1996.

(163) Rybka, J. S.; Margerum, D. W. *Inorganic Chemistry* **1980**, *19*, 2784-2790.

(164) Lacoste, R. G.; Martell, A. E. *Inorganic Chemistry* **1964**, *3*, 881-884.

(165) Cox, E. H.; McLendon, G. L. *Current Opinion in Chemical Biology* **2000**, *4*, 162-165.

Biography

The author was born on July 4, 1982 in Reading, Pennsylvania. She attended the Reading Public Schools in Reading, PA during her elementary years. In 2000, she graduated from Muhlenberg High School located in Reading, PA. She attended Millersville University, a public university located in Lancaster, PA. In 2004, Kate graduated magna cum laude from Millersville University with a B.S. in Chemistry, honors in Chemistry and Mathematics, and a varsity letter in softball.

In the fall of 2004, Kate began her graduate work in the Chemistry Department at Duke University under the direction of Dr. Katherine Franz. During her tenure at Duke University, Kate received the Burroughs Welcome Award, the Kathleen Zielek Fellowship, and Chemistry Departmental Recognition Awards. Her work has resulted in publications in journals such as *The Journal of the American Chemical Society*, *The European Journal of Inorganic Chemistry* and papers submitted to *The Journal of Inorganic Chemistry* and *Angewandte Chemie International Edition*. Following her graduate work in Dr. Franz's laboratory, Kate will pursue postdoctoral research at Harvard University in the laboratory of Dr. Peter Caravan.